4
Results

This chapter presents the outcomes of binary Al-Si alloy selection and their process variables on the evolution in microstructure and mechanical properties by varying the test methods and conditions. The processing encompasses both as-cast and mechanically processed states, with the latter consisting of hot extrusion, friction stir processing, and high pressure torsion. The room temperature tests for mechanical properties involved measurement of hardness, tensile, and compressive properties. Only tensile tests were done at elevated temperatures, but the same were extended to investigating the effects of test temperature and strain rate towards examining the variations in the parameters of the constitutive relationship and nature of stress-strain curves, as affected by concurrent microstructure evolution. Microstructures were examined by using optical and scanning electron microscopes. The quantitative aspects of microstructural study considered measurements of grain size, particle size, and phase proportion across the various alloy compositions, mechanical processing, and test conditions, which highlights the impact noted on the changes occurred with respect to the initial as-cast microstructure. This chapter gives a detailed analysis of the deformation behaviour of Al-Si alloys at both ambient and elevated temperatures, which was aimed to elucidate the parameters governing the constitutive relationship and the underlying deformation mechanisms. The interrelationships among the mechanical properties, as well as structure-property correlation, were explored in an attempt to unify the findings, irrespective of apparent variations with respect to each other.

4.1 MICROSTRUCTURE EVOLUTION

4.1.1 As-cast Microstructure of Al-Si Alloys

The microstructures of different compositions of as-cast Al-Si alloys were examined using an optical microscope, as shown in Figure 4.1. It is noted that the microstructures consist of the α-Al phase, the eutectic phase, and the primary silicon phase. In the hypoeutectic Al-Si alloys (2wt.% Si, 4wt.% Si, 7wt.% Si, 8wt.% Si) depicted in Fig. 4.1 (a-d), the dendritic α-Al serves as the major phase and acts as a matrix, while the fine eutectic phase is present in lesser proportions along the grain boundaries of the aluminium matrix. Based on the Al-Si binary phase diagram (Murray and McAlister, 1984), the solubility of silicon in aluminium is only 1.65wt.% at eutectic temperature, which decreases to 0.05wt.% at room temperature. Consequently, adding more silicon leads to the precipitation of pure silicon (primary Si), which becomes the dominant phase in hypereutectic Al-Si alloys (20wt.% Si and 30wt.% Si). Also, the silicon morphology changes with an increase in wt.% Si in the alloy. It can be seen that the fibrous type shape of primary silicon appears in eutectic Al-Si alloy, Figure 4.1(e), but it changed to polyhedral type in hypereutectic Al-20Si, Figure 4.1(f). Further, the coarse primary silicon particles are present in plate-type shape in the hypereutectic Al-30Si and Al-50Si alloys, Figure 4.1(g,h). Silicon growth takes place through the twin plane re-entrant edge (TPRE) mechanism, and it is based on the formation of twin planes through the silicon lamella. It was reported by Wagner (R.S. Wagner, 1960; Wagner *et al.*, 1964) and Hamilton and Siedensticker in 1960 on the faceted growth mechanism of germanium crystals (Hamilton and Seidensticker,

1960). The chemical compositions of as-cast alloys, as analysed by optical emission spectroscopy (OES) and x-ray fluorescence (XRF), are reported in Table 3.1.

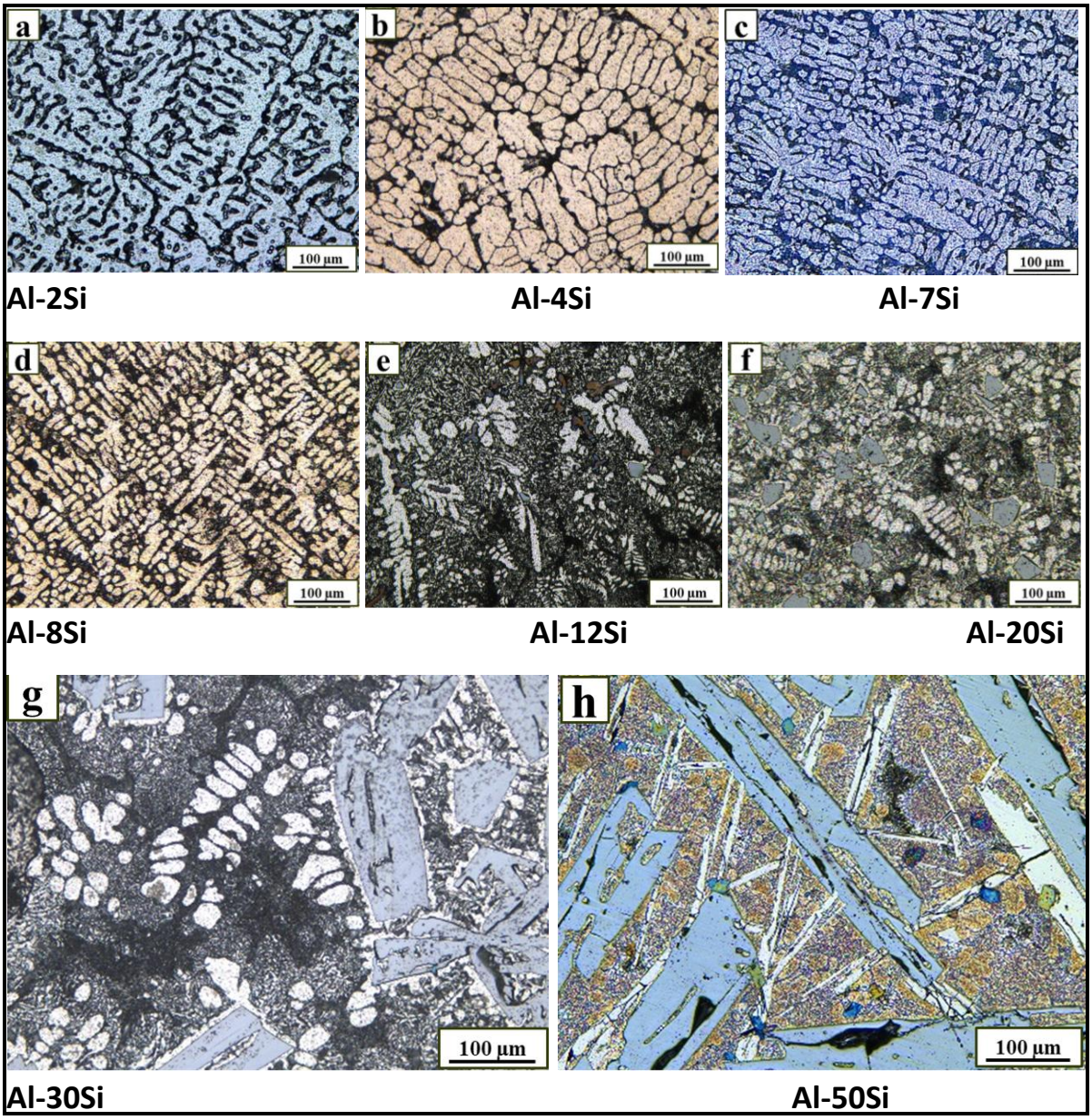


Figure 4.1 : Optical micrographs of as-cast Al-Si alloys: (a-d) hypoeutectic (Al-2Si, Al-4Si, Al-7Si, and Al-8Si) Al-Si alloys, (e) eutectic (Al-12Si) alloy, and (f-h) hypereutectic (Al-20Si, Al-30Si, and Al-50Si) alloys

The microstructural parameters, including grain size (d_α), secondary dendrite arm spacing (SDAS), primary silicon size (d_p), and volume fraction (f) of phases, were measured for as-cast Al-Si alloys. These parameters were plotted as a function of wt.% Si (C_{Si}), as shown in Figure 4.2(a, b), and their values are listed in Table 4.1. Figure 4.2(a) shows the variation in both the α-Al grain size (d_α) and silicon particle size (d_p) as a function of silicon content (C_{Si}). d_α decreases with an increase in C_{Si}, whereas, in contrast, d_p increases with increasing silicon content. They follow the trend as expressed

$$d_\alpha = 130.5(C_{Si})^{-0.7}, \qquad R^2 = 0.9 \qquad (4.1)$$

$$d_p = 0.004(C_{Si})^3, \qquad R^2 = 1 \qquad (4.2)$$

The fractions of different phases are also found to vary as a function of silicon content in the alloys, Figure 4.2(b). As shown in Figure 4.1, it can be observed from the optical microstructures that the α-Al phase fraction (f_α) decreases with increasing silicon content. In contrast, the eutectic phase fraction (f_{eu}) increases with increasing silicon content up to the eutectic Al-Si alloy composition. In hypereutectic Al-Si alloys, the primary silicon phase fraction (f_p) is increased much more than in the other two compositions of hypoeutectic and eutectic ones.

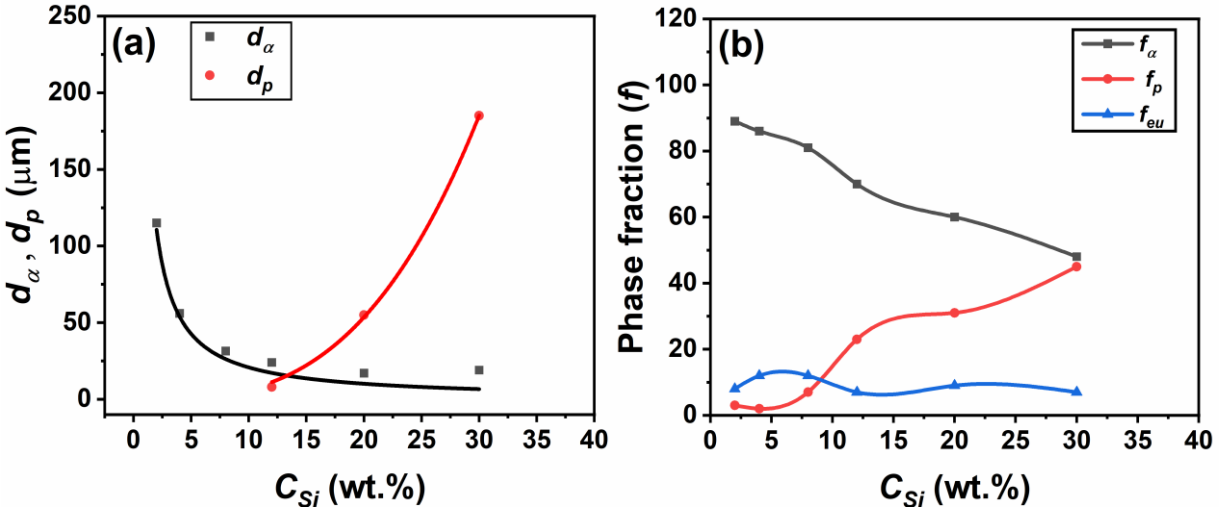


Figure 4.2 : (a) Variation in grain size (d_α) and primary silicon particle size (d_p), (b) variation in phase proportions (f) as a function of silicon content

Table 4.1 : Microstructural parameters (grain size, primary Si size, and phase fractions) in Al-Si alloys of different compositions (wt.%) in the as-cast state

Alloy	*As-Cast*				
	Size (µm)		*Phase fraction (%)*		
	d_α	d_p	f_α	f_{eu}	f_p
Al2Si	115±3	-	89	8	3
Al4Si	56±1	-	86	12	2
Al8Si	31.4±1	-	81	12	7
Al12Si	24±1	8±0.6	70	7	23
Al20SI	17±1	55±3	60	9	31
Al30Si	19±1	185±5			

4.1.2 Microstructure of Mechanically Processed Al-Si Alloys

In the current study, mechanical processing techniques, including hot extrusion, friction stir processing (FSP), and high-pressure torsion (HPT), were employed to refine the matrix grain size and primary silicon size, as well as to achieve a uniform distribution of second-phase (Si) particles in the cast Al-Si alloys of various compositions. These mechanical processing methods were aimed at enhancing the overall mechanical properties.

(a) Microstructures Evolved by Hot Extrusion

Hot extrusion is a widely utilized process for its ability to refine grain structure and reduce casting defects/porosity in metals by a large deformation in a single pass. Presented in Figures 4.3 and 4.4 are the optical microstructures of the longitudinal section and transverse section of Al-Si alloys of different compositions after being extruded at various temperatures ranging from 510K to 810K.

Following hot extrusion, the dendritic matrix grain structure presented in Figure 4.1 transforms into equiaxed grains, accompanied by variations in primary silicon (P-Si) size and morphology, based on the extrusion temperature and wt.% Si. This process of extrusion led to a well-modified microstructure. Regarding the effect of extrusion temperature, the microstructural features (grain size and particle size) demonstrate refinement at lower extrusion temperatures across all alloy compositions. However, the silicon particles assume a globular shape and exhibit uniform distribution at higher extrusion temperatures (710K and 810K). The matrix grain size becomes more equiaxed at higher extrusion temperatures, but this leads to coarser matrix grains in all the Al-Si alloys.

At lower extrusion temperatures (510K and 610K), the longitudinal section of the hypoeutectic and eutectic Al-Si samples displays a banded structure (Figures 4.3(a_2) and 4.3(b_1), along with elongated α-Al grains and short rod-like silicon particles in the direction of extrusion. In contrast, the transverse section reveals an equiaxed microstructure, Figure 4.4. Above the extrusion temperature of 610K, both longitudinal and transverse sections of all the Al-Si alloys exhibit equiaxed grains and a globular silicon morphology.

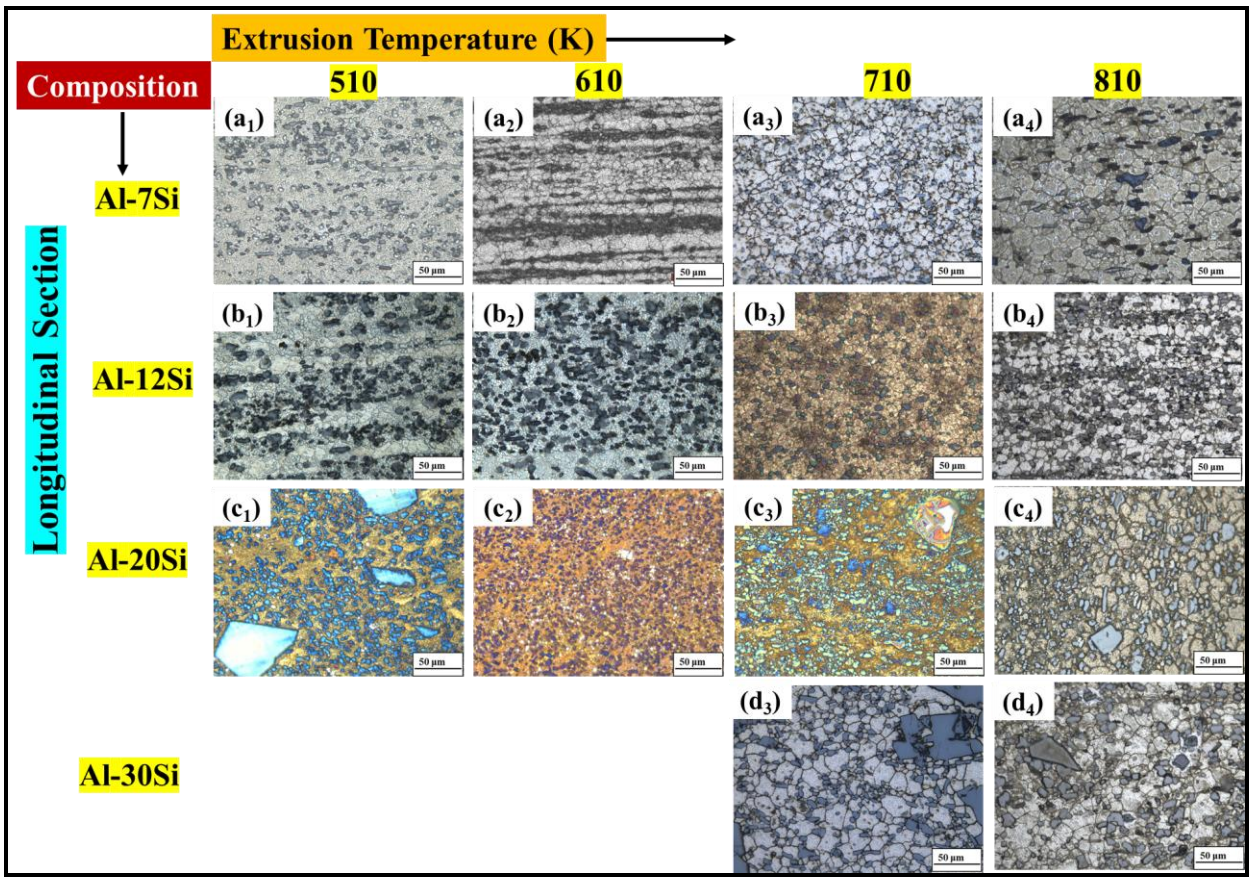


Figure 4.3 : Optical micrographs of the longitudinal section of Al-Si alloys of different compositions upon extrusion at different temperatures: (a_1-a_4) Al-7Si alloy, (b_1-b_4) Al-12Si alloy, (c_1-c_4) Al-20Si alloy, and (d_3-d_4) Al-30Si alloy (a_1-a_4, b_1-b_4, c_1-c_4, and d_3-d_4, where, 'a', 'b', 'c', and 'd' are used for Al-7Si, Al-12Si, Al-20Si, and Al-30Si, and the subscripts 1, 2, 3, 4 are used to represent the four extrusion temperatures, 510, 610, 710, 810K, respectively)

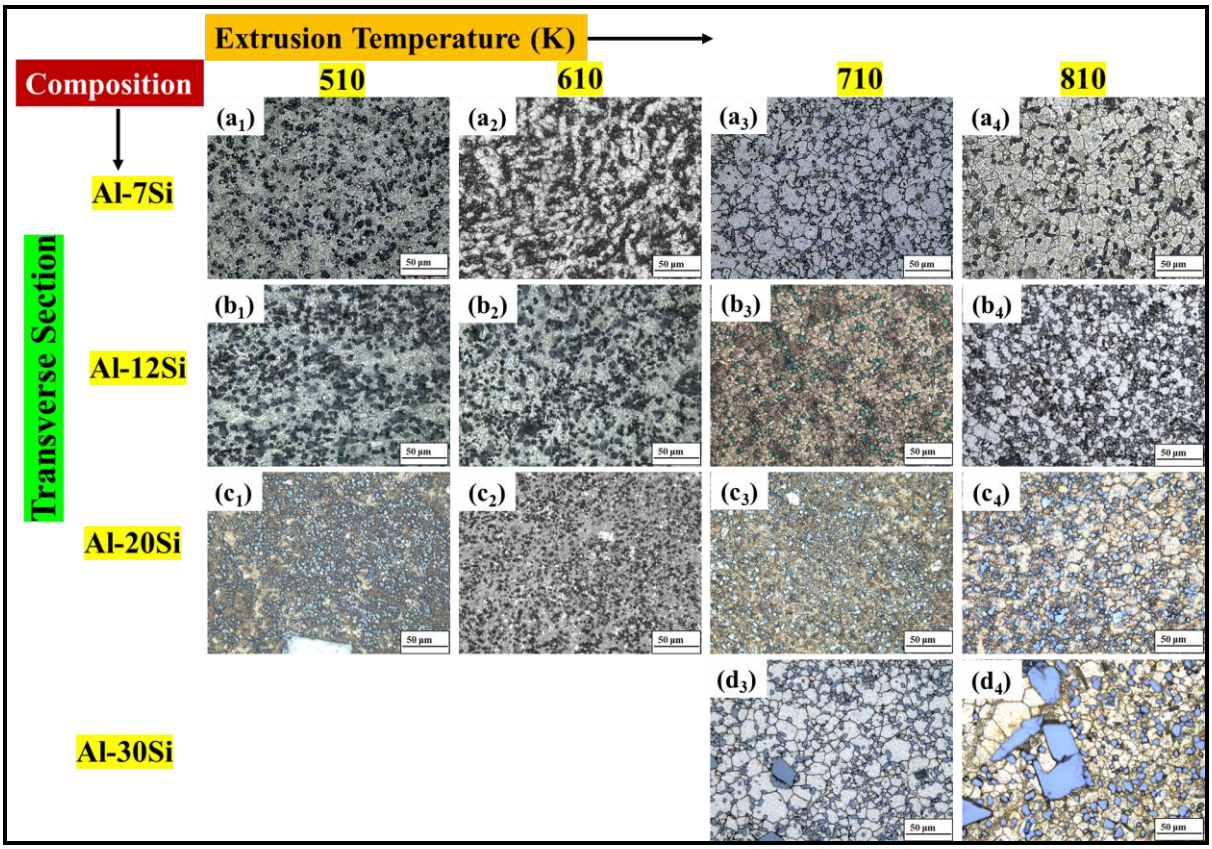


Figure 4.4 : Optical micrographs of the transverse section of Al-Si alloys of different compositions upon extrusion at different temperatures: (a_1-a_4) Al-7Si alloy, (b_1-b_4) Al-12Si alloy, (c_1-c_4) Al-20Si alloy, and (d_3-d_4) Al-30Si alloy (a_1-a_4, b_1-b_4, c_1-c_4, and d_3-d_4, where, 'a', 'b', 'c', and 'd' are used for Al-7Si, Al-12Si, Al-20Si, and Al-30Si, and the subscripts 1, 2, 3, 4 are used to represent the four extrusion temperatures, 510, 610, 710, 810K, respectively)

Figure 4.5(a) reveals that the grain size initially decreases with an increase in silicon content, reaching a minimum value, but then it subsequently increases with further increases in silicon content. Additionally, the grain size increases with higher extrusion temperatures for high silicon alloys. The primary silicon size increases with increasing Si in the higher extrusion temperature regime. The morphology of primary silicon varies depending on the silicon content, exhibiting a globular shape in hypoeutectic Al-Si alloys and a plate-like shape in hypereutectic Al-Si alloys. In hypereutectic Al-Si alloys, the initially large primary silicon particles in the as-cast state undergo refinement, ranging from ~4µm to 5.2µm under all extrusion conditions. The α-Al grain size ranges from 3.8µm to 8.3µm, depending on the extrusion temperature, with the smallest value of 3.8µm observed at lower extrusion temperature. In hypoeutectic and eutectic Al-Si alloys, the primary silicon size falls within the range of 2µm to 3.4µm.

The phase fractions were calculated for all the conditions and analysed as a function of extrusion temperature and alloy composition, Figure 4.5(b). The phase fraction demonstrates its variation with wt.% Si (C_{Si}) in the Al-Si alloys while remaining relatively constant with respect to extrusion temperature. The matrix phase proportion (f_α) decreases with increasing Si content, while the primary silicon phase (f_p) increases with increasing Si content. The eutectic phase fraction (f_{eu}) was found to remain low and nearly constant as a function of wt.% Si.

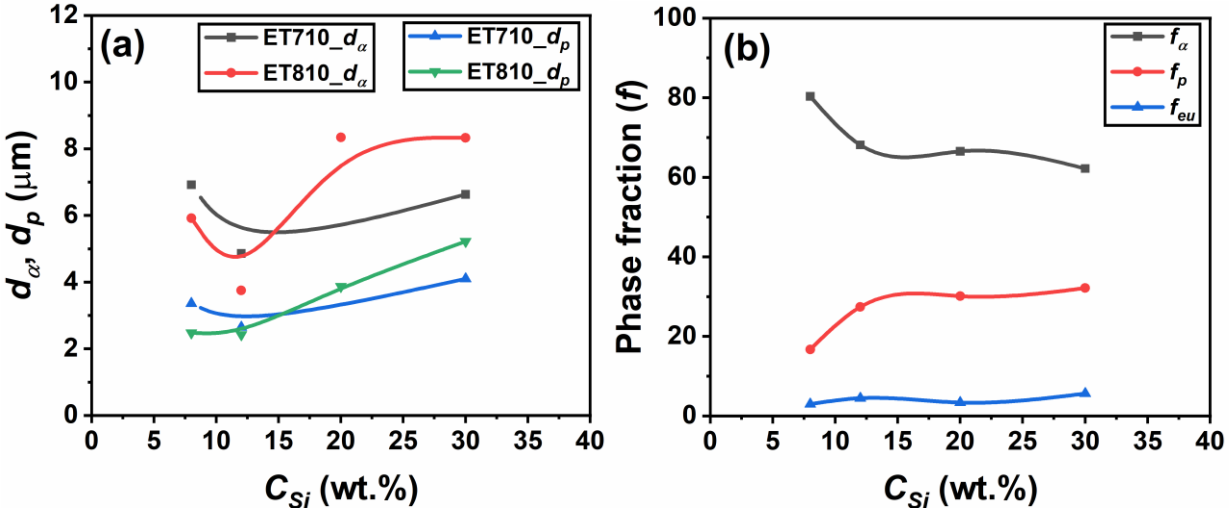


Figure 4.5 : Variation in grain size (d_α) and primary silicon particle size (d_p) as a function of silicon content (a); and (b) change in the α-Al matrix, primary silicon, and eutectic phase fractions as a function of C_{Si} in the extruded Al-Si alloys (Legends in (a) have the meanings as exemplified for ET710- '*ET*' represents the extrusion temperature and the '710' is the temperature in kelvin)

Table 4.2 : Microstructural parameters (grain size, primary Si size, and phase fractions) for Al-Si alloys of different compositions (wt.%) after hot extrusion at different temperatures (Note: no measurements could be made at lower temperatures owing to the banded microstructures and lack of clarity in revealing the grain boundaries)

Alloy	*Extrusion conditions*											
	510 K			*610 K*			*710 K*			*810 K*		
	d_α	d_p	f_α	d_α	d_p	f_α	d_α	d_p	f_α	d_α	d_p	f_α
Al8Si	No measurements could be done.						6.9	3.4	80.3	5.9	2.5	80.3
Al12Si							4.9	2.7	-	3.8	2.4	68.1
Al20Si							-	-	71.5	8.3	3.9	66.5
Al30Si							6.6	4.1	60.9	8.3	5.2	62.2

(b) Microstructures Evolved Under Friction Stir Process (FSP)

Friction stir processing (FSP) was used as a severe plastic deformation technique to modify the as-cast microstructure of various Al-Si alloys. Many authors studied the effect of FSP on microstructural variations and reported that the microstructure of the as-cast alloy was generally highly refined. In the current work, the FSP was done at a rotational speed of 1400rpm and traverse speed of 40mm/min with one pass, two overlapped passes, and three overlapped FSP passes. The details of the FSP process with variations in parameters are elaborated in Chapter 3: Experimental Procedures.

Figures 4.6(a-l) display the optical micrographs of various Al-Si alloys processed under different FSP conditions. As shown in Figure 4.1(a-h), in the as-cast Al-Si alloys, a dendritic structure is observed in hypoeutectic (Al-2Si, Al-4Si, Al-8Si) and eutectic (Al-12Si) compositions, while the large primary silicon particles are evident in hypereutectic (Al-20Si, Al-30Si, Al-50Si) compositions. Following a single FSP pass, Figure 4.6(a-d), the dendritic structure in hypoeutectic Al-8Si and eutectic Al-12Si alloys is disrupted, resulting in equiaxed α-Al grains with some refinement. Additionally, the matrix grains are surrounded by randomly distributed

refined eutectic silicon. However, in hypereutectic Al-20Si and Al-30Si alloys, coarse/large primary silicon particles undergo some refinement and redistribution after a single FSP pass (Figures 4.6(c) and 4.6(d)). Although refined, some large silicon particles are still present after one FSP pass. Notable changes in the microstructure are not observed at this stage.

After two and three FSP passes, it becomes evident that the silicon particles are significantly refined, assuming a globular shape, and are uniformly distributed throughout the matrix in all Al-Si alloys. Additionally, it is noteworthy that the porosities present in the as-cast Al-Si alloy are completely eliminated after three FSP passes.

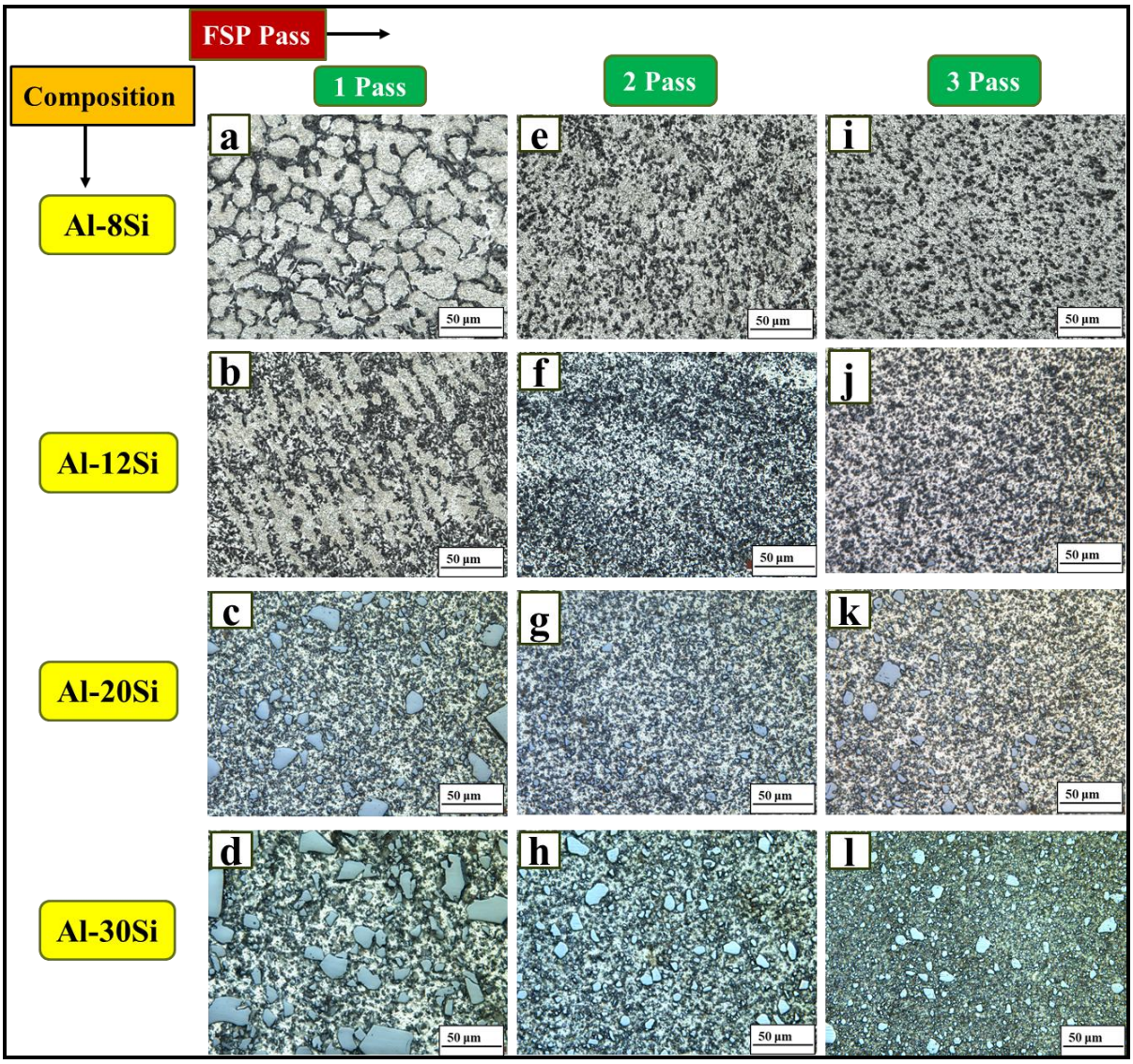


Figure 4.6 : Optical microstructures upon (a-d) one pass, (e-h) two overlapped passes, (i-l) three overlapped passes of FSP processed hypoeutectic Al-8Si (a,e,i), eutectic Al-12Si (b,f,j), and hypereutectic Al-20Si (c,g,k), Al-30Si (d,h,l) Al-Si alloys

Furthermore, Figure 4.7 shows the effect of rotational and traverse speeds of the FSP tool on the microstructures of hypoeutectic Al-2Si and Al-4Si alloys. In the first set, the rotational speed is fixed at 800rpm, and optical microstructures of Al-2Si after one pass FSP at a traverse speed of 100mm/min, 200mm/min, and 250mm/min were observed, Figure 4.7(a-c), microstructures of Al-2Si at a fixed traverse speed of 150mm/min and at a rotational speed of 800rpm, 1200rpm, and 1400rpm were depicted in Figure 4.7(d-f). Similarly, optical microstructures of Al-4Si upon single pass FSP at a fixed rotational speed of 800rpm and traverse speed of 200mm/min and 250mm/min were observed, shown in Figure 4.7(g,h). Also,

the microstructure of Al-4Si for a fixed traverse speed of 150mm/min and at the rotational speeds of 800rpm, 1200rpm, and 1400rpm are presented in Figure 4.7(i-k)

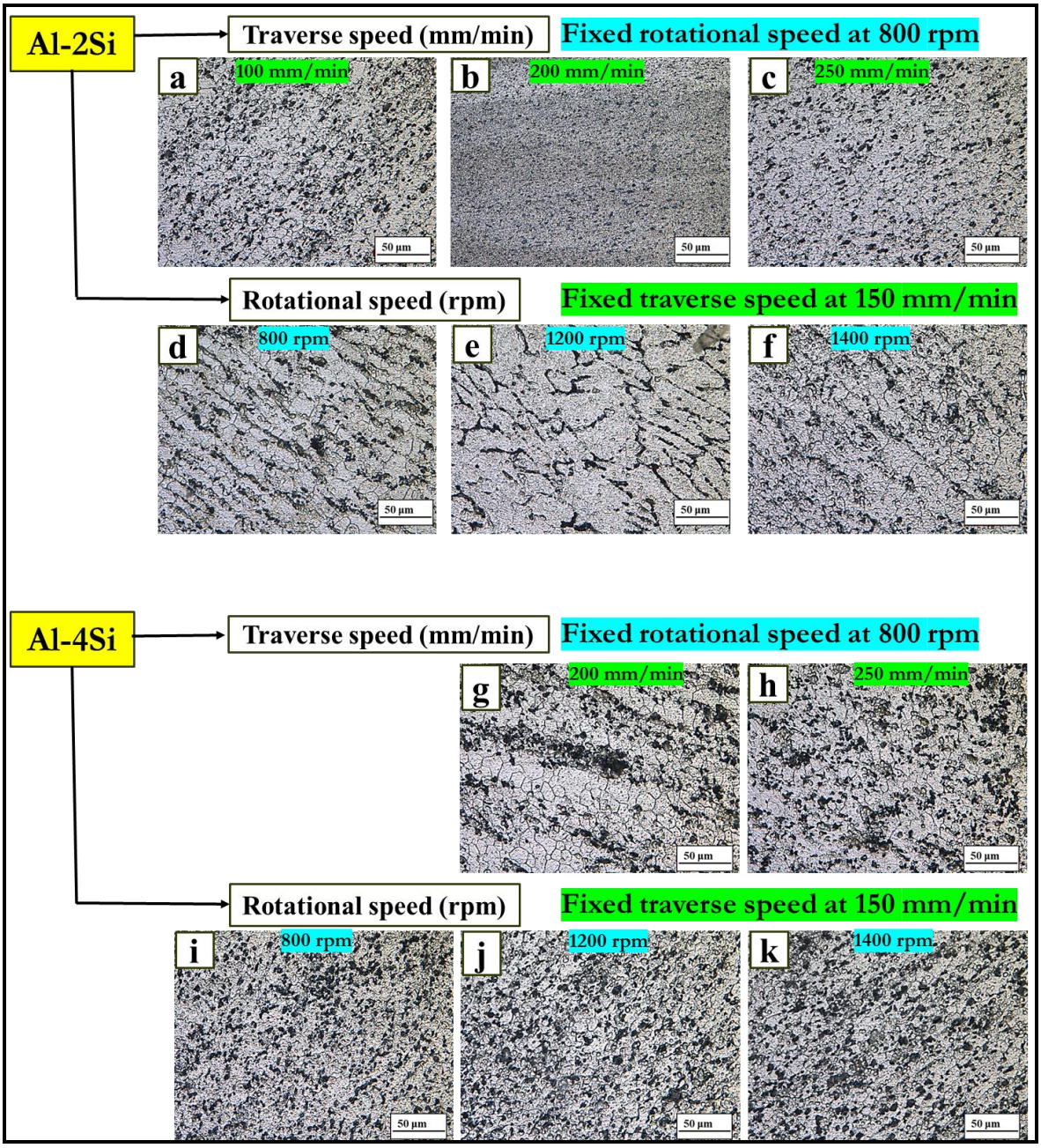


Figure 4.7 : Optical microstructures of Al-2Si single pass FSP at (a) traverse speed of 100mm/min, (b) traverse speed of 200mm/min, (c) at traverse speed of 250mm/min for fixed rotational speed of 800rpm of FSP processed; microstructures of Al-2Si at a fixed traverse speed of 150mm/min and at the (d) rotational speed of 800rpm, (e) rotational speed of 1200rpm, (f) rotational speed of 1400rpm. Optical microstructures of Al-4Si upon single pass FSP at (g) traverse speed of 200mm/min, (h) at traverse speed of 250mm/min for fixed rotational speed of 800rpm of FSP processed, and microstructure of Al-4Si for a fixed traverse speed of 150mm/min and at the (i) rotational speed of 800rpm, (j) rotational speed of 1200rpm, (k) rotational speed of 1400rpm

In Figure 4.8(a), it is evident that the average grain size of the Al-2Si alloy subjected to a single pass of FSP remains relatively stable, showing an approximate value of 6±0.5µm despite variations in traverse speed of 100-250mm/min (as shown in Figure 4.8(a)) at a fixed rotational speed of 800rpm. However, we observe that the grain size initially increases from 9.8µm to 16.4µm and then decreases to 9.7µm with an increase in rotation speed from 800 to 1400rpm (as shown in Figure 4.8(b)) at a fixed traverse speed of 150mm/min. For the Al-4Si alloy processed

with a single pass of FSP, we note a slight decrease in grain size from 7µm to 6.2µm as the traverse speed increases from 200 to 250mm/min (as shown in Figure 4.8(a)). In contrast, as depicted in Figure 4.8(b), the grain size continuously increases from 5.5µm to 7.5µm with an increasing rotational speed from 800 to 1400rpm.

In summary, it can be implied that grain size tends to increase with higher rotational speeds, whereas it decreases with higher traverse speeds. This behaviour can be attributed to the heat generated during FSP due to the frictional interaction between the tool and the workpiece, which depends on the FSP pass duration. Increasing traverse speed results in reduced local heat generation, favouring dynamic recrystallization over annealing effects. Conversely, higher rotation speeds generate more heat, promoting the growth kinetics of dynamic recrystallization through annealing effects.

Figure 4.8(c) shows the plot of variation in grain size as a function of Si content for three-pass FSP-processed Al-Si alloys. It can be seen that after three-pass FSP, the grain size first decreased from 2.7µm to 2.4µm as the silicon increased from 8wt.% Si to 12wt.% Si and then remained constant as a function of silicon content. The Si particle size was obtained in the range of 1.4-2.3µm after three passes of FSP.

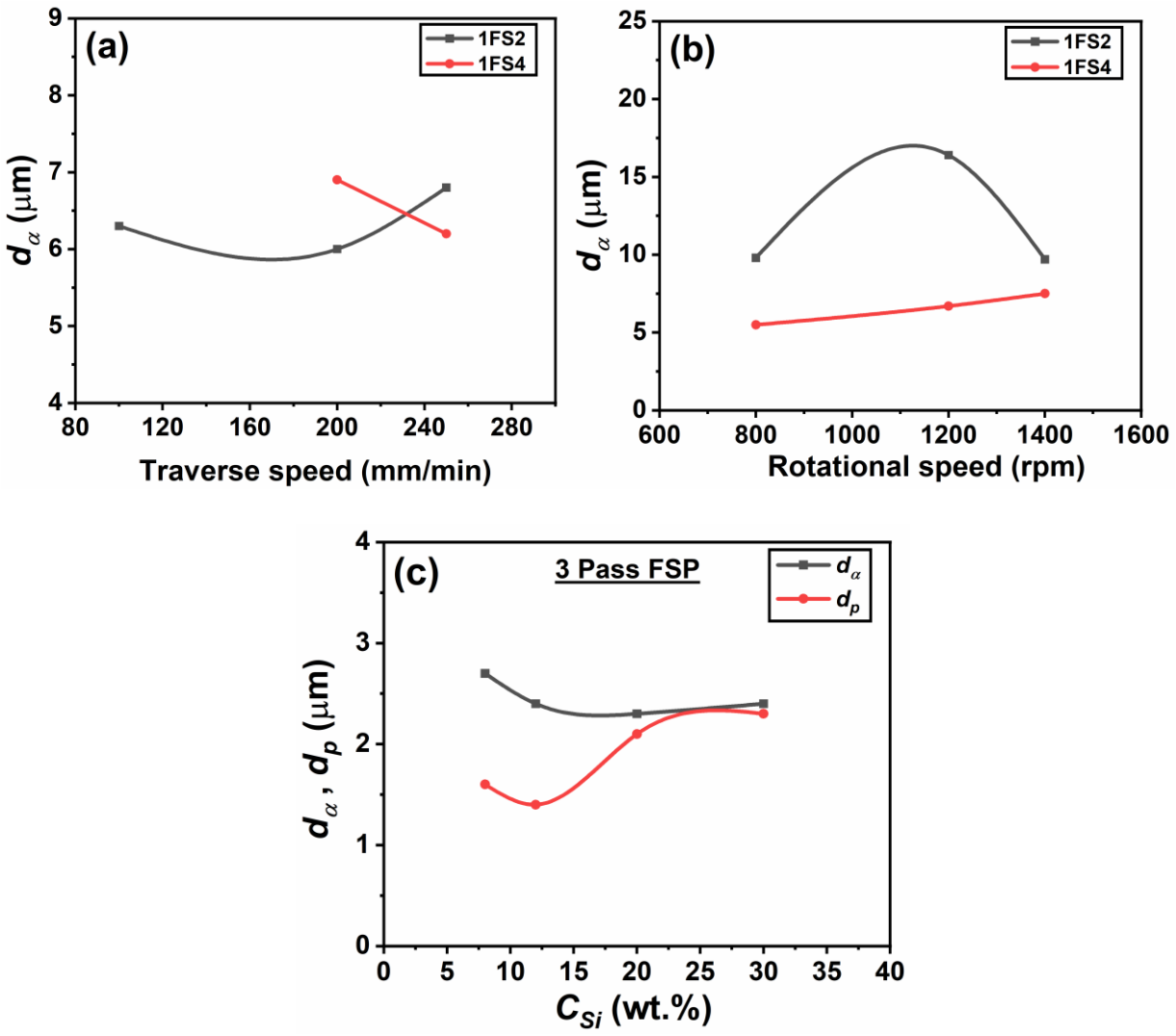


Figure 4.8 : Plot of grain size (d_α) as a function of (a) traverse speed, (b) rotational speed of the FSP tool for Al-2Si and Al-4Si alloys, and (c) change in d_α and d_p as a function of silicon content after three-pass FSP of the Al-8Si, Al-12Si, Al-20Si, and Al-30Si alloys

(c) Microstructures Evolved Under High Pressure Torsion (HPT) Process

The optical microstructures of Al-Si alloys processed with a varying number of turns in high pressure torsion (HPT) were examined. The microstructures upon HPT reveal a significant refinement and the emergence of alternating patterns of matrix and silicon phases. The central region of the microstructure appears similar to the as-cast state, while refinement is observed to extend away from the centre of the disc sample. Moreover, it is evident that both refinement and homogenization increase as the distance from the centre to the edge of the sample increases.

Typical optical micrographs of eutectic Al-12Si alloy taken in the centre, mid-radius, and the edge of the HPT processed samples for N=0 (6GPa compression), ½, 1, 2, 10, 20, 50, and 100 are presented in Figure 4.9. The micrographs in the first column are shown at low magnification, whereas the micrographs in the 2nd, 3rd, and 4th columns represent them ten times magnified in the centre, the mid-radius, and at the edge of the disc-shaped HPT samples, respectively. It is seen that the microstructures on compression alone retain the as-cast structure, except that the Si flakes are broken and dispersed within the matrix. For all HPT turns, it is noted that the microstructures become more homogeneous and refined while moving diametrically from the centre to the edge through the mid-radius locations. Similar effects of homogenization and refinement in the microstructure appear with the increasing number of HPT rotations for all the selected locations. A careful examination of the microstructures at low magnification (Column 1 of Figure 4.9) suggests that the microstructures tend to align along the rotational direction of the anvil on their way to refinement and homogenization. By the time it reaches N=10, the micrograph shows the formation of distinct concentrating circles of alternate bright and dark regions corresponding to the α-Al matrix and the Si particles. The higher magnified FESEM micrographs for 2 turns, 10 turns, and 50 turns of Al-12Si alloy at the centre, mid-radius, and edge illustrate the degree of microstructure refinement, as shown in Figure 4.10(a-g). It can be observed that both the particles and matrix become more refined with increasing radius from the centre to the edge and with an increasing number of HPT turns. At the edge of all the samples presented, the particles are at the nano-scale. The matrix and particle sizes are identical at the edge, reflecting a homogeneous distribution of the two phases. There develops a systematic gradient in microstructure (d_α) refined as a function of equivalent strain (ε_{eq}) following the exponential relation of type:

$$d_\alpha = C_{HS} exp(-D_{HS}\varepsilon_{eq}), \tag{4.3}$$

where the pre-exponential term C_{HS} and the exponential term D_{HS} are found to be sensitive to both the radius and number of turns of rotation.

Table 4.3 : Pre-exponential constants values for different HPT turns (N or ε_{eq}) for Al-12Si alloy

HPT Turns (N or ε_{eq})	C_{HS}	D_{HS}
0.5	7.5	0.1
1	6.5	0.05
10	2.6	0.001
50	2.4	0.0005

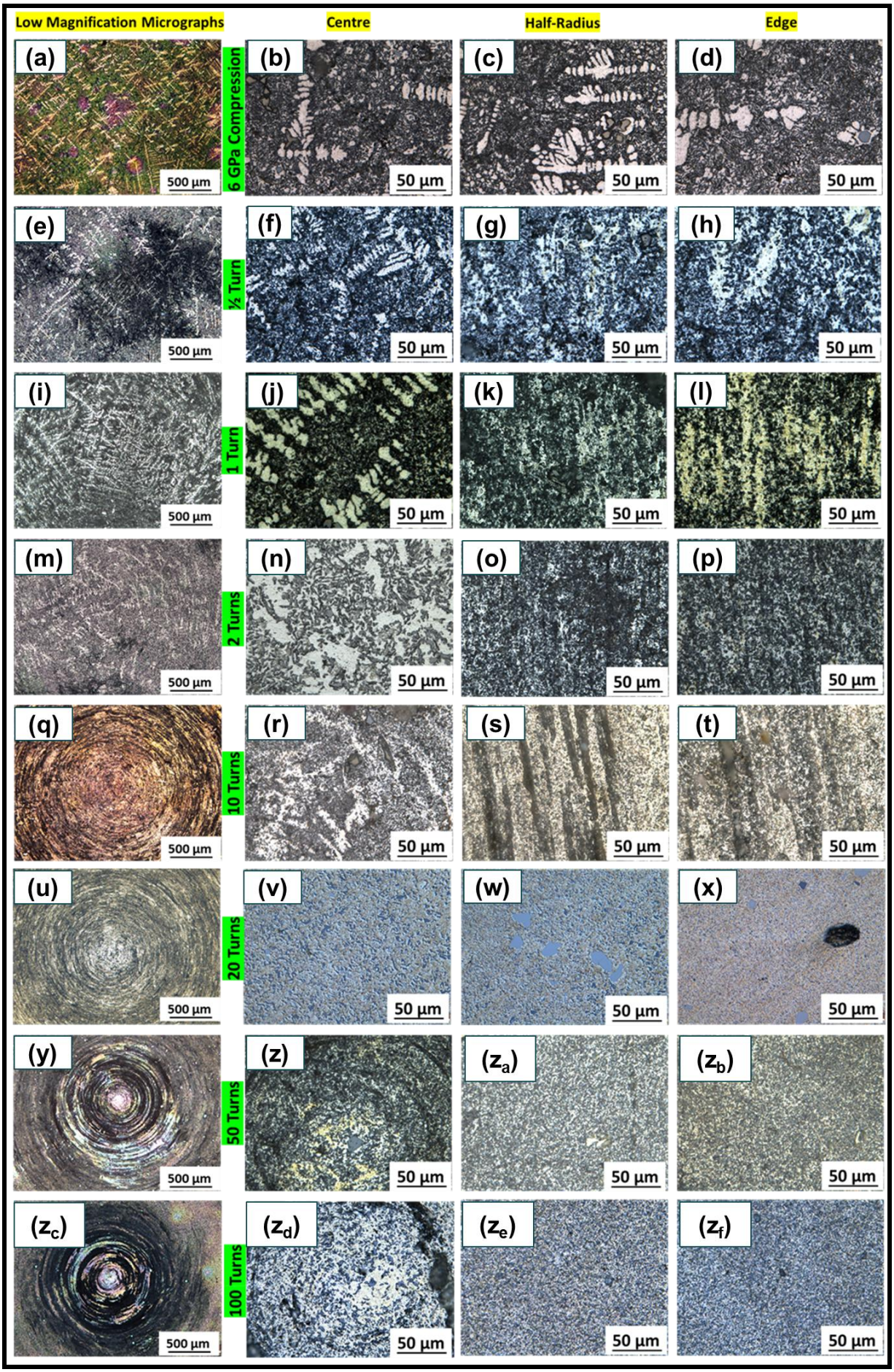


Figure 4.9 : (a-z_f) Diametrical variation in microstructures observed in the optical microscope as a function of the number of HPT turns (~equivalent strain) of eutectic Al-12Si alloy

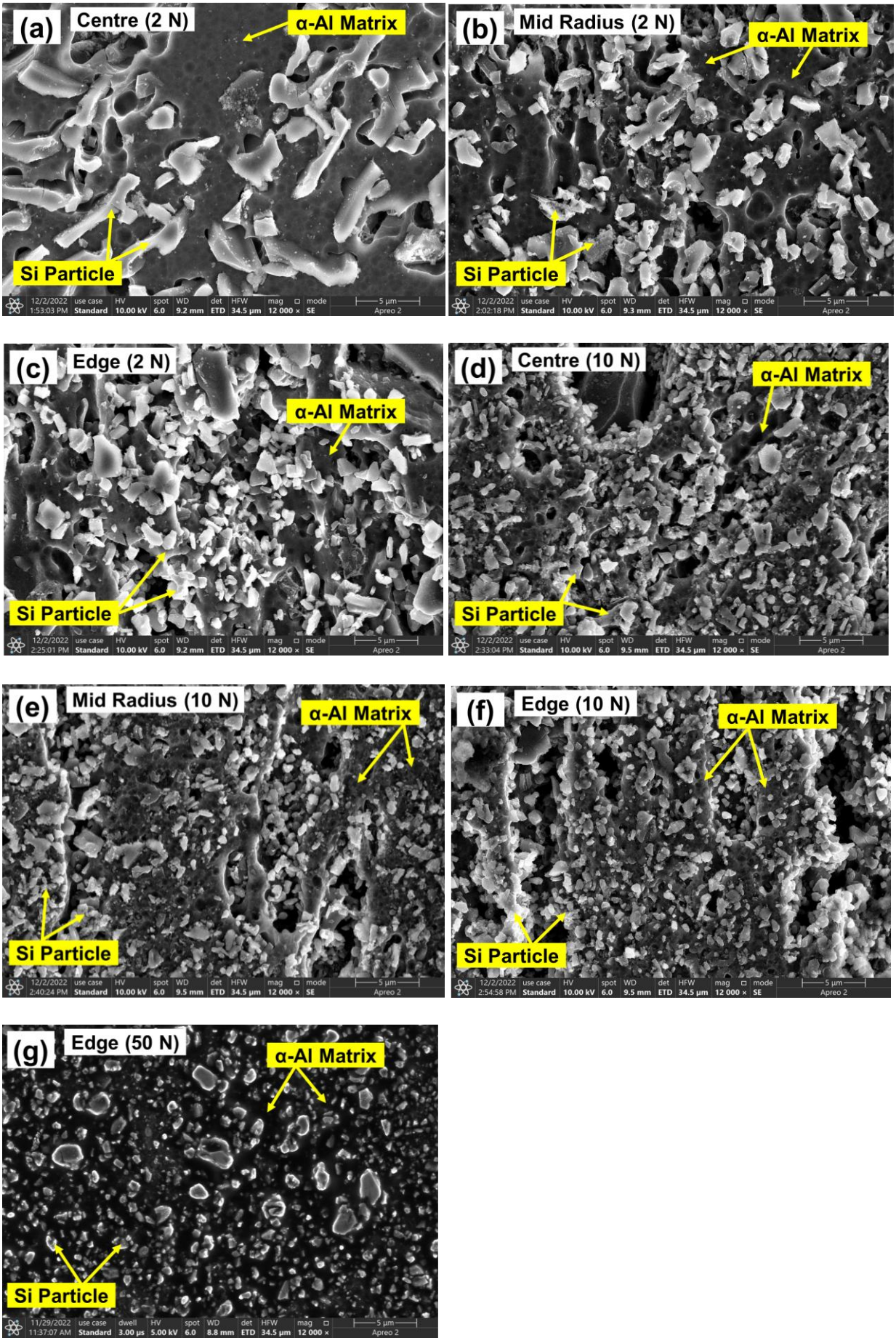


Figure 4.10 : (a-c) Typical magnified FESEM micrographs of 2 HPT turns, (d-f) 10 HPT turns at centre, mid-radius, edge, respectively, and (g) 50 HPT turns at the edge of Al-12Si alloy

The sizes of the α-Al matrix (d_α) and Si particles (d_p) measured are plotted in Figure 4.11(a) and Figure 4.11(b), respectively, as a function of N, which, along with the radius (r) of the sample, represents a measure of equivalent strain (Eq. 2.2). It is noticed that the refinement in both α-Al matrix and Si particles occurs rapidly in the early part of HPT processing ($N \leq 2$). The equivalent strain increases from the center to the edge of the sample with increasing radius (Eq. 2.2), as a function of which the refinement in the edge is found to be maximum, whereas, in the center zone, it was much slower, up to N=2 cycles, Figure 4.10, Figure 4.11(a). Unlike this, the particle size decreases distinctly with an increasing number of turns and increasing sample radius. During HPT, the eutectic phase dissociates into α-Al matrix and Si particles. At the same time, the large primary Si particles are also seen to be broken into refined particles. This apparently leads to an increase in the volume fraction of Si particles distributed in the α-Al matrix. The volume fractions of the α-Al matrix (f_α), eutectic phase (f_{eu}), and Si particles (f_p) measured in the samples as a function of the number of HPT cycles are presented in Figure 4.11(c). It is seen that f_α decreases, whereas f_p and f_{eu} generally increase with the increasing number of HPT cycles. The ratio (d_α / d_p) plotted as a function of the volume fraction of Si particles (f_p) in Figure 4.11(d) shows a decreasing trend and reaches saturation in (d_α / d_p).

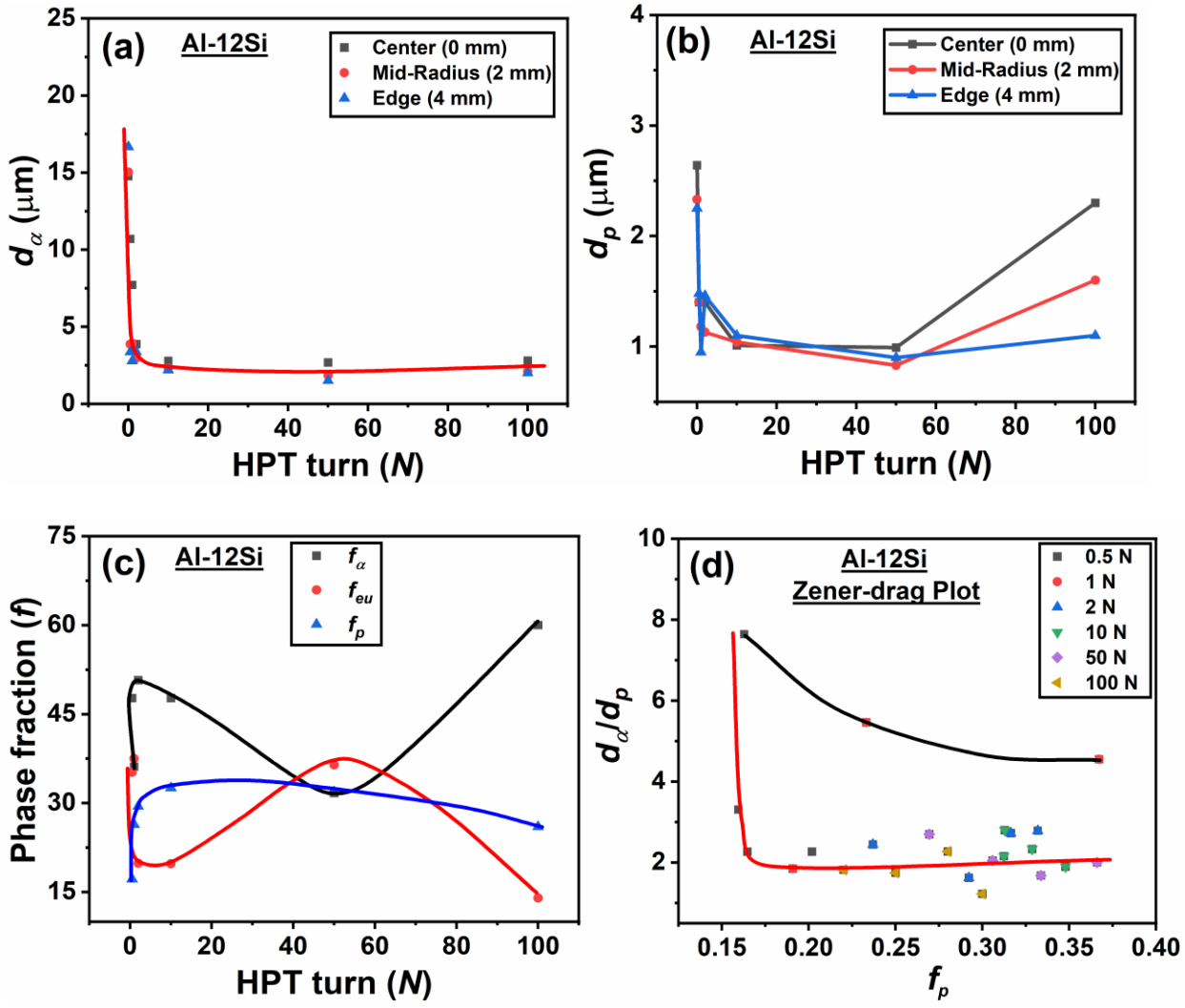
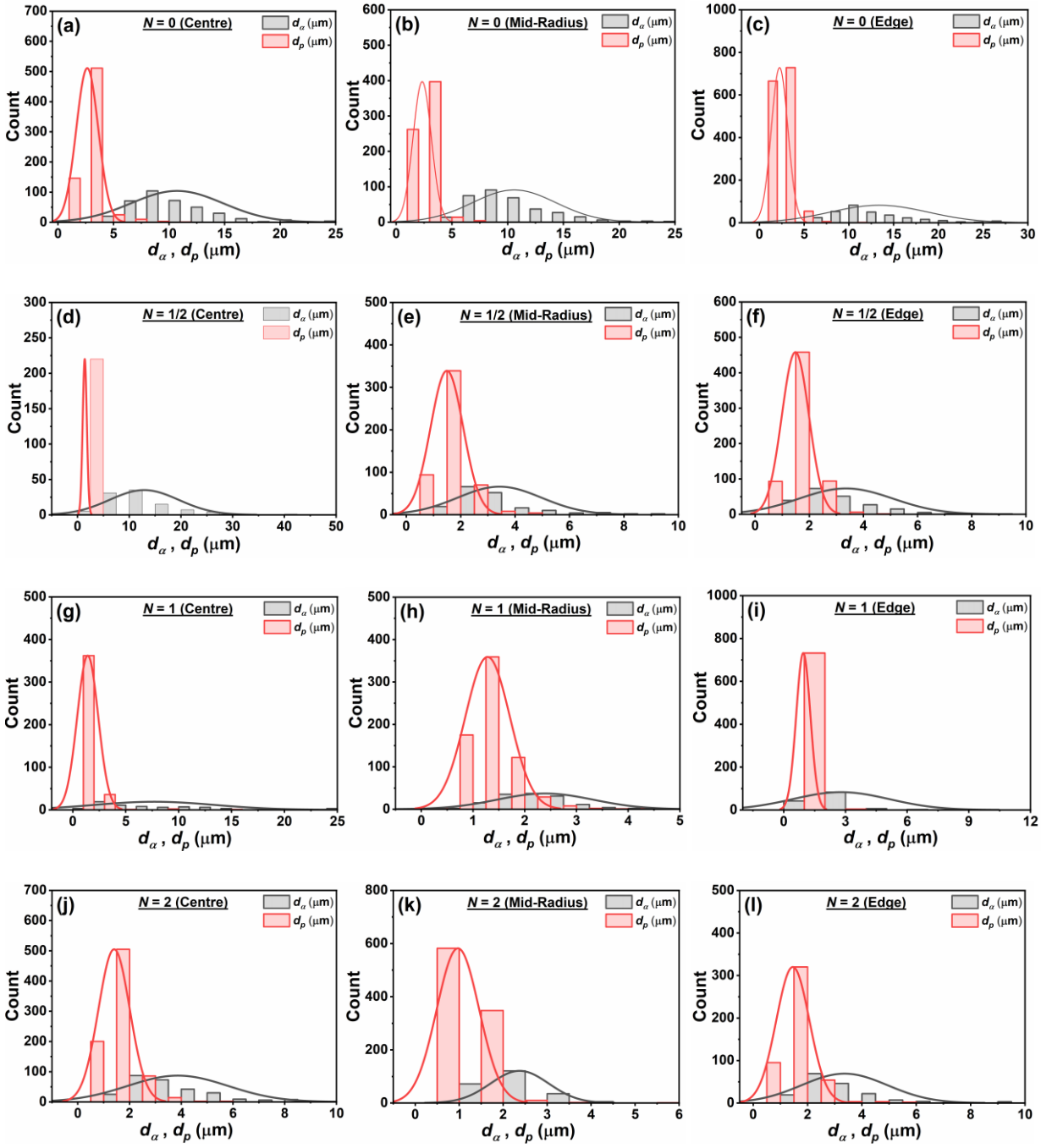


Figure 4.11 : Variation in microstructural parameters, (a) matrix size, (b) silicon particle, and (c) phase fraction as a function of HPT turns (N), (d) Zener plot for all the HPT turns and alloy compositions

The sizes of the matrix and particles exhibit variations depending on the sample location and the number of HPT turns applied. Homogeneity is achieved at the outer edge of the disc-shaped sample. We generated normal distribution plots to assess the impact of HPT turns on the size distribution of silicon particles and the matrix at various locations within the disc

sample. In Figure 4.12(a-r), these plots illustrate the distribution for 0, ½, 1, 2, 10, and 50*N* at different locations: centre, mid-radius, and edge.

It is evident that from 0 to 1*N*, there is a notable difference in size and frequency between the aluminium matrix and silicon particles. This disparity diminishes as we move from the centre to the edge (as shown in Figure 4.12(a-i)), indicative of a coarser matrix and finer silicon particles. Also, there is a shift in the peak of the curves toward each other, which shows clearly that the difference in the size of both matrix and particle decreases with radius. A similar trend is observed in the 10*N* sample, where the differences decrease. However, distributions become uniform after subjecting the sample to 50*N*, Figure 4.12(p-r). This suggests that beyond 50*N*, the matrix size and silicon particle size are nearly identical, resulting in a homogeneous distribution throughout the sample.



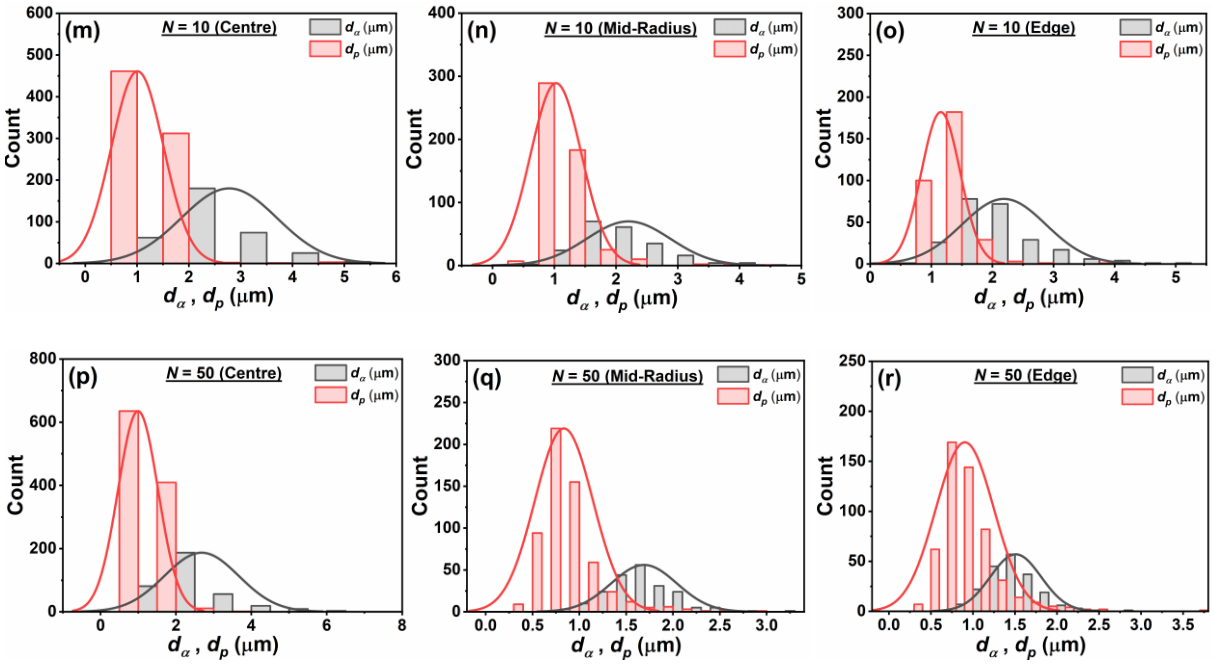


Figure 4.12 : Normal distribution plots of matrix grain size (black) and particle size (red) at different locations of the samples for (a-c) *N*=0, (d-f) *N*=1/2, (g-i) *N*=1, (j-l) *N*=2, (m-o) *N*=10, (p-r) *N*=50 HPT turns

4.2 DEFORMATION BEHAVIOR AND MECHANICAL PROPERTIES

4.2.1 Room Temperature Deformation of Al-Si Alloys

Al-Si alloys of different compositions and processing conditions were deformed at a constant initial strain rate of $10^{-4}s^{-1}$ at room temperature through tensile and compressive tests. The tension tests were conducted up to fracture, whereas the compression tests were terminated within the limit of ~40% strain level for all the samples because of the dominance of frictional stress for further increasing strain. The ultimate stress obtained in the tension test is known as ultimate tensile strength (UTS), but in compression tests, the proof stress at the corresponding uniform strain in tension was considered to be representative of the ultimate compressive strength (UCS).

(a) Mechanical Properties of As-cast Al-Si Alloys at Room Temperature

The engineering stress-engineering strain curves were obtained from tensile and compressive tests at room temperature for hypoeutectic (Al-4Si), eutectic (Al-12Si), and hypereutectic (Al-30Si) alloys, as presented in Figure 4.13(a). It is noted that the tensile yield strength (TYS) and ultimate tensile strength (UTS) increase with increasing wt.% Si (C_{Si}) up to eutectic composition, but beyond the eutectic composition, the strengths decrease with increasing C_{Si} for hypereutectic composition. The total elongation of the samples showed a decreasing trend with increasing C_{Si}, Figure 4.14(a). Figure 4.13(b) shows the micro-Vickers hardness values plotted as a function of silicon content. The hardness increases linearly as a function of C_{Si}. The mechanical properties of different compositions of Al-Si alloy at room temperature are presented in Table 4.4. These variations in TYS, UTS, and total elongation as a function of silicon content are shown in Figure 4.14(a). From Figure 4.14(b), it can be observed that the compressive yield strength (CYS) increases with increasing Si content. However, the increase in CYS as a function of Si content between the hypoeutectic and near-eutectic alloy is more sensitive than that between near-eutectic and hypereutectic alloys, which tends to suggest saturation in CYS. A fixed value of strain (at 10% strain level for hypoeutectic and near-eutectic Al-Si alloys) was selected to get the compressive flow stress (treated as equivalent ultimate compressive strength (UCS)) values to make a comparison of this property among all the samples of different compositions. An examination of the variation in ultimate compressive

strength (UCS) as a function of Si content revealed it to increase and reach saturation with an increase in Si content of Al-Si alloys, as shown in Figure 4.14(b).

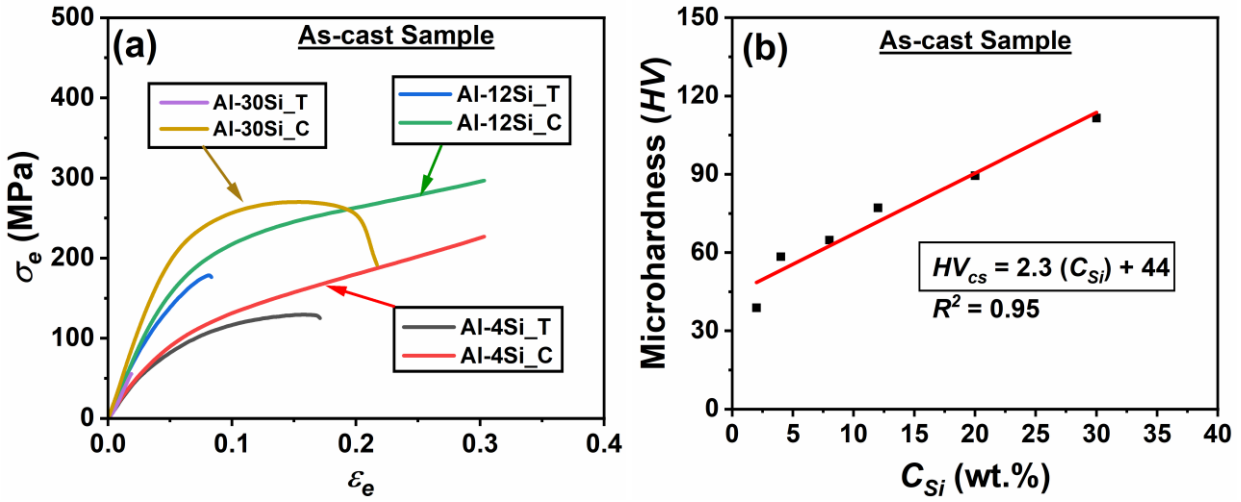


Figure 4.13 : (a) Engineering stress-strain plots for hypoeutectic (Al-4Si), eutectic (Al-12Si), and hypereutectic (Al-30Si) alloys, (b) variation in micro-Vickers hardness values plotted as a function of silicon content

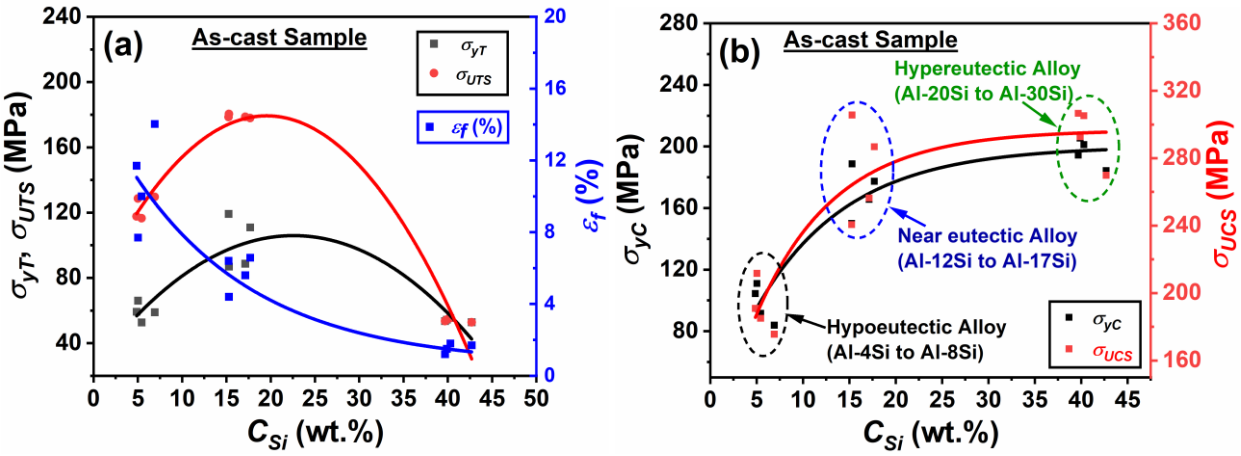


Figure 4.14 : (a) Variation in tensile yield strength (TYS), ultimate tensile strength (UTS), and % total elongation (ε_f) as a function of Si content, (b) variation in compressive yield strength (CYS) and that considered as ultimate compressive strength (UCS) to reflect the flow stress for comparison (proof stress at 10% strain) as a function of Si content

Table 4.4 : Mechanical properties of different Al-Si alloys at room temperature in the as-cast condition

Alloy	*As-Cast condition*						
	Tension			*Compression*			*Hardness (HV)*
	TYS (MPa)	*UTS (MPa)*	*%El*	*CYS (MPa)*	*UCS (proof stress at 10% strain) (MPa)*	*%El*	
Al2Si	-	-	-	-	-	-	38.9±0.9
Al4Si	59	130	14	84	176	-	58.4±1.7
Al8Si	-	-	-	-	-	-	64.8±3.3

Al12Si	89	179	5.6	166	256		77.1±6.5
Al20SI	-	-	-	-	-	-	89.5±12.7
Al30Si	53	53	0	184.3	270	19.2	111.5±20.2

The work hardening rates of all as-cast Al-Si alloys were calculated by differentiating the flow stress (σ) with respect to strain (ε) from the plastic region of the stress-strain plots, viz. ($\theta_H = d\sigma/d\varepsilon$). Figure 4.15 shows the work hardening rates from both tension and compression stress-strain data. The work hardening rate is noted to decrease with increasing strain in all the cases, but in compression, it attains constant or saturation values toward larger strains (stress). The maximum work hardening rate is found in the hypereutectic Al-Si alloys in compression, whereas the hypoeutectic alloy exhibits the minimum work hardening rate in both tension and compression tests. It is also noted that the work hardening rate increases with increasing Si content.

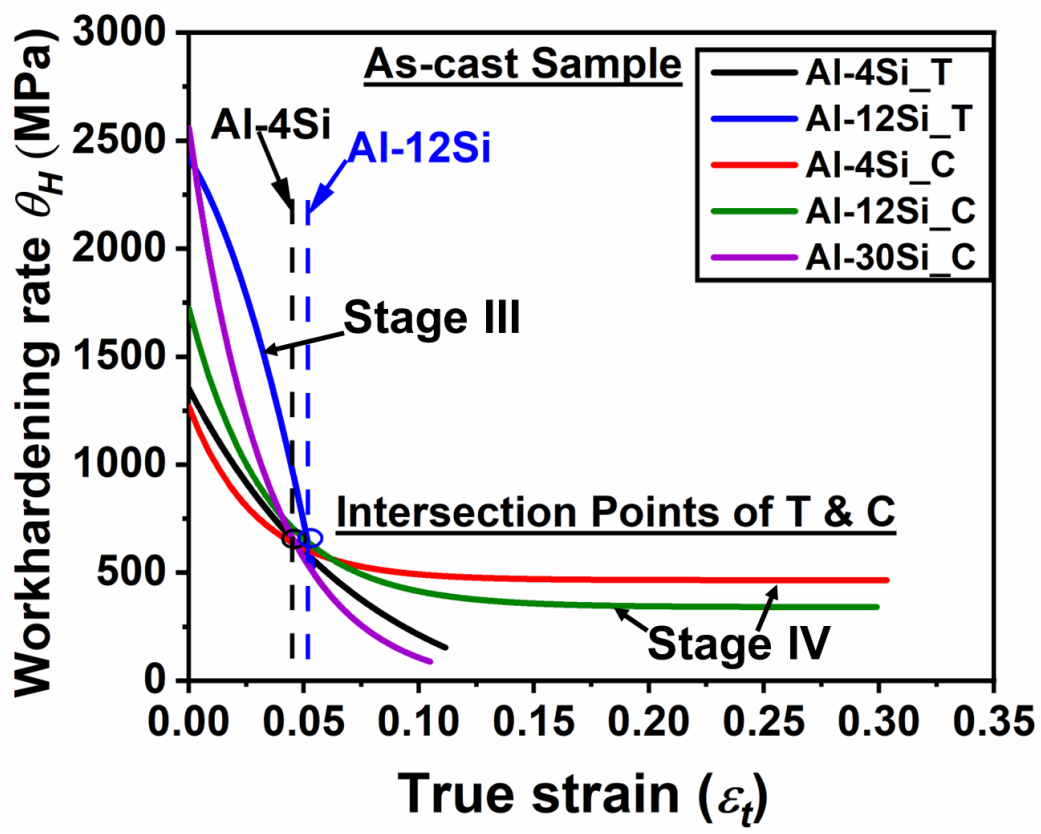


Figure 4.15 : Work hardening rate of Al-Si alloys as a function of strain in tension (T) and compression (C) for as-cast samples

It is noted that the hypoeutectic alloy sample experienced failure along an oblique plane, suggesting a ductile fracture, whereas the other alloys failed through catastrophic brittle fracture, as shown in Figure 4.16(a-c).

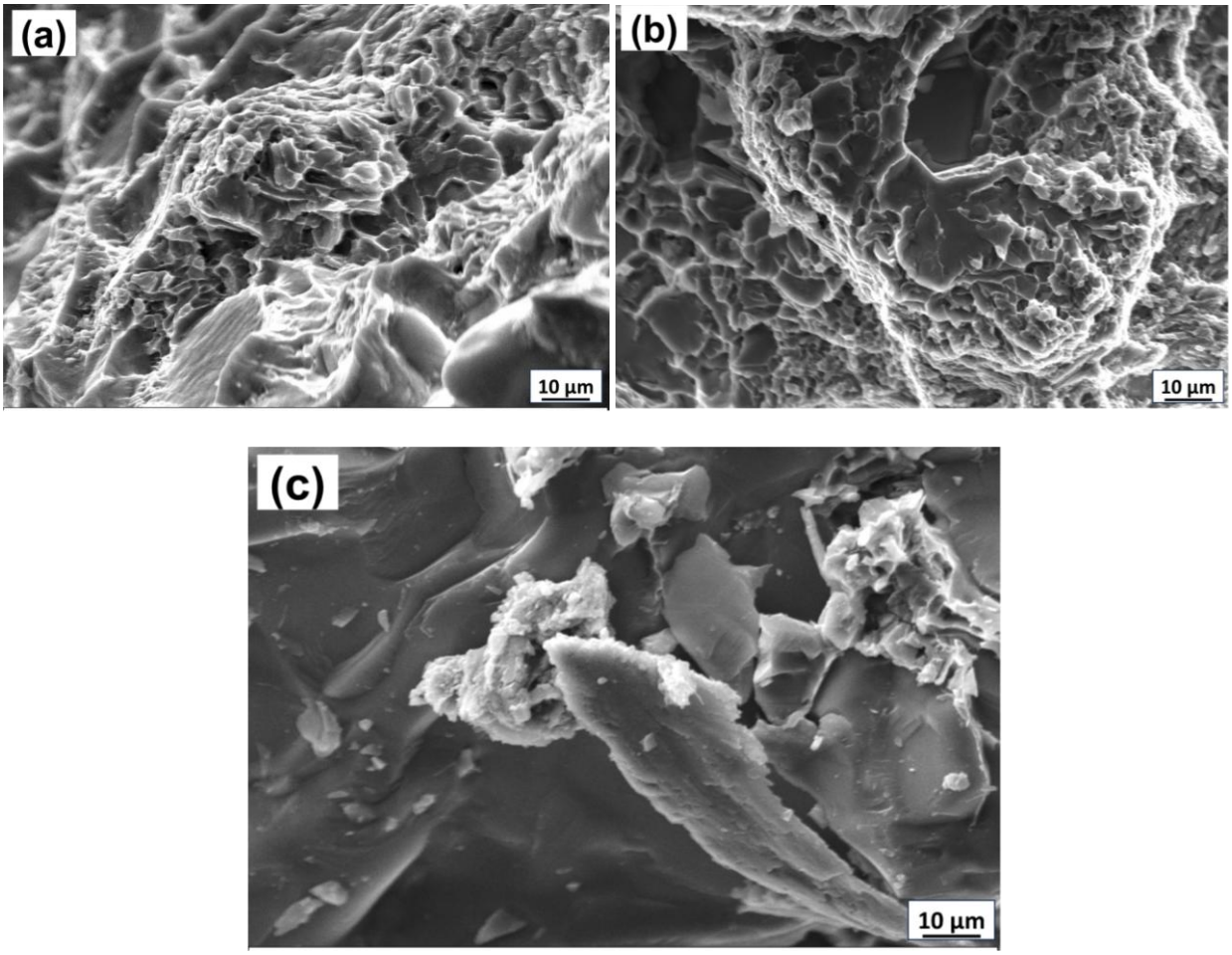


Figure 4.16 : SEM fractographs upon tensile tests of the as-cast hypoeutectic (a) Al-4Si, eutectic (b) Al-12Si, and hypereutectic (c) Al-30Si alloys

The Hollomon-type plots (described in Chapter *3*) were made for all tensile and compressive flow curves. Typical Hollomon-type plots are presented in Figure 4.17(a) to bring out the effects of (i) composition (hypoeutectic and eutectic) and (ii) tensile vs. compressive flow, as marked and given in the legend of the figure. The Hollomon plot reveals three regions in Figure 4.17(a), and the average values of K_H and n_H obtained in different regions, along with the transition stages, are taken for further analysis. The magnitudes of K_H and n_H are found to increase with increasing Si content, and they are also more in compression than in tension.

Also, an attempt was made to explore if there exists any relationship between the Hollomon parameters K_H and n_H themselves. For this purpose, the mean values of these parameters over the different regions were considered, and the same are plotted separately for compressive (K_{HC} vs. n_{HC}; for hypereutectic alloy) and tensile (K_{HT} vs. n_{HT}; for hypoeutectic and eutectic alloys) flow in Figure 4.17(b). Interestingly, K_H and n_H are found to have linear relationships of type:

$$K_H = A_{cs} n_H \pm B_{cs}, \tag{4.4}$$

where A_{CS} and B_{CS} are constants used for as-cast alloys, whose magnitudes are listed as an inset in Figure 4.11(b) for the materials in which this relationship was followed clearly. The subscript '*CS*' represents the as-cast sample.

Hollomon parameters, K_H and n_H, obtained through both tensile and compressive deformation tests on Al-Si alloys, were plotted as a function of silicon content, as illustrated in Figure 4.17(c,d). When examining the strain-hardening exponent in tension (n_{HT}), we observed a

consistent declining trend as silicon content increased, fitting clearly into a linear curve. Notably, we derived two separate linear fits for the n_{HT} data points. In contrast, the n_{HC} data points exhibited a similar decreasing trend, yet a single linear fit was sufficient for this data set, as shown in Figure 4.17(c). The values of the strength coefficient, K_{HT}, and K_{HC} demonstrated an increase with higher silicon content, Figure 4.17(d). K_{HT} data followed a clear linear trend, while K_{HC} data exhibited a more complex second-order polynomial pattern, initially increasing and then decreasing with increasing silicon content.

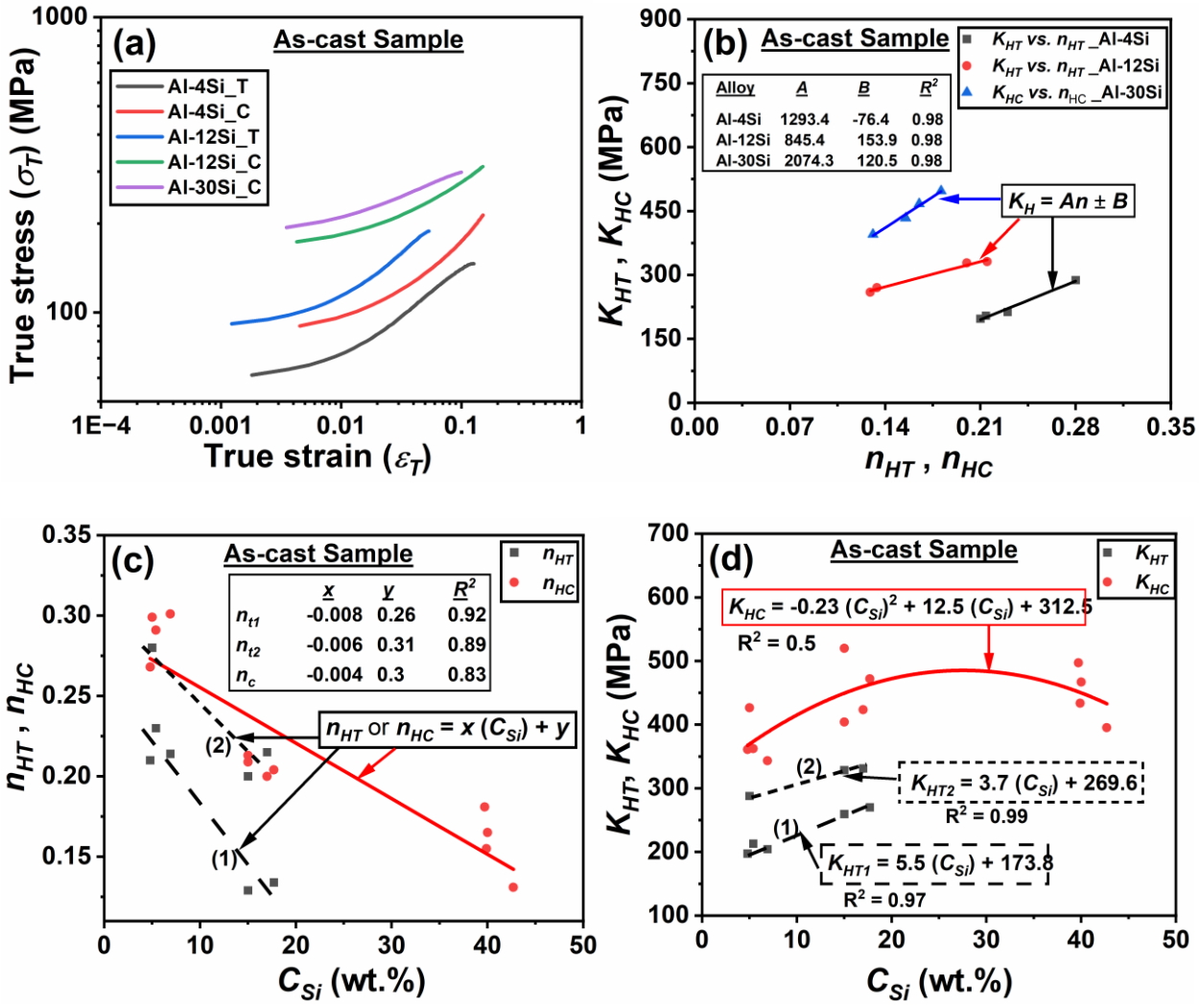


Figure 4.17 : Typical Hollomon plot from the tensile and compressive stress-strain curves of hypoeutectic and eutectic, hypereutectic Al-Si alloys for as-cast (a); (b) plots of the mean value of the Hollomon parameters for compressive (K_{HC} vs. n_{HC}) and tensile (K_{HT} vs. n_{HT}) tests, (c) variation in the strain-hardening exponent (n_H) obtained from tension and compression data as a function of silicon content, and (d) variation in strength coefficient (K_H) obtained from tension and compression data as a function of silicon content (1 and 2 are the regions in Hollomon plot)

The above results were investigated through tensile and compressive deformation at room temperature. Al-Si alloys exhibit asymmetry in work hardening (Figure 4.15), Hollomon parameters (Figure 4.17), and flow strength. In this context, "asymmetry" signifies that the behaviour of the material during deformation differs between tension and compression tests, a phenomenon extensively explored by numerous researchers across various metals and alloys. The difference in yield strength values in tension (σ_{yT}) and compression (σ_{yC}) is defined as yield strength asymmetry (σ_{yA}=σ_{yC}-σ_{yT}), which was plotted as a function of silicon content. A small change in silicon content can influence the flow properties in tension and compression differently. The yield strength asymmetry exhibited an increasing trend with higher silicon

content, following a linear relationship, as demonstrated in Figure 4.18. Notably, the maximum observed asymmetry reached 151 MPa in the case of the hypereutectic Al-Si alloy.

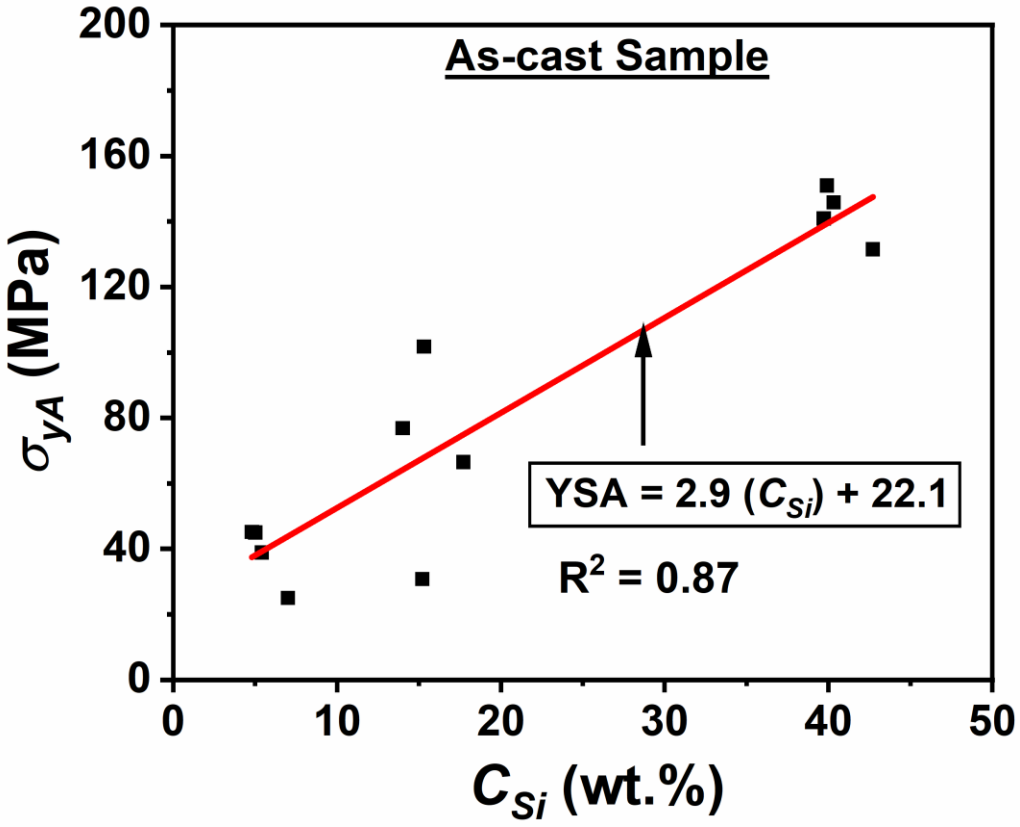


Figure 4.18 : Yield strength asymmetry (σ_{yA}) plot as a function of silicon content (C_{Si}) in the as-cast Al-Si alloys

Flow stresses (σ) at selected constant strain (ε) levels (0.2%, 5%, 10% with R^2 = 0.83, 0.83, 0.8 respectively) were plotted as a function of the inverse square root of grain size (d) in the form of Hall-Petch (H-P) type relationship (Eq. 3.9). Compression test data, as illustrated in Figure 4.19(a), follow the H-P type relationship, but the tensile test data did not follow such a relationship. The obtained HP parameters σ_{HP} and k_{HP} from the H-P plot in Figure 4.19(a) were plotted as a function of strain by considering other strain levels that were not used in HP plots, Figure 4.19(b).

Initially, it is noteworthy that σ_{HP} decreases with increasing strain at lower strain levels (1), while k_{HP} exhibits an increasing trend with higher strain levels. However, in the higher strain region (2), a reversal of this trend is observed, with σ_{HP} increasing as strain increases and k_{HP} reaching a saturation point, accompanied by a slight decrease in trend as strain continues to rise. The effect of strain on σ_{HP} and k_{HP} can be expressed by Eqs.(4.5a), (4.5b), and Eqs.(4.6a), (4.6b), respectively.

$$\sigma_{HP1} = -562.1(\varepsilon) + 13.4, \qquad R^2 = 0.87 \qquad (4.5a)$$

$$\sigma_{HP2} = 568.4(\varepsilon) - 24.3, \qquad R^2 = 0.98 \qquad (4.5b)$$

$$k_{HP1} = 113.6\ln(\varepsilon) + 1355, \qquad R^2 = 0.97 \qquad (4.6a)$$

$$k_{HP2} = -936.8(\varepsilon) + 1083, \qquad R^2 = 0.94 \qquad (4.6b)$$

It is evident that the flow stress in both tension and compression is influenced by several key factors, including grain size, silicon content, and phase fractions within Al-Si alloys.

Moreover, we sought to explore the combined impact of particle size and volume fraction represented by interparticle spacing (Λ) on the yield strength in both tensile and compressive deformations. The interparticle spacing (Λ) can be determined using the following equation (Z. Guo and W. Sha, 2002):

$$\Lambda = \left(1.23\sqrt{\frac{2\pi}{3f_p}} - 2\sqrt{\frac{2}{3}}\right)\left(l/2\right), \tag{4.7}$$

In this equation, f_p represents the particle volume fraction, while l corresponds to the length or is considered as the diameter of the Si particle. The yield strength values in tension and compression were analysed as a function of the inverse square root of the interparticle spacing and plotted in the form of an H-P plot, as shown in Figure 4.19(c). The tensile yield strength data exhibited a reasonable H-P relationship, while the yield strength values in compression did not exhibit the same behaviour. Additionally, we computed the flow stresses independently by utilizing the Hollomon parameters and H-P parameters derived from the compression test. These results were then graphically represented, illustrating the relationship between them, Figure 4.19(d). A linear fit was applied to these data, revealing the interplay between work hardening and grain boundary strengthening effects.

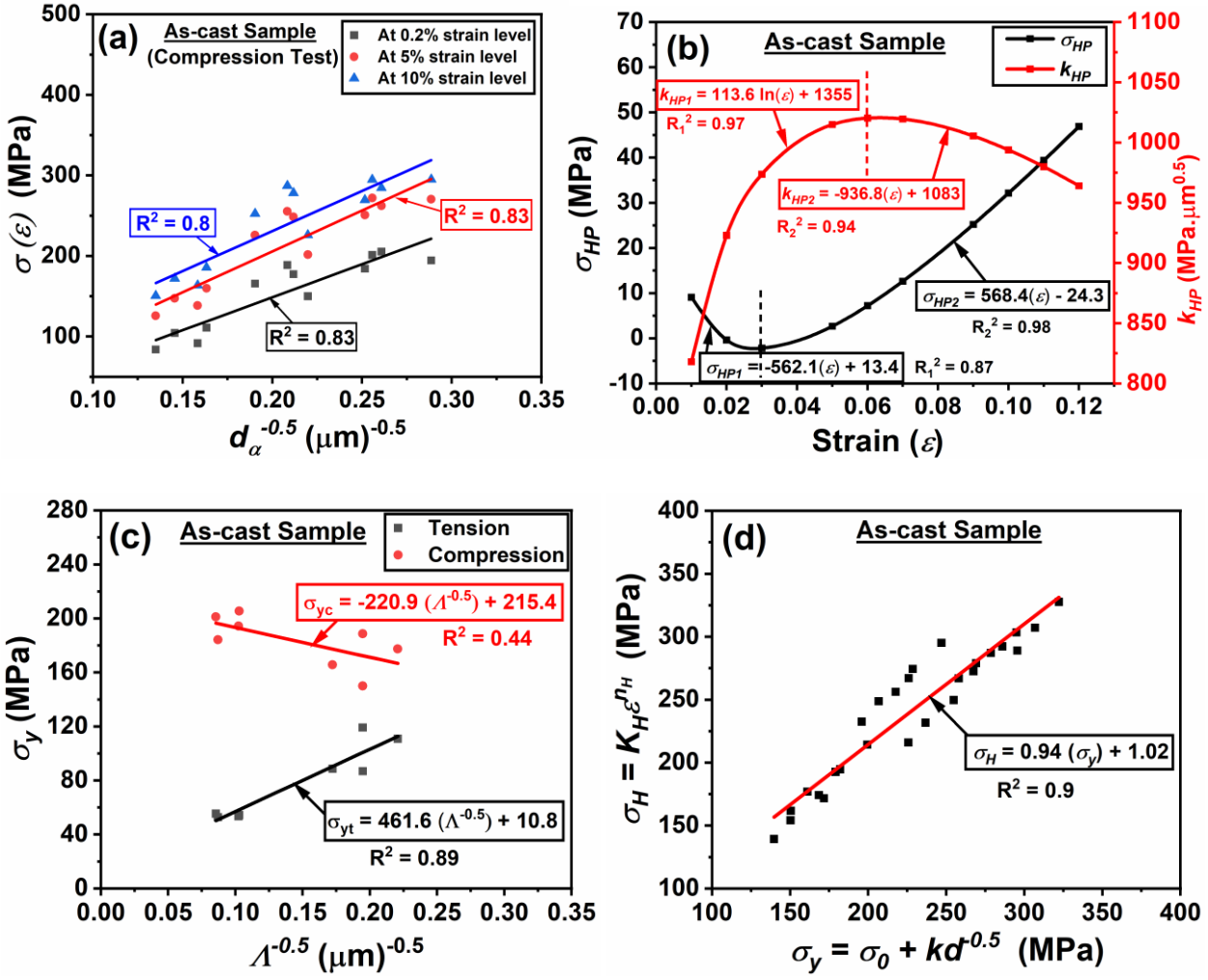


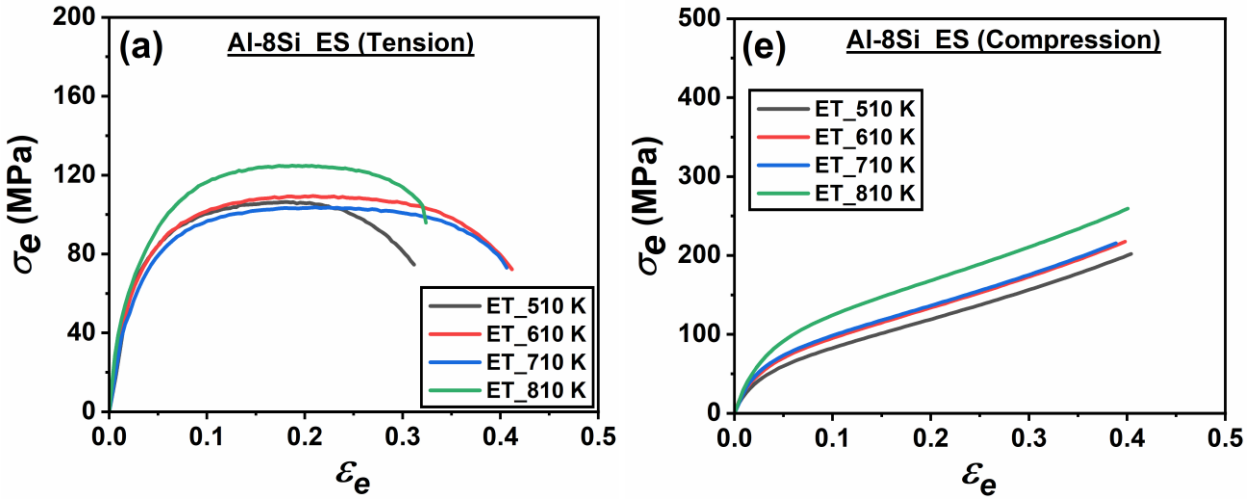
Figure 4.19 : (a) Hall–Petch type plots at selected strain levels (proof stresses at 0.2% (yield point), 5%, and 10% strains) of the compression test data of all Al-Si alloys, (b) variation in HP parameters σ_{HP} and k_{HP} as a function of strain, (c) HP type plot of yield strength in tension and compression tests and interparticle spacing, and (d) comparison plot of flow stresses calculated by using Hollomon and Hall-Petch parameters for compression test

(b) Mechanical Properties of Extruded Al-Si Alloys at Room Temperature

Tensile and compressive tests at room temperature were conducted on extruded Al-Si alloys, employing a strain rate of $10^{-4}s^{-1}$. Additionally, microhardness measurements were made for these alloys. These tests were performed on the samples of different alloy compositions (Al-8Si to Al-30Si) processed at various extrusion temperatures (510K-810K). The corresponding results for yield strength, ultimate strength, total elongation, and microhardness values can be found in Table 4.5.

The stress-strain plots in Figure 4.20 illustrate the results of uniaxial tension (Figure 4.20(a-d)) and compression (Figure 4.20(e-h)) tests conducted at room temperature. In the lower extrusion temperature range, an increase in silicon content up to Al-20Si led to increasing TYS and UTS values, which then decreased for the highest silicon content alloy of the Al-30Si. Similarly, in the higher extrusion temperature range, the TYS and UTS increased with the silicon content up to the eutectic Al-12Si alloy, followed by a decrease for higher silicon-containing Al-Si alloys. The total elongation exhibited an improvement with increasing silicon content from hypo to eutectic compositions, but then decreased for hypereutectic Al-Si alloys under the lowest and highest extrusion temperature conditions. For intermediate extrusion temperatures, elongation consistently decreased as a function of increasing silicon content in the alloy. The same trend was observed for uniform strain and necking strain with respect to silicon content and extrusion temperatures.

During the compression test, it was observed that the compressive yield strength (CYS) initially increased with Si content up to Al-20Si and then decreased for the hypereutectic Al-30Si alloy, with the exception of the lowest extrusion temperature employed. However, at the lowest extrusion temperature, the CYS showed a continuous increase with higher silicon content. Conversely, the ultimate compressive strength (UCS), which represents the proof stress calculated based on the uniform strain during tensile deformation, reached its maximum for the eutectic alloy and decreased as the silicon content increased for all extrusion temperatures.



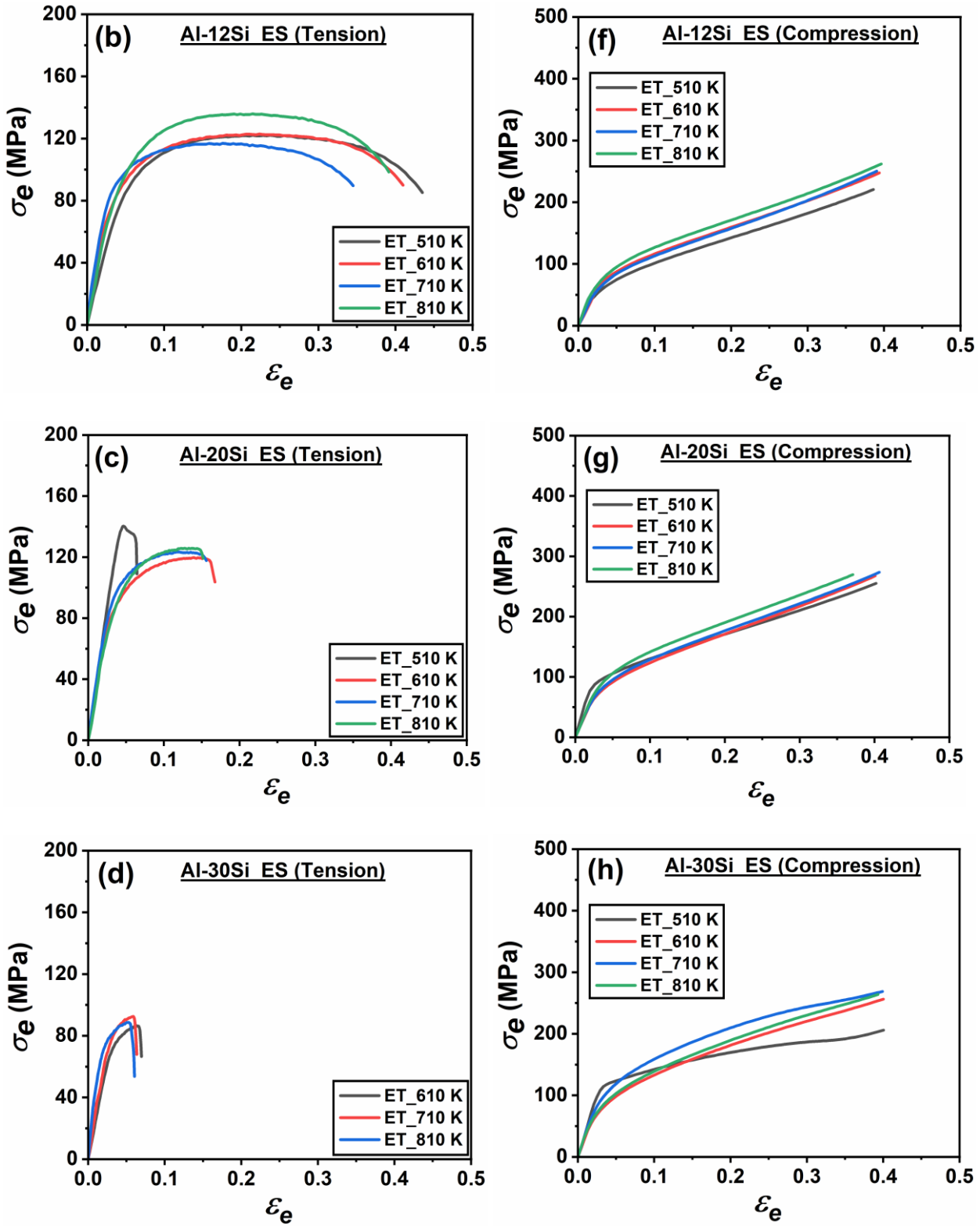
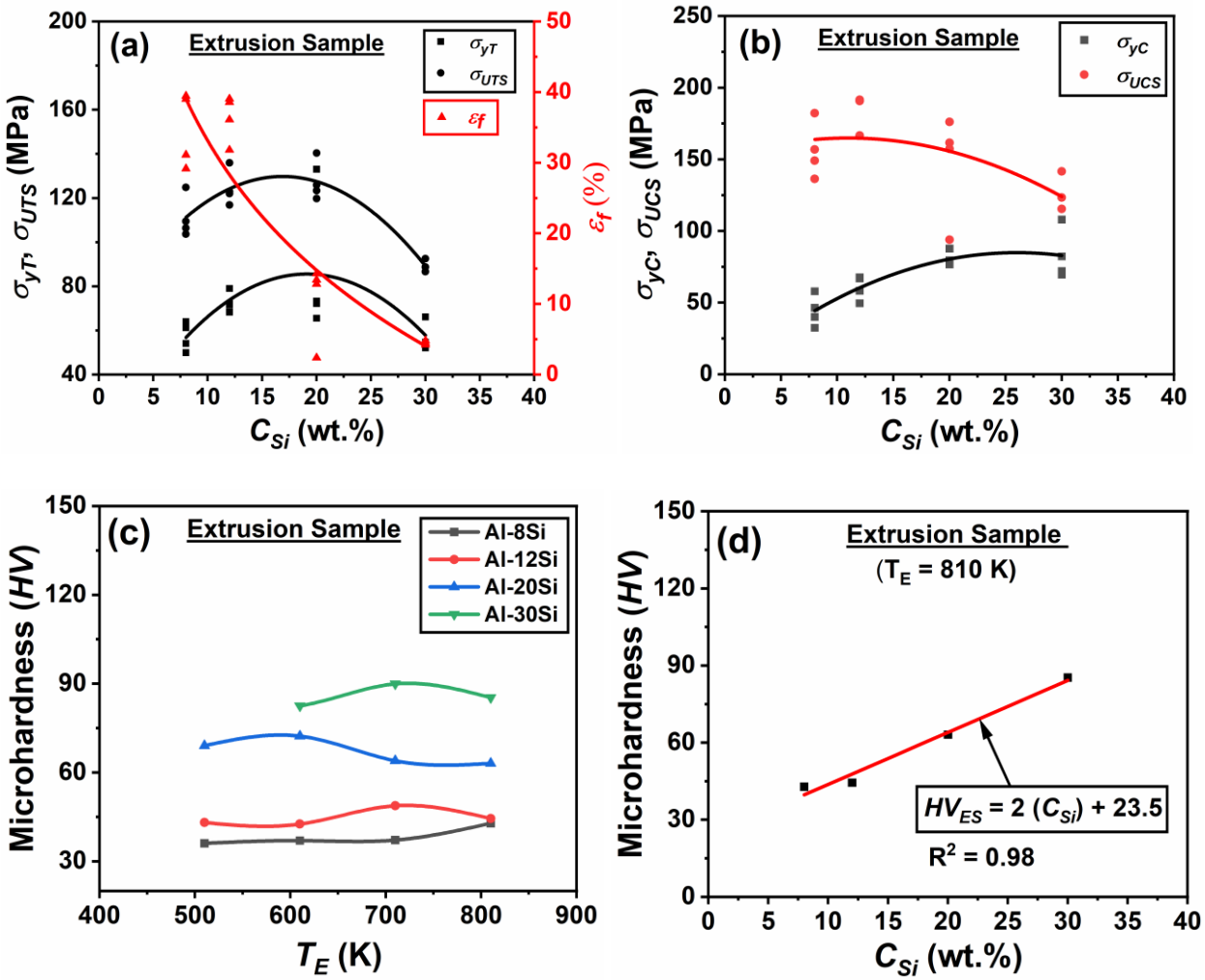


Figure 4.20 : Room temperature stress-strain curves obtained from tension tests (a-d), and compression tests (e-h) of different Al-Si alloys extruded at selected temperatures

The variations in mechanical properties obtained from tensile and compression tests were analysed in relation to the Si content for all the processed Al-Si alloys at different extrusion temperatures, and the results are presented in Figure 4.21(a-e). The nature of variation in TYS and UTS as a function of Si content was noted to be the same, whereas a continuous decreasing trend was found for the elongation, Figure 4.21(a). Notably, the maximum TYS of 133MPa was achieved with the hypereutectic Al-20Si alloy extruded at 510K, while the minimum of 50MPa was observed in the hypoeutectic Al-8Si alloy extruded at 710K. Similarly,

the highest UTS of 140MPa was found in the Al-20Si alloy extruded at 510K, while the lowest of 87MPa was observed in the Al-30Si alloy extruded at 610K. Additionally, the maximum total elongation of 40% was achieved in the hypoeutectic Al-8Si alloy extruded at 710K. Figure 4.21(b) shows the variation in CYS and UCS as a function of Si content, which reveals that both CYS and UCS first increase with the increase in Si content and then decrease with the further increase in Si content. The hypereutectic Al-30Si alloy extruded at 510K exhibited the highest CYS of 108MPa, while the hypoeutectic Al-8Si alloy extruded at 510K showed the minimum value. Furthermore, the highest UCS of 192MPa was recorded for the eutectic Al-12Si alloy extruded at 810K, with the lowest value observed in the hypereutectic Al-20Si alloy extruded at 510K.

A small variation in hardness was observed with respect to the extrusion temperature, Figure 4.21(c), while a more significant change was evident with varying silicon content, Figure 4.21(d). The microhardness varies linearly as a function of the Si content of Al-Si alloys extruded at the maximum temperature of 810K. Moreover, a clear relationship between hardness and total elongation of the tensile samples was identified, independent of the alloy composition, Figure 4.21(e). As the elongation increased, the hardness decreased, indicating that higher ductility resulted in a softer alloy. For a comprehensive overview, the range of hardness values at different extrusion temperatures can be found in Table 4.5.



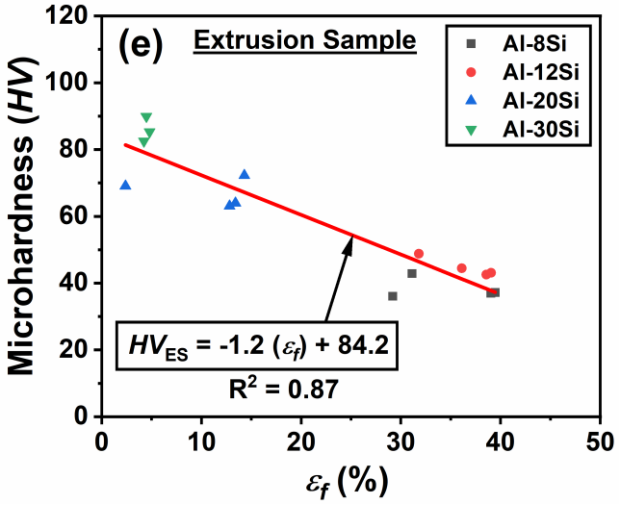


Figure 4.21 : (a) Variation in tensile yield strength (σ_{yT}), ultimate tensile strength (σ_{UTS}), and % total elongation (ε_f) as a function of Si content, (b) variation in compressive yield strength (σ_{yC}) and that considered as ultimate compressive strength (σ_{UCS}) to reflect the flow stress for comparison (proof stress at uniform strain level in tension) with the yield strength as a function of Si content, variation in microhardness as a function of extrusion temperature and alloy composition (c), (d) wt.% Si for maximum extrusion temperature (810K) condition, and (e) % total elongation (ε_f) irrespective of alloy condition

Figure 4.22(a) illustrates the typical work hardening rate (θ_H) plots in tension and compression for various compositions of Al-Si alloy, ranging from hypoeutectic to hypereutectic, including eutectic compositions. Figure 4.22(b) presents the effect of extrusion temperature on work hardening behaviour in tension and compression tests of hypoeutectic Al-8Si alloy. It is noteworthy that the work hardening decreases rapidly in tension for all extrusion conditions and alloy compositions, whereas in compression, it decreases gradually, reaches a saturation point, and then starts to increase with an increase in strain. Furthermore, the study reveals that the work hardening rate is directly proportional to the silicon content, as an increase in silicon leads to higher work hardening. The highest work hardening rate is observed in tension for the hypereutectic Al-20Si alloy, while the hypoeutectic Al-8Si alloy exhibits the lowest work hardening rate in both tension and compression. Overall, regardless of conditions, tension shows a higher maximum work hardening rate than compression.

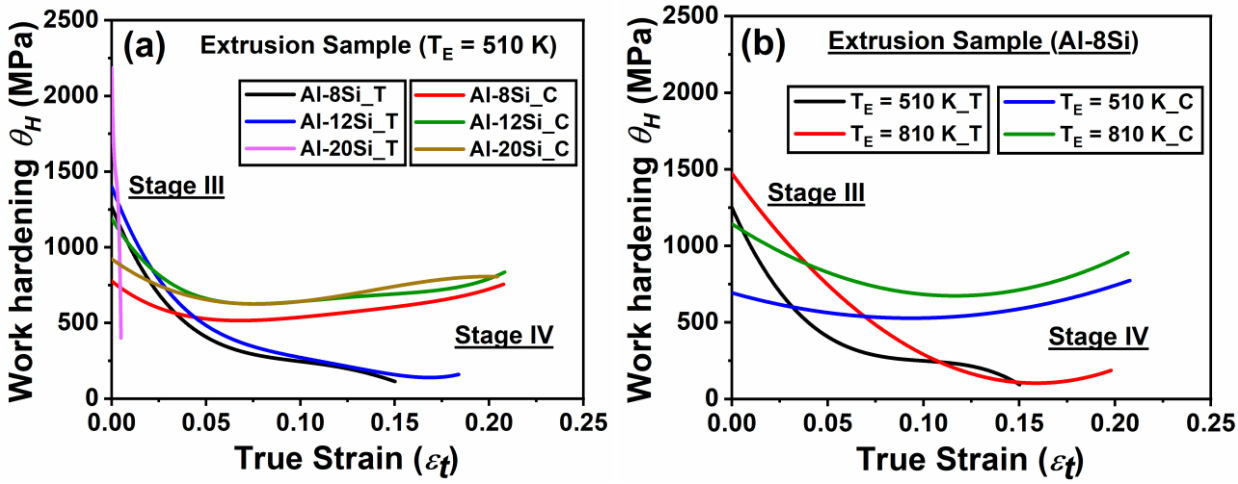


Figure 4.22 : Variation in work hardening rate as a function of strain in tension (T) and compression (C) (a) for hypoeutectic, eutectic, and hypereutectic Al-Si alloys extruded at 510K, (b) for hypoeutectic Al-8Si alloy extruded at different extrusion temperatures (given in the legends of the figure)

The variation in flow stress with strain was analysed using the Hollomon-type relationship for different extrusion conditions and alloy compositions to understand the

deformation mechanism at room temperature. Figure 4.23(a,b) depicts the typical Hollomon-type plots, highlighting the impact of alloy composition, tension, and compressive flow behaviour, and extrusion condition. Notably, the Hollomon plot reveals two regions for tension and three regions for compression. The Hollomon parameters (K_H, n_H) were calculated by taking the average of different regions for tension and compression of the plot. The values of K_H and n_H were noted to be higher in compression than in tension, irrespective of all conditions. In most alloy compositions, a linear relationship was observed between K_H and n_H values separately for tension and compression. Interestingly, the plot of K_H and n_H values for different compositions, extrusion temperature, and tension-compression combined exhibits a linear relationship, as shown in Figure 4.23(c). The same can be expressed by the following equation with R^2=0.9:

$$K_H = A_{ES} n_H \pm B_{ES}, \tag{4.8}$$

where A_{ES} and B_{ES} are the constants for extrusion samples whose magnitudes are 943 and 31, respectively.

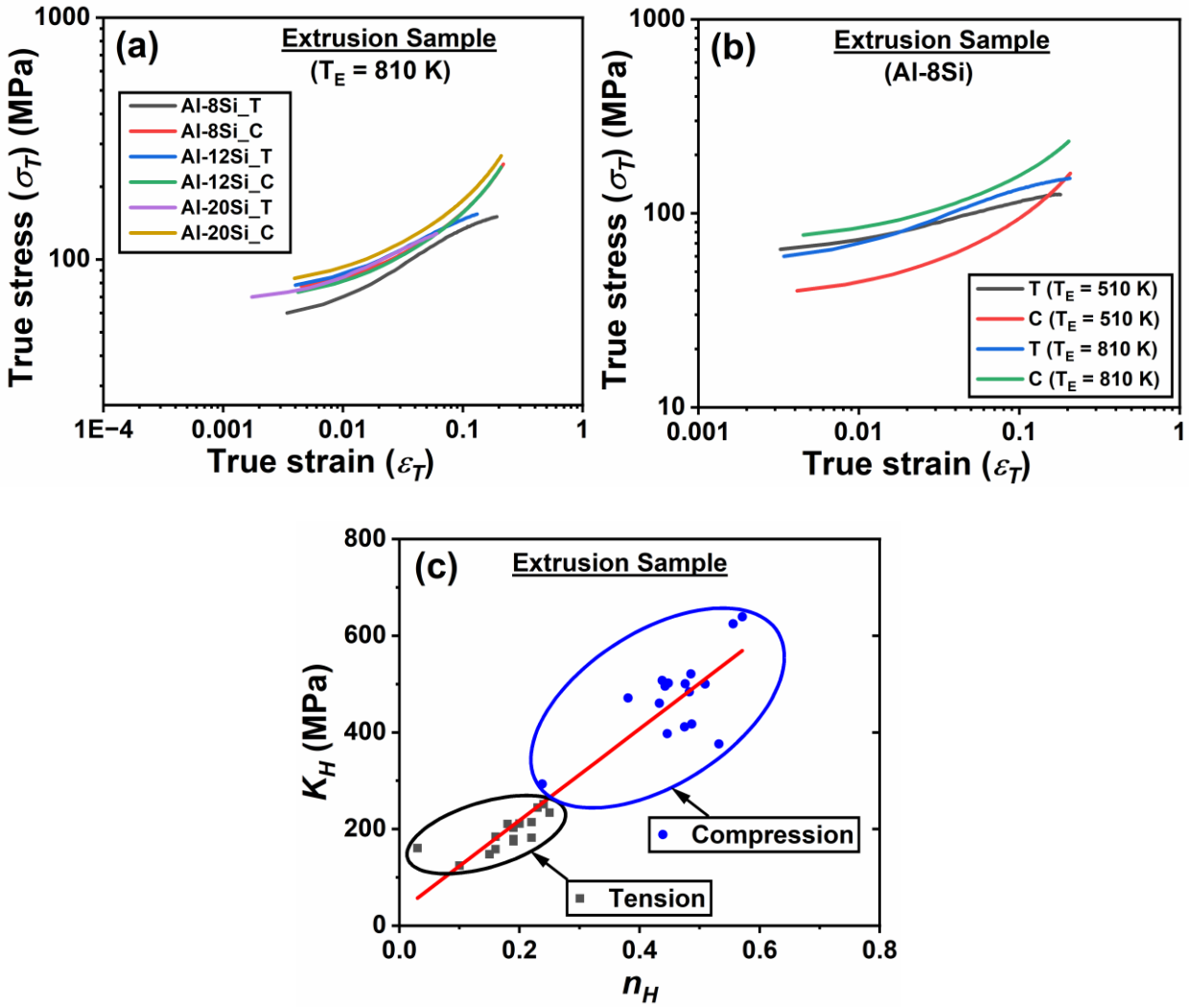


Figure 4.23 : Typical Hollomon-type plots obtained from tension and compression curves of different alloy compositions extruded at 810K (a), (b) for different extrusion temperatures of Al-8Si alloy, and (c) the mutual plot of mean values of Hollomon parameters for extrusion samples (K_H,n_H), independent of extrusion temperature and alloy composition

Table 4.5 : Range of mechanical properties obtained from tension, compression, and micro-Vickers hardness tests of Al-Si alloys processed by hot extrusion

Al-Si Alloys	*Extrusion Processed Alloys*					
	Tension			*Compression*		*Hardness (HV)*
	TYS (MPa)	*UTS (MPa)*	*%El*	*CYS (MPa)*	*UCS (proof stress at uniform strain) (MPa)*	
Al8Si	50-64	104-125	29-40	32-58	136-182	36-43
Al12Si	68-79	117-136	31-39	50-68	167-192	43-49
Al20Si	66-133	120-140	3-14	76-88	94-176	63-72
Al30Si	52-66	87-93	4-5	70-108	115-142	83-90

The H-P type plots were made from the grain size, hardness, tensile, and compression test data obtained from the extruded samples of different compositions and extrusion temperatures. It was found that the H-P plot was followed by only alloys that were extruded at 710K in tension, but the rest of the conditions did not satisfy the H-P relationship. Figure 4.24 shows such a plot between yield strength (σ_y) and $d_\alpha^{-0.5}$, which can be expressed by the Eq.(4.9) given within the inset of this figure.

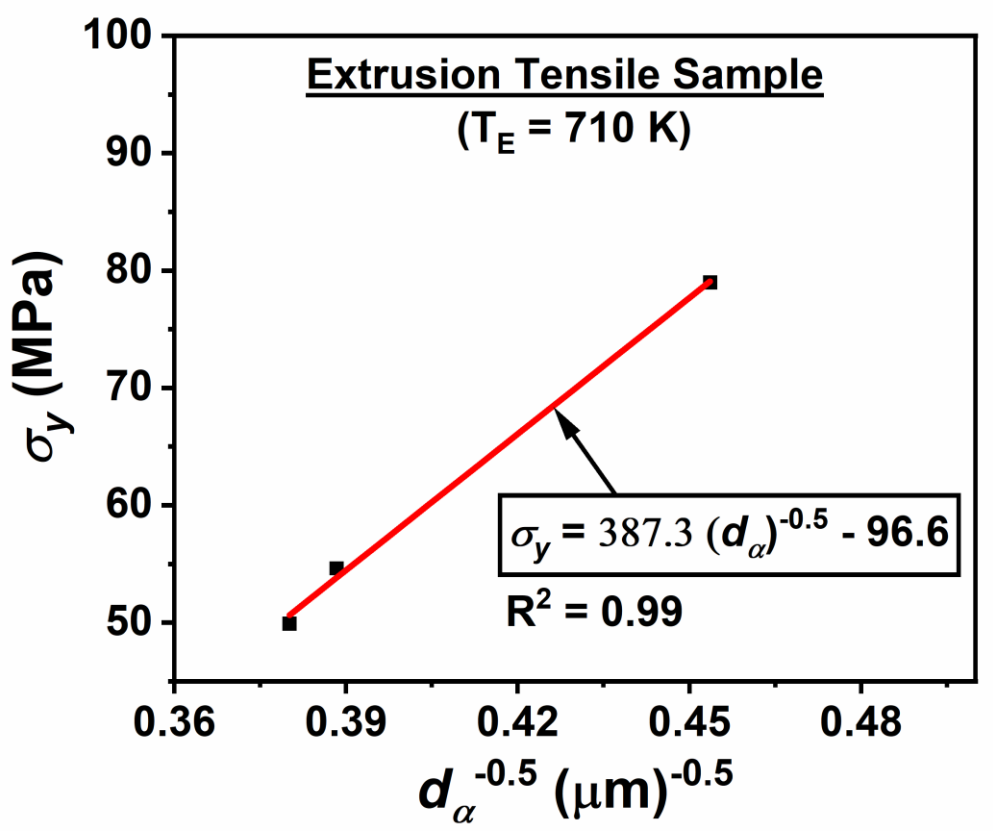


Figure 4.24 : Hall-Petch type plot for the Al-Si alloys extruded at 710K

(c) Mechanical Properties of FSPed Al-Si Alloys at Room Temperature

The stress-strain curves shown in Figure 4.25(a) were obtained from the room temperature tensile tests conducted on Al-Si alloys of different compositions subjected to three-

pass friction stir processing (FSP). The corresponding plots for TYS (σ_{yT}), UTS (σ_{UTS}), and % elongation (ε_f) as a function of Si content are shown in Figure 4.25(b). The results delineate that the σ_{yT} initially increases with the increase in silicon content, reaching a peak value of 115.4MPa for the Al-20Si alloy. However, beyond the Al-20Si alloy composition, the σ_{yT} starts to decrease, reaching a minimum of 73.5MPa for the hypoeutectic Al-8Si alloy. In terms of σ_{UTS}, the eutectic Al-12Si alloy exhibits the highest value of 185MPa, while the hypereutectic Al-30Si alloy shows the lowest value of 141MPa, but it may be noted that the sample of this composition did not undergo significant plastic deformation but failed upon reaching the yield point. As far as elongation is concerned, the hypoeutectic Al-8Si alloy demonstrates a large elongation of about 30%, but as the silicon content increases, the elongation decreases to almost 0% in the case of Al-30Si alloy. Given as inset in Figure 4.25(b) is the equation (Eq. 4.10) for elongation as a function of Si content in wt.% (C_{Si}). Figure 4.25(c) illustrates the variation in microhardness of the three-pass FSP samples as a function of Si content. Interestingly, the hardness varies linearly with silicon content, revealing a straight-line relationship (Eq. 4.11).

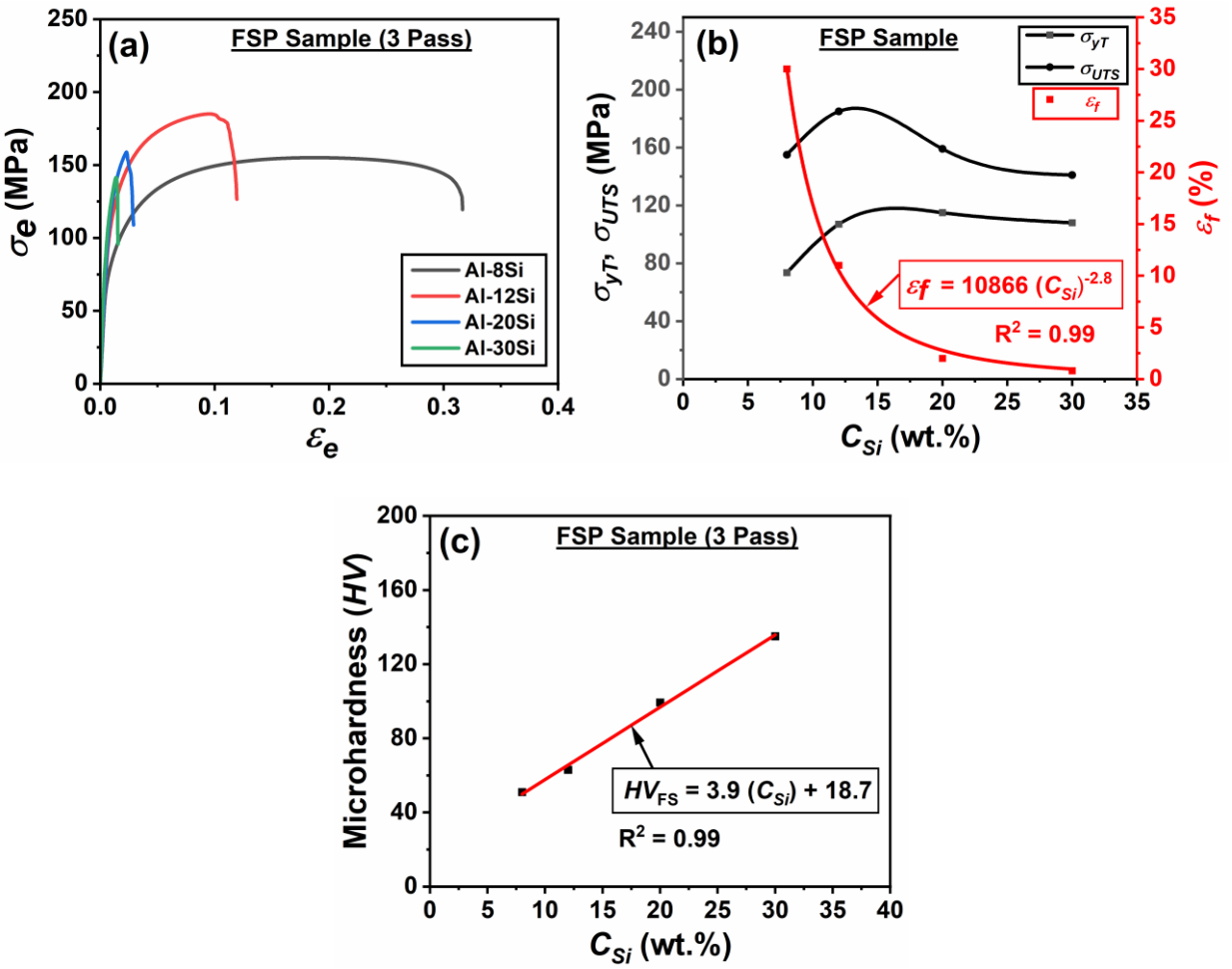


Figure 4.25 : (a) Stress-strain curves obtained from tensile tests at room temperature, (b) variation in TYS (σ_{yT}), UTS (σ_{UTS}), and % elongation (ε_f) obtained from the stress-strain curves of tensile tests, (b) microhardness plotted as a function of Si content of the different Al-Si alloys processed under three-pass FSP condition

Figure 4.26 illustrates the work-hardening behaviour from the tensile test of Al-Si alloys processed through FSP. The observed pattern of work hardening rate (θ_H) exhibits an initial sharp decrease (Stage III) with increasing strain across all alloy compositions, followed by near stabilization (Stage IV) for hypoeutectic and eutectic alloys, suggesting Stage III of rapid drop and saturation of Stage IV type behaviour. Notably, the highest level of work hardening is achieved in the hypereutectic Al-30Si alloy, while the lowest is recorded for the hypoeutectic Al-8Si alloy. This investigation establishes a direct effect of silicon content on work hardening rate, leading to an increase in work hardening response with increasing silicon content.

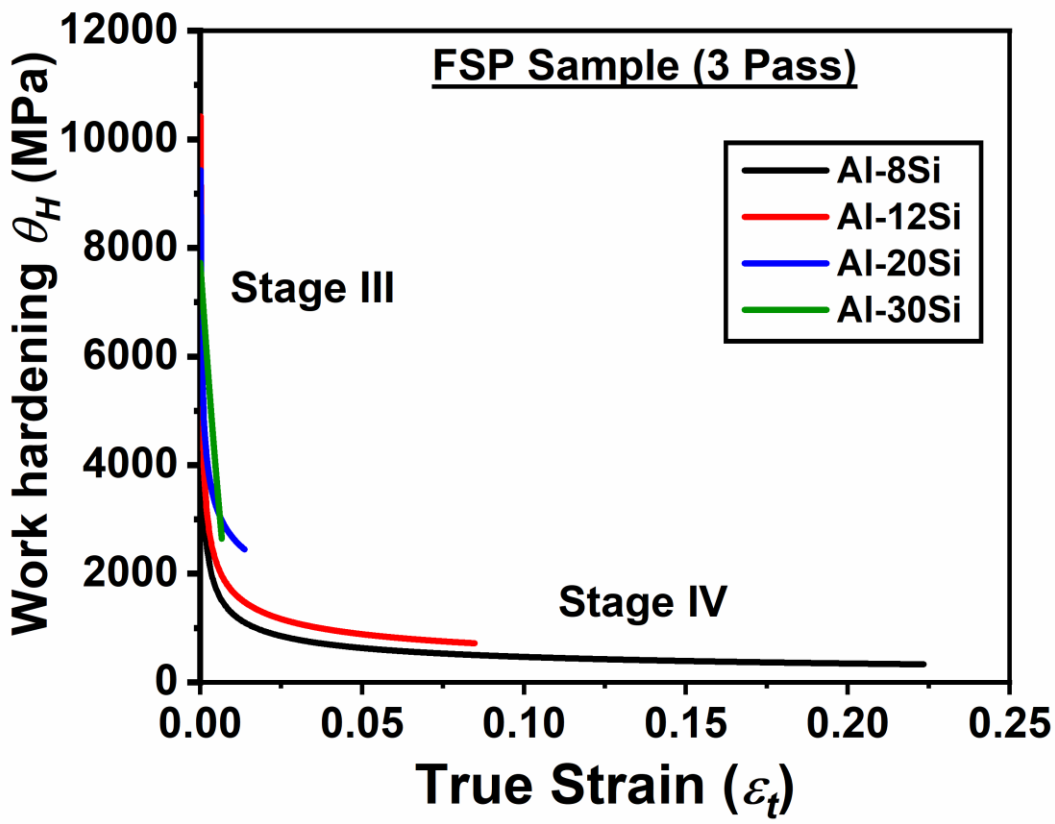


Figure 4.26 : Work hardening plot with true strain, obtained from the stress-strain curves of tensile tests of different Al-Si alloys processed to three-pass FSP

The study involved further analysis of stress-strain curves obtained from FSP of various Al-Si alloy compositions. The resulting data was used to generate typical Hollomon-type plots, as presented in Figure 4.27(a). It is noted that the Hollomon plots show two typical regions, which were used to determine the average values of K_H and n_H. Additionally, Figure 4.27(b) displays the variation of Hollomon parameters, K_H and n_H, as a function of silicon content. This plot enables examining the relationship between silicon content and the Hollomon parameters. It is observed that the magnitude of n_H is decreased with an increase in silicon content, whereas the K_H plot shows the opposite trend. The maximum value of K_H was obtained for hypereutectic Al-30Si alloy and the minimum for hypoeutectic Al-8Si alloy. In contrast, the maximum value of n_H was found for hypoeutectic Al-8Si alloy and the minimum for hypereutectic Al-20Si alloy.

Furthermore, Figure 4.27(c) illustrates an inter-relationship plot, representing the mean values of Hollomon parameters (K_H, n_H) for FSPed samples. Notably, this plot is independent of specific conditions. Similar to the previous results for as-cast and extrusion conditions, K_H and n_H are found to have a linear relationship for FSPed alloy of type:

$$K_H = A_{FS} n_H \pm B_{FS}, \tag{4.12}$$

where A_{FS} and B_{FS} are constants, whose magnitudes are listed as an inset in Figure 4.27(c), the subscript '*FS*' represents the three-pass FSP processed sample.

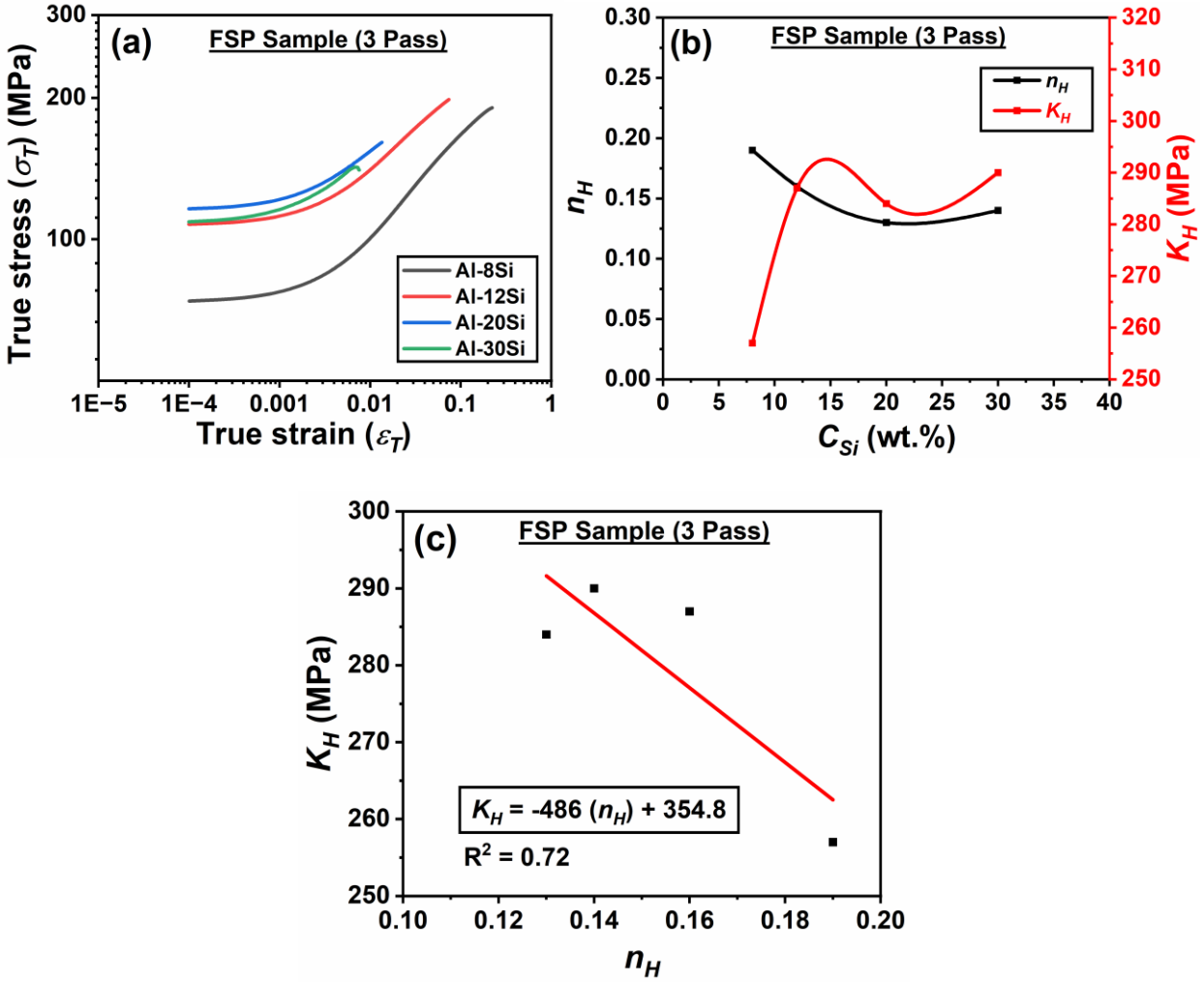


Figure 4.27 : Hollomon type plots obtained from tensile stress-strain curves of three pass FSP processed alloys of different compositions (a), (b) Hollomon parameters, K_H, n_H plotted as a function of silicon content, and (c) the inter-relationship plot of mean values of Hollomon parameters for FSPed samples (K_H, n_H) independent of alloy composition

Also, the Hall-Petch type relationship was explored between the tensile yield strength and grain size data obtained from three-pass FSP processed Al-8Si, Al-12Si, Al-20Si, and Al-30Si alloys. Interestingly, the data shown in Figure 4.28 follows the H-P plot with a linear curve fitting and a good correlation coefficient.

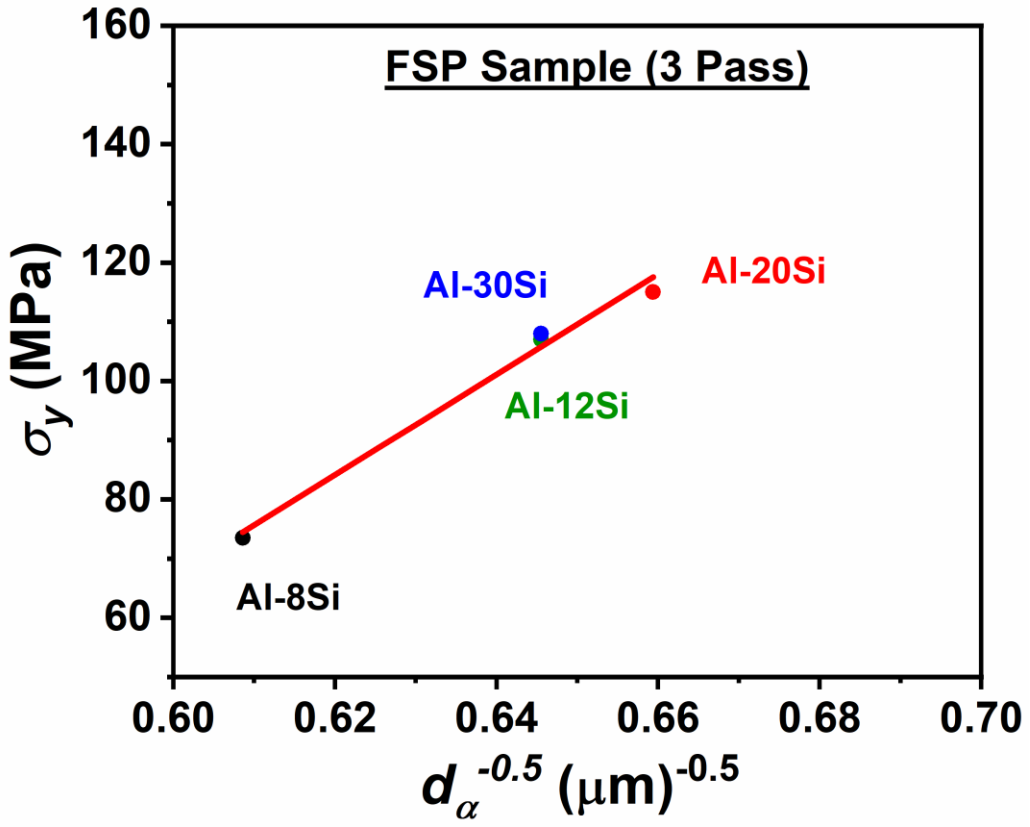
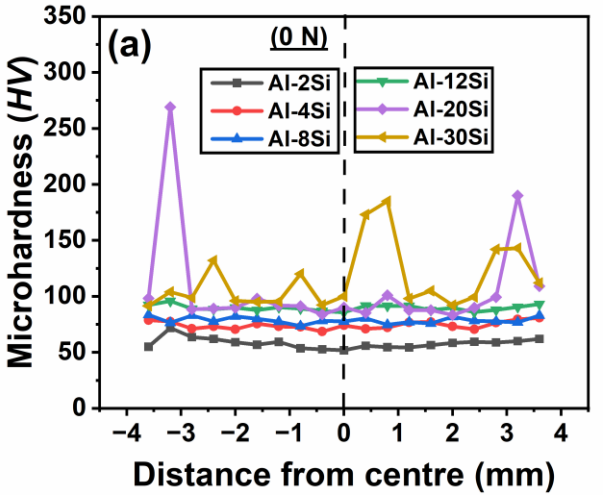
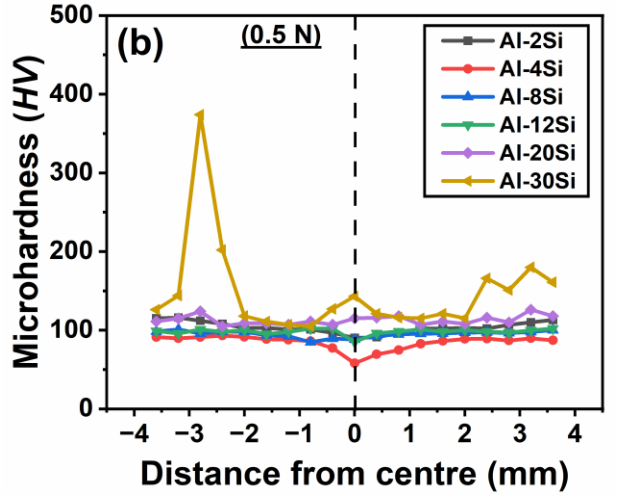


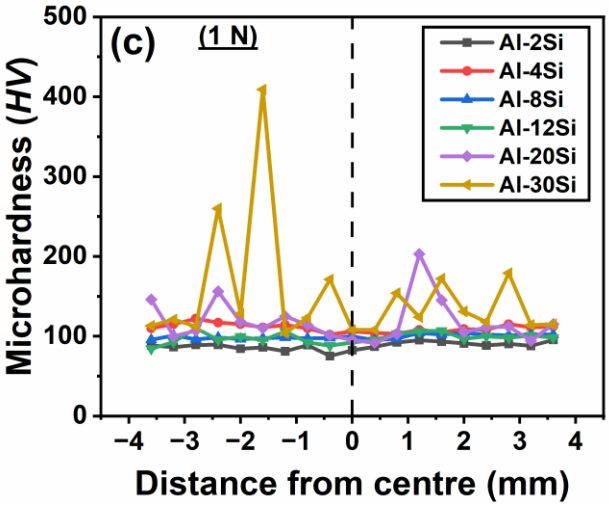
Figure 4.28 : Hall-Petch plot for the grain size obtained from three-pass FSP processed Al-8Si, Al-12Si, Al-20Si, and Al-30Si alloys

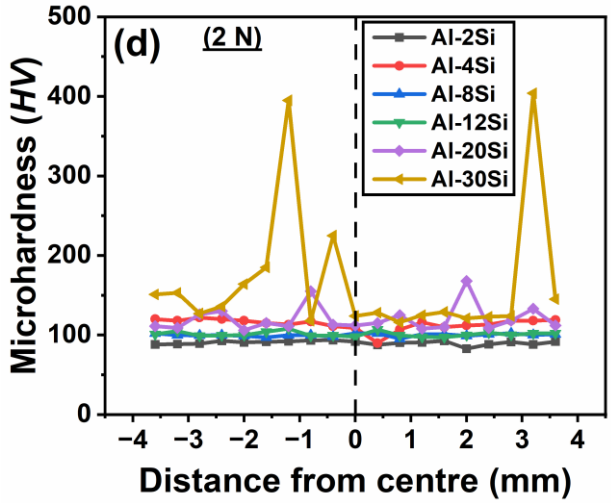
(d) Room Temperature Hardness of HPT Processed Al-Si Alloys

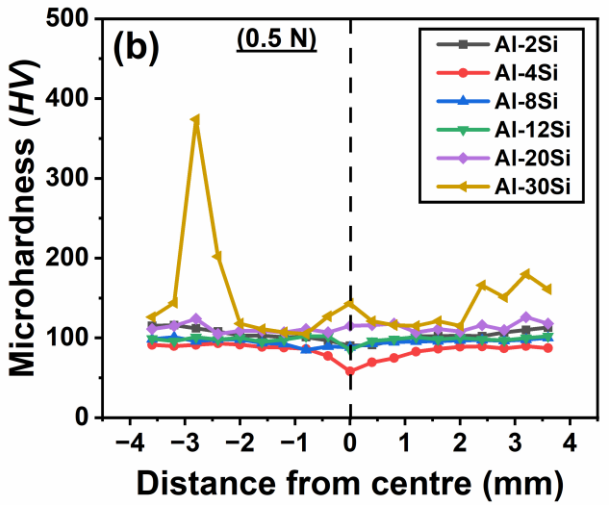
The microhardness of the HPT-processed samples was measured along the sample diameter from one end to the other to evaluate the strengthening of the alloys alongside concurrent microstructural changes. The microhardness values were plotted as a function of sample radius for all HPT turns and all alloy compositions, Figure 4.29(a-h). The magnitudes of hardness for the hypoeutectic Al-Si alloys (Al-2Si, Al-4Si, Al-8Si) were noted to be constant as a function of distance from the centre for all the HPT turns. However, beyond eutectic composition (Al-12Si), the variation was found to be irregular. The hypereutectic Al-Si alloys (Al-20Si, Al-30Si) exhibited more fluctuations in hardness due to the possibility of the random presence of large silicon particles, which might have fallen below the indenter. The minimum hardness values were consistently found at the centre, while the maximum values were consistently near the edge of the sample, irrespective of the alloy composition. Generally, the hardness increases with the increase in distance from the centre towards the edge and with an increase in wt.% Si.

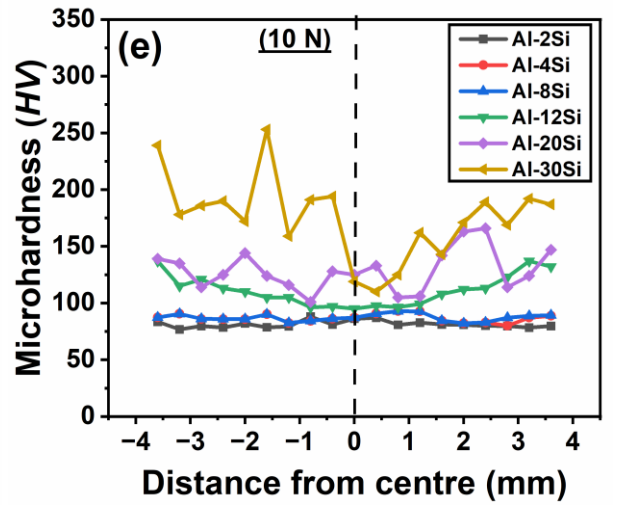

(a)
(0 N)
Al-2Si
Al-4Si
Al-8Si
Al-12Si
Al-20Si
Al-30Si
Microhardness (HV)
Distance from centre (mm)


(b)
(0.5 N)
Al-2Si
Al-4Si
Al-8Si
Al-12Si
Al-20Si
Al-30Si
Microhardness (HV)
Distance from centre (mm)


(c)
(1 N)
Al-2Si
Al-4Si
Al-8Si
Al-12Si
Al-20Si
Al-30Si
Microhardness (HV)
Distance from centre (mm)


(d)
(2 N)
Al-2Si
Al-4Si
Al-8Si
Al-12Si
Al-20Si
Al-30Si
Microhardness (HV)
Distance from centre (mm)


(b)
(0.5 N)
Al-2Si
Al-4Si
Al-8Si
Al-12Si
Al-20Si
Al-30Si
Microhardness (HV)
Distance from centre (mm)


(e)
(10 N)
Al-2Si
Al-4Si
Al-8Si
Al-12Si
Al-20Si
Al-30Si
Microhardness (HV)
Distance from centre (mm)

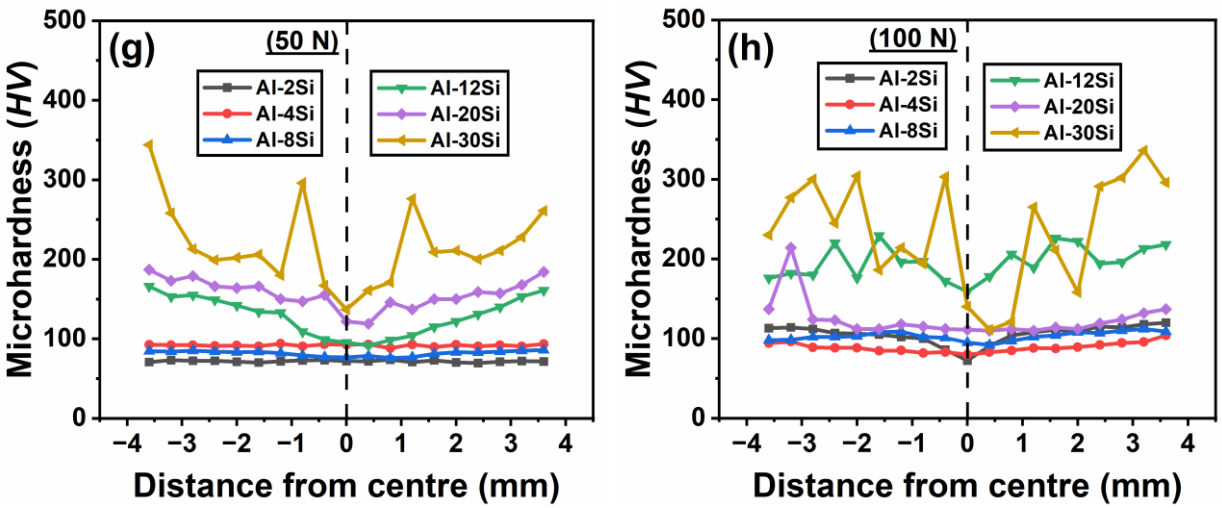


Figure 4.29 : Variation in hardness as a function of sample radius (*r*) and alloy compositions (wt.% Si) for different numbers of HPT turns (*N*); (a) 0*N*, (b) 0.5*N*, (c) 1*N*, (d) 2*N*, (e) 10*N*, (f) 20*N*, (g) 50*N*, and (h) 100*N*

To examine the effects of HPT turns and equivalent strain (sample location), typical hardness values were plotted for a fixed composition (eutectic Al-12Si alloy), shown in Figure 4.30(a), as a function of distance from the centre and number of HPT turns. The initial hardness of the as-cast alloy was relatively lower, measuring 77HV. Notably, the hardness increased immediately after the sample underwent only compression at 6GPa for 1 minute. Subsequently, there was not much effect on the hardness of up to two turns. However, a drastic change occurred for samples subjected to ten, twenty, fifty, and hundred turns, resulting in maximum hardness at the edge, measuring 137HV, 134HV, 166HV, and 195HV, respectively.

Figure 4.30(b) illustrates the variation in hardness with increasing HPT turns for different positions, viz. centre, mid radius, and at the edge of the Al-12Si disc sample. The hardness values exhibited minimal differences among different locations for the low number of HPT turns, but these differences increased as the number of HPT turns (equivalent strain) increased. When examining the hardness variation as a function of equivalent strain (radius), the data for the higher number of HPT turns (N=10, 20, 50, 100) showed an exponential trend without significant scattering, Figure 4.30(d). In contrast, the hardness exhibited irregular variation with equivalent strain for half, one, and two HPT turns, Figure 4.30(c).

The exponential variation of hardness follows the relationship:

$$HV = A_{HS} exp(B_{HS} \varepsilon_{eq}), \tag{4.13}$$

Where HV is the hardness, A_{HS} and B_{HS} are constants, and ε_{eq} represents the equivalent strain.

The effect of grain size on microhardness was analysed to represent the H-P type relationship at different portions of the HPT sample. The grain size variation at a fixed position was obtained by the change in the number of HPT turns, which also resulted in a change in the hardness of the sample. Thus, the hardness variation with $d_a^{-0.5}$ at the centre (0mm), mid-radius (2mm), mid-edge (3mm), and at the edge (4mm) were plotted, as presented in Figure 4.31(a-d). It is revealed that the H-P type relationship is followed with a good correlation coefficient $R^2 \geq 0.78$ at the centre, mid-radius, and edge of the sample, but there is a poor correlation coefficient R^2=0.38 when considered all data points and R^2=0.71 by excluding the encircled data point in the mid-edge portion, Figure 4.31(c). Further, the H-P parameters determined from the above case are plotted as a function of sample radius (equivalent strain), Figure 4.31(e). HV_0 increases with increasing the sample radius or equivalent strain, whereas an opposite trend is

noted for k_{HP}. Also, a mutual plot between these parameters follows a linear relationship (Eq. 4.14), as shown in Figure 4.31(f).

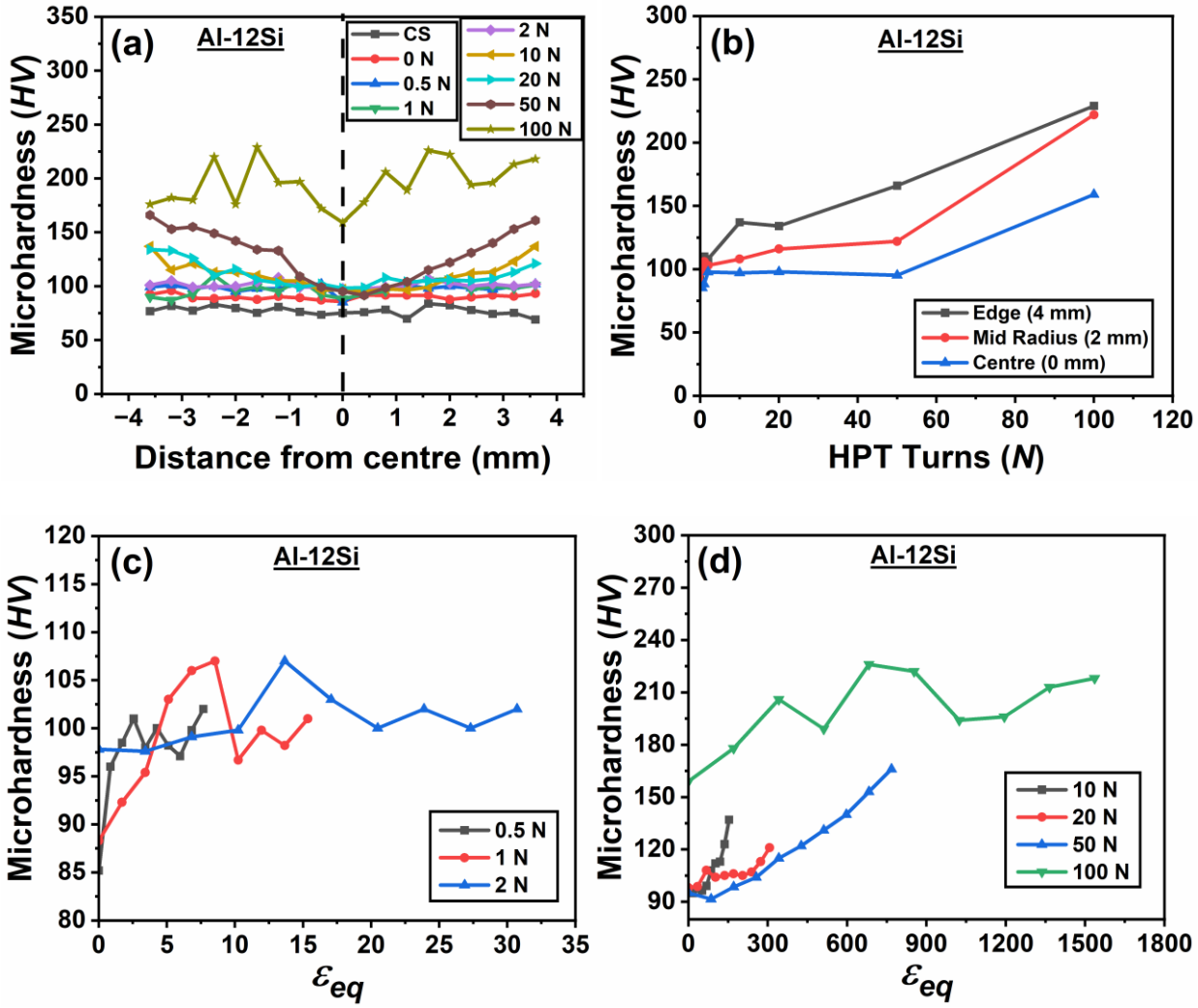
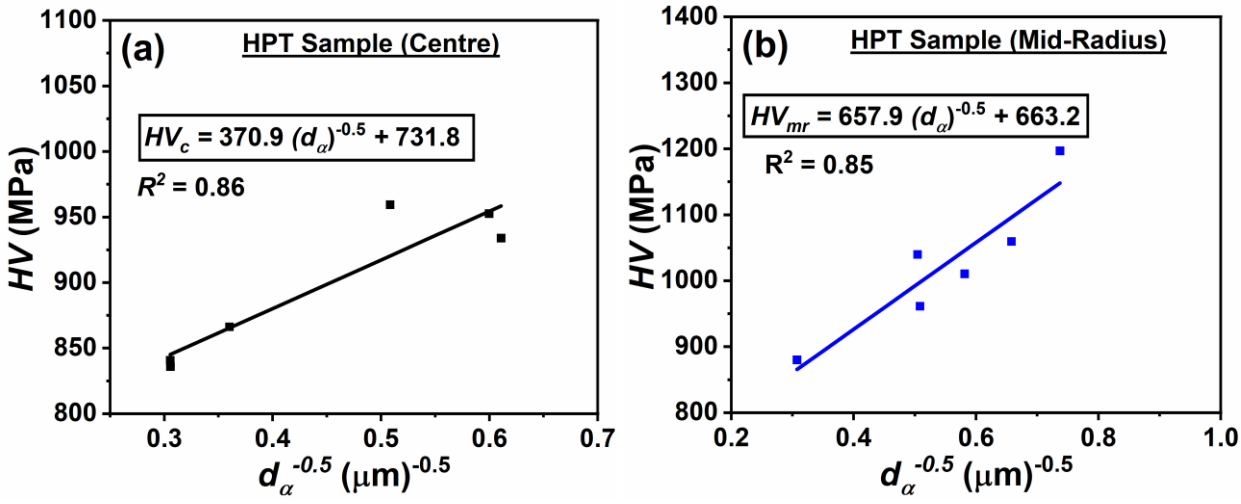


Figure 4.30 : Variation in hardness as a function of the number of HPT turns (~equivalent strain), (b) typical plots for hardness at the centre, mid radius, and the edge of the sample, (c) hardness variation as a function of equivalent strain for half, one, and two HPT turns, (d) hardness variation as a function of equivalent strain for ten, twenty, fifty and hundred HPT turns



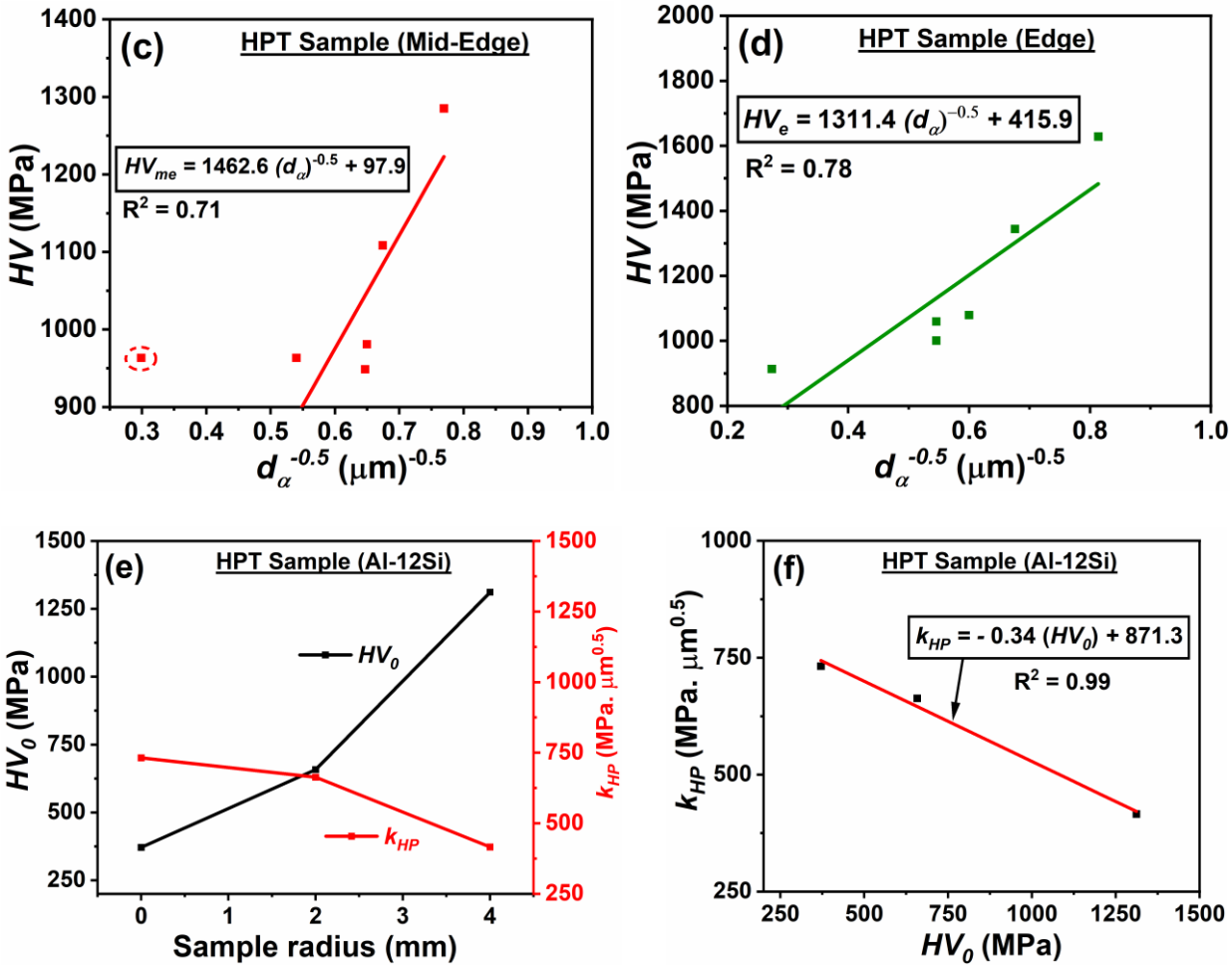


Figure 4.31 : Hall-Petch type plot for Al-12Si alloy processed to 0, 0.5, 1, 2, 10, and 50 HPT turns at (a) centre, (b) mid-radius, (c) mid-edge, and (d) at the edge of the disc type samples, (e) Hall-Petch parameter as a function of sample radius or equivalent strain, (f) interrelationship between HV_0 and k_{HP}

4.2.2 High-Temperature Deformation Behaviour of Al-Si Alloys

The high-temperature tests of all the alloys undergone different processing routes were conducted at constant initial strain rates (CSR), differential strain rates (DSR), and the combinations of the two to observe the flow behaviour and concurrent microstructure evolution during deformation. The obtained mechanical properties and the parameters of the constitutive relationship play a crucial role in understanding the composition-process-structure-property-performance relationship of the designed material for its intended application.

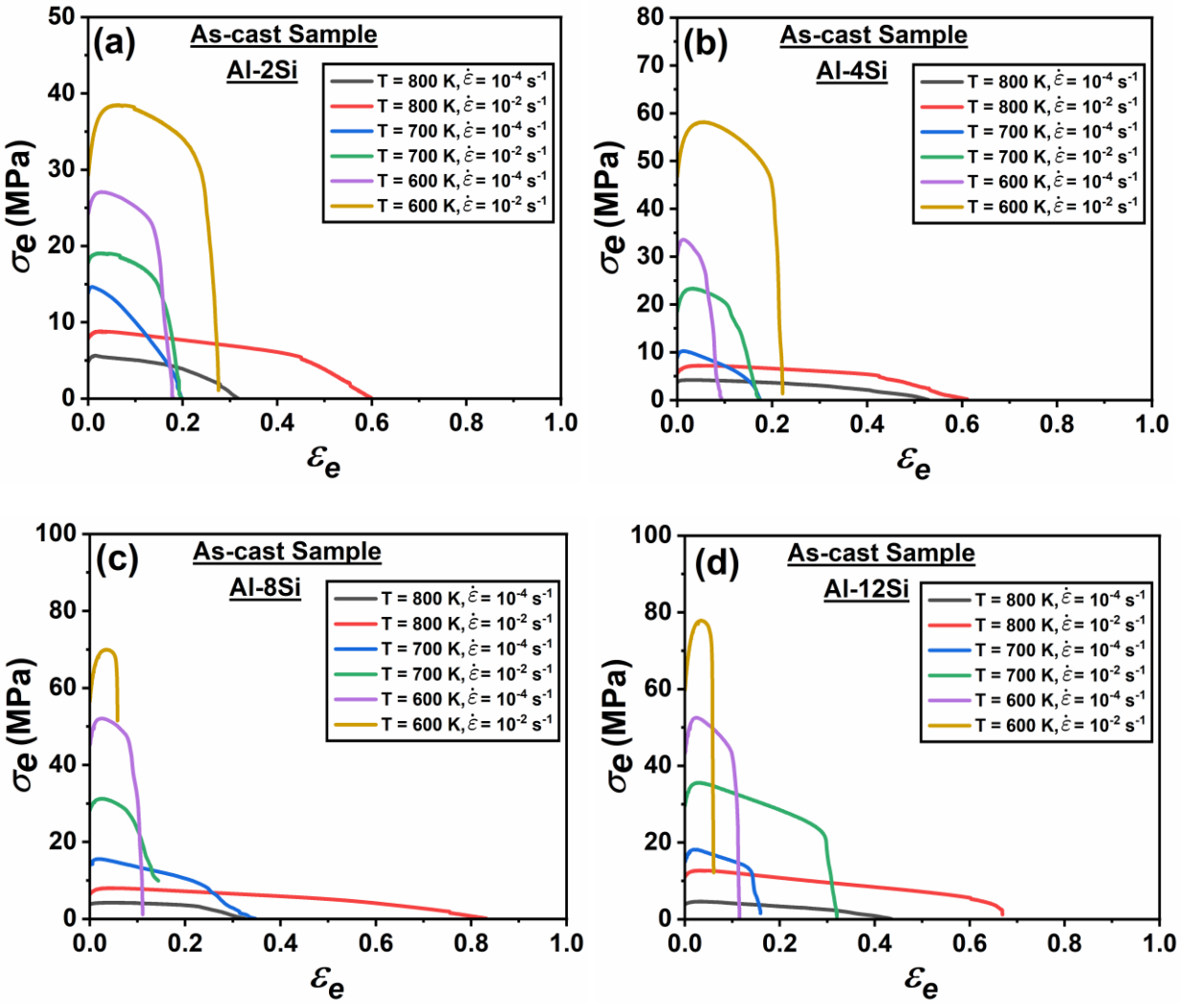
(a) High-Temperature Deformation Behaviour of As-cast Al-Si Alloys

Stress-Strain Curves from CSR Tests

Tensile samples of all six as-cast compositions (as listed in Table 3.1) were subjected to deformation at constant initial strain rates of 10^{-4} and $10^{-2}s^{-1}$ at fixed test temperatures of 600, 700, and 800K. The engineering stress-engineering strain curves in the plastic region of deformation from these tests are presented in Figure 4.32(a-f). Based on the composition and test conditions, the flow stress variation with increasing strain exhibits one or more of the following three stages:

(i) Initially, there is an increase in stress with increasing strain.
(ii) In some cases, stress decreases either from the beginning of deformation or upon reaching the maximum stress point.
(iii) In certain scenarios, there is an accelerated decrease in stress with increasing strain resulting from localized deformation.

The influence of strain, strain rate, test temperature, and alloy composition on the flow behaviour and the nature of stress-strain curves have been summarized and presented in Figure 4.32(g). It is observed that the flow stress increases with increasing silicon content under fixed test conditions. Moreover, for a given alloy composition, the flow stress increases with the increase in strain rate but decreases with the increase in test temperature. The elongation increases with an increase in temperature at the expense of strength and attains a maximum value of more than 80% elongation at the highest test temperature and higher strain rate for hypoeutectic Al-8Si alloy. Elongation decreases as the silicon content increases in the alloys and attains the minimum value of 1% for hypereutectic Al-30Si alloy. Work hardening is evident under certain conditions, and its magnitude (strain hardening rate, θ_H) increases with higher strain rates and lower test temperatures. Also, the presence of work hardening is more pronounced in alloys with higher silicon content. Additionally, for the selected test temperatures and strain rates, the effect of temperature on θ_H is found to be more significant compared to the influence of strain rate. This suggests that temperature plays a dominant role in affecting the work-hardening behaviour of the materials under consideration.



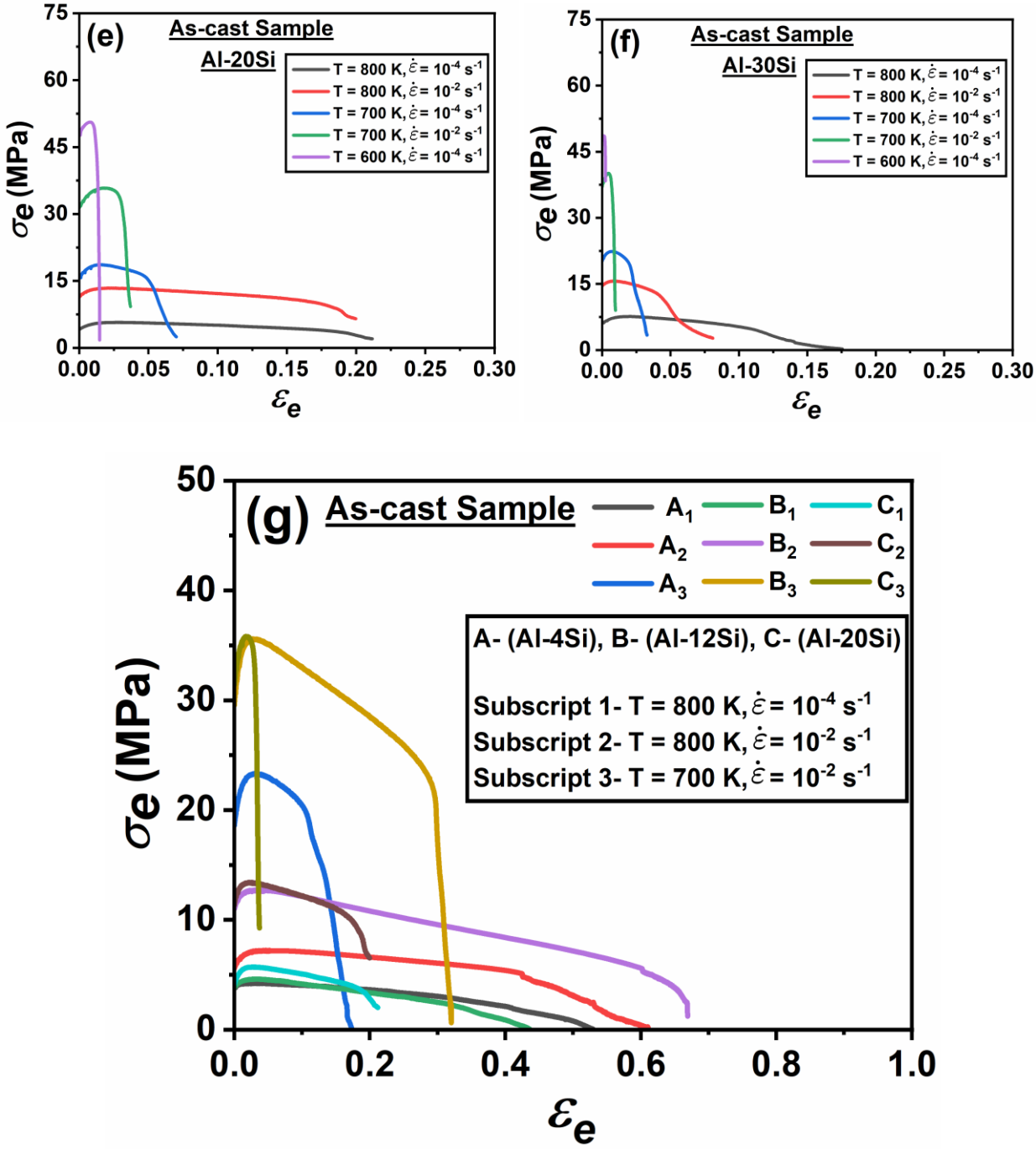


Figure 4.32 : Stress-strain curves obtained from tension tests at different test conditions (T, $\dot{\varepsilon}$) as shown by legends in the figures for as-cast hypoeutectic (2 wt.% Si, 4 wt.% Si, 8wt.% Si) Al-Si alloys (a-c), (d) eutectic Al-12Si alloy, and (e-f) hypereutectic (Al-20Si, Al-30Si) alloys, and (g) a summary of typical stress-strain curves for different alloy compositions and varying test conditions

The secant work hardening rates (θ_H), defined by $\theta_H = \frac{(\sigma_p - \sigma_0)}{\varepsilon_p}$, were determined from the values of peak stress (σ_p), stress at the onset of plastic strain (σ_0), and strain (ε_p) corresponding to the peak stress. The values of ε_p, (σ_p - σ_0), θ_H were plotted as a function of Si content (C_{Si}) for different strain rates and test temperature conditions, Figure 4.33(a-c). Shown here in Figure 4.33(c) is the variation in θ_H as a function of Si content in the Al-Si alloys for different strain rates and temperature conditions. It is noted that θ_H generally increases with increasing Si content, and the nature of observed variation is sensitive to the test temperature and strain rate conditions. The variation in θ_H is more predominant at the lower temperature and higher strain rate conditions. For the selected test temperatures and strain rates, the effect

of temperature on θ_H appears to be greater than that of strain rate. The plots of ε_p and $(\sigma_p - \sigma_0)$ as a function of Si content, Figure 4.33(a,b), both were generally found to follow the opposite trend of that seen in the variation of θ_H. The nature of the increase in work hardening rate (θ_H) as a function of C_{Si} can be quantitatively expressed by a linear relationship as follows.

$$\theta_H = A_H C_{Si} + B_H, \tag{4.15}$$

Here, A_H is the slope of a straight line, whereas B_H is the intercept. The values of A_H decrease with increasing temperature but increase with increasing strain rate, Figure 4.33(d). The values of B_H decrease with increasing temperature and strain rate.

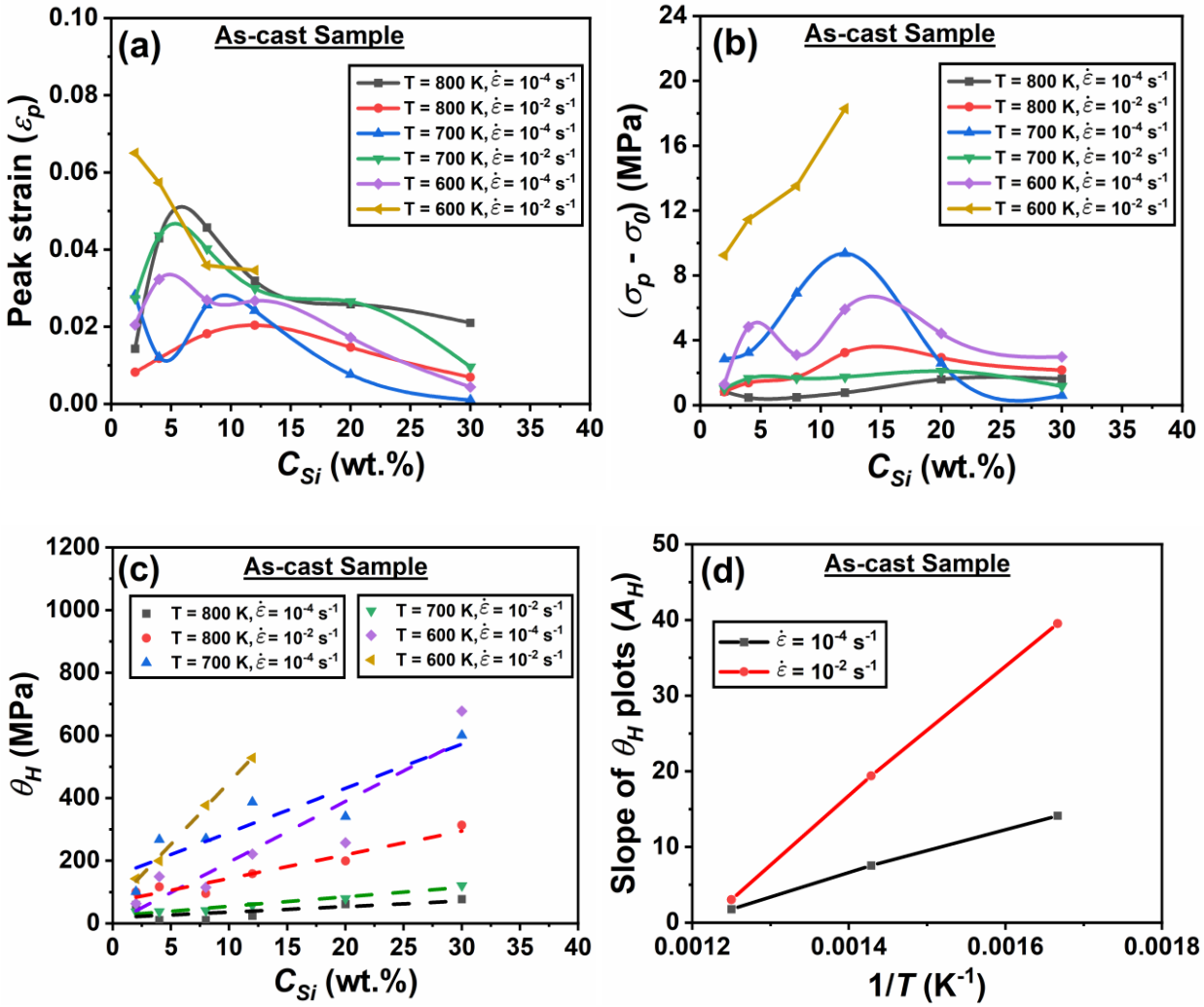


Figure 4.33 : Peak strain (ε_p) plot as a function of silicon content from different test conditions (a), $(\sigma_p - \sigma_o)$ plot as a function of silicon content (b); (c) work hardening rate (ϑ_H) plot from the tensile test data as a function of silicon content, and (d) the variation in slope value as a function of inverse temperature from the curve fitting of work hardening plot in (c) as a function of test condition

The nature of the flow softening part of the stress-strain curves as a function of C_{Si} at different temperatures and strain rates used in this work was also examined. The variation in strain span for softening (ε_s=strain corresponding to the end of softening, ε_{ES}–strain corresponding to the peak stress from where softening starts, ε_p) and the difference between the peak stress (σ_p) and the stress (σ_{ES}) at the end of the flow softening part (σ_s=σ_p–σ_{ES}) of the stress-strain curves are presented as a function of Si content (C_{Si}) in Figure 4.34(a) and Figure 4.34(b), respectively. The variations in ε_s and σ_s as a function of C_{Si} appear as a scatter at first glance, but a careful examination of the plot reveals maximum effects in these parameters of strain

softening at the intermediate level of Si content around the eutectic composition. Similarly, the effects of test temperature and strain rate on ε_s and σ_s can be vividly drawn as presented below.

Shown in Figure 4.34(c) is the plot of flow softening rate θ_S (-ve to work hardening rate) as a function of C_{Si}. This also shows the same type of variation as that for the work hardening rate with increasing Si. The nature of the increase in θ_S as a function of C_{Si} can be quantitatively expressed by a linear relationship between the two as follows.

$$\theta_s = A_s C_{Si} + B_s, \tag{4.16}$$

Here, A_S is the slope of the trend lines in Figure 4.34(c), whereas B_S is the intercept. As shown in Figure 4.34(d), the value of A_S decreases with increasing temperature but increases with increasing strain rate. The values of B_S (not shown in Figure) decreased with increasing temperature and strain rate.

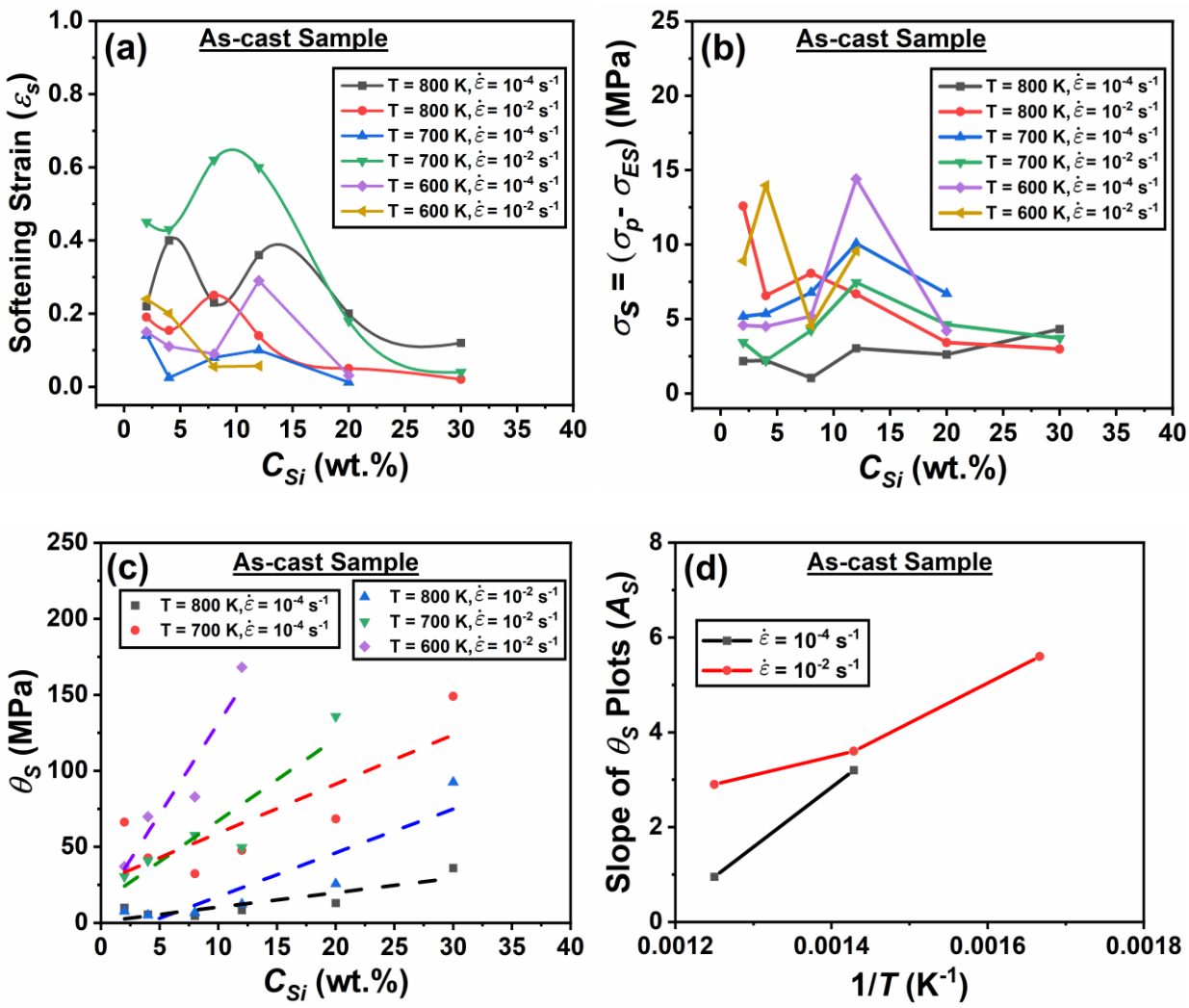


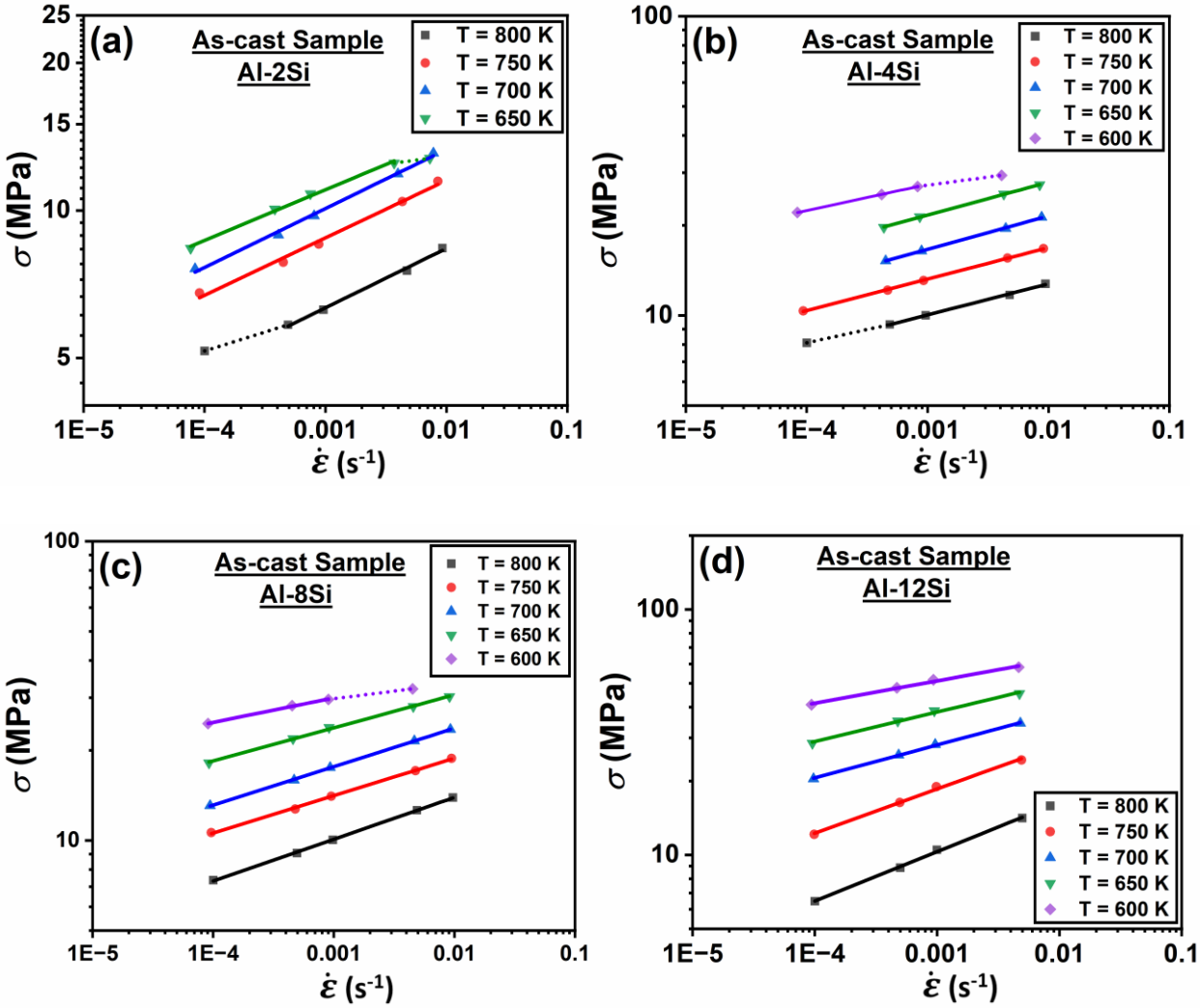
Figure 4.34 : Flow softening strain value (ε_S) plot as a function of silicon content at different test conditions (a), (σ_S=σ_p–σ_{ES}) plot as a function of silicon content, (c) work softening (ϑ_S) plot as a function of Si content, and (d) the variation in slope value of the curve fitting in work softening plot (Figure c) as a function of test conditions

Stress-Strain Rate Behaviour of the As-Cast Alloy

CSR and DSR type tests were employed to collect the data for stress (σ) - strain rate ($\dot{\varepsilon}$) plots. The strain rate sensitivity index (m) and activation energy (Q) were obtained from the limited data of two strain rates and three test temperatures employed in the CSR tests, which could, therefore, give the approximate values of these parameters. In order to get the more definite values of m and Q, σ-$\dot{\varepsilon}$ data were collected over the strain rate range of ~ 10^{-4}-$10^{-2}$$s^{-1}$ and

at the decreasing test temperature ranges of (i) 800-600K and (ii) 840-800K, using the separate samples for each temperature ranges in DSR technique.

Case (i): Presented in Figure 4.35(a-f) are the σ-$\dot{\varepsilon}$ plots determined over the strain rate range of 10^{-4} to $10^{-2}s^{-1}$ and the temperature range from 800 to 600K, at an interval of 50K, for all the alloy compositions and the whole temperature range investigated. σ-$\dot{\varepsilon}$ plots in Figure 4.35(a-f) show an increase in flow stress with the increase in strain rate and decrease in test temperature. In most cases, the σ-$\dot{\varepsilon}$ plots are seen to exhibit straight lines with a constant slope, which, as per Eq.(3.12), reveals constant values of m, being independent of strain rate and test temperature. However, in a few cases, the magnitude of m is noted to be reduced. The magnitude of m was obtained to vary from 0.08 to 0.2, with the highest value of m=0.2 being for the eutectic Al-12Si alloy at the highest test temperature of 800K and the lowest value of m=0.08 being for Al-30Si alloy at the lowest common test temperature of 650K.



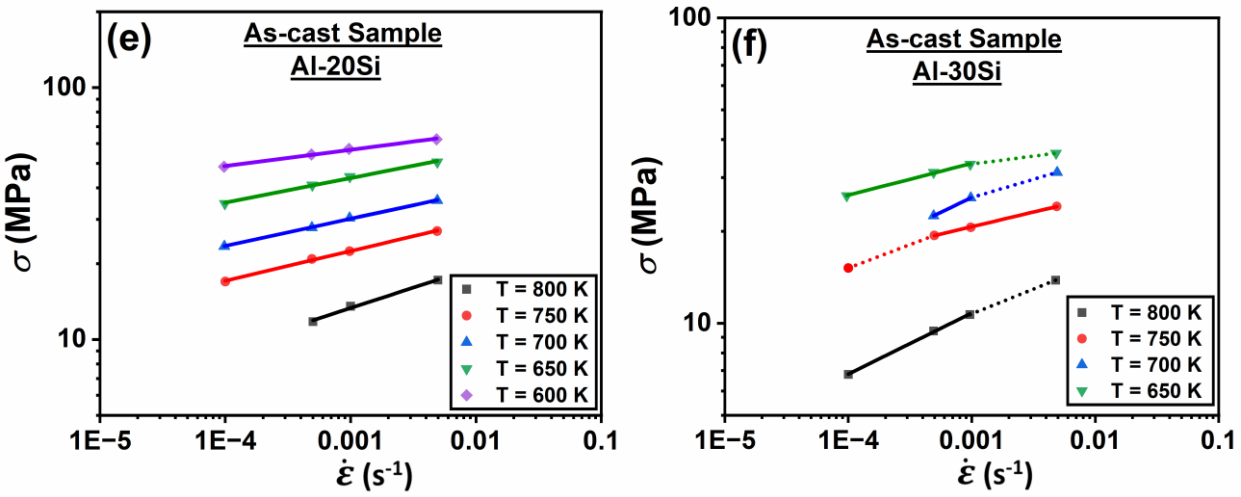
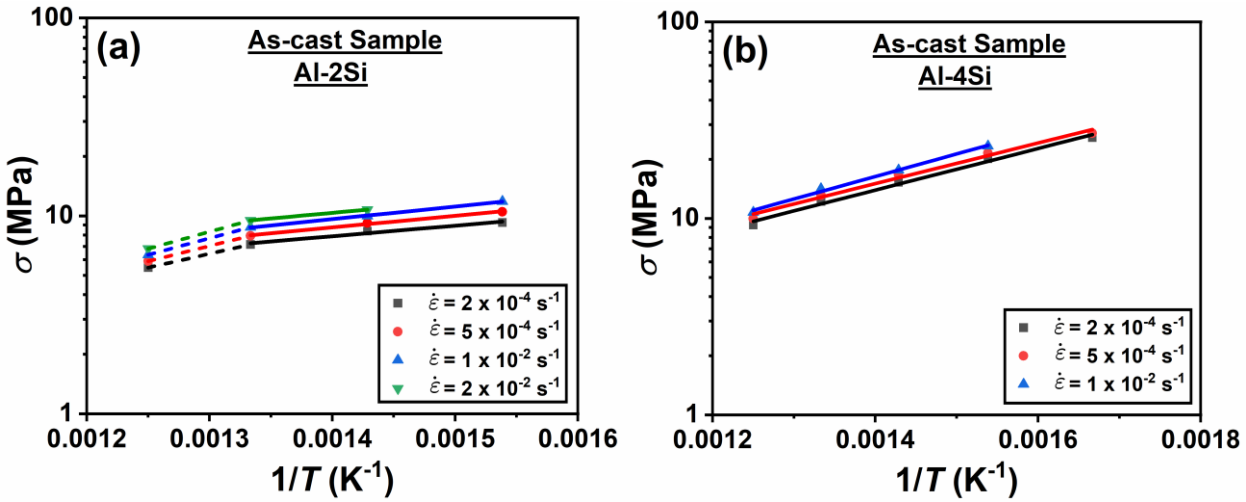


Figure 4.35 : Stress-strain rate plot obtained from DSR type tests for as-cast (a-c) hypoeutectic ((a) Al-2Si, (b) Al-4Si, (c) Al-8Si), (d) eutectic Al-12Si, and (e-f) hypereutectic (Al-20Si and Al-30Si respectively) alloys

The values of apparent activation energy (Q_a) for high-temperature deformation were determined at constant strain rates by using Eq.(3.13) and taking the average value of n (inverse of m) at the temperatures involved in the Arrhenius plots given in Figure 4.36(a-g). The Arrhenius plot shows two slopes with bi-linear behaviour, suggesting higher values of activation energy at higher temperatures and lower Q_a at lower test temperatures. The activation energy for deformation in the lower temperature range varied from 109.6±0.9kJ/mol in the hypoeutectic Al-2Si alloy to 148±1.9kJ/mol in the hypereutectic Al-30Si alloy. The Q_a for these alloys in higher temperature ranges was found to vary from 287.3kJ/mol to 499kJ/mol, Figure 4.36(g) (no error was calculated because of 2 data points only).



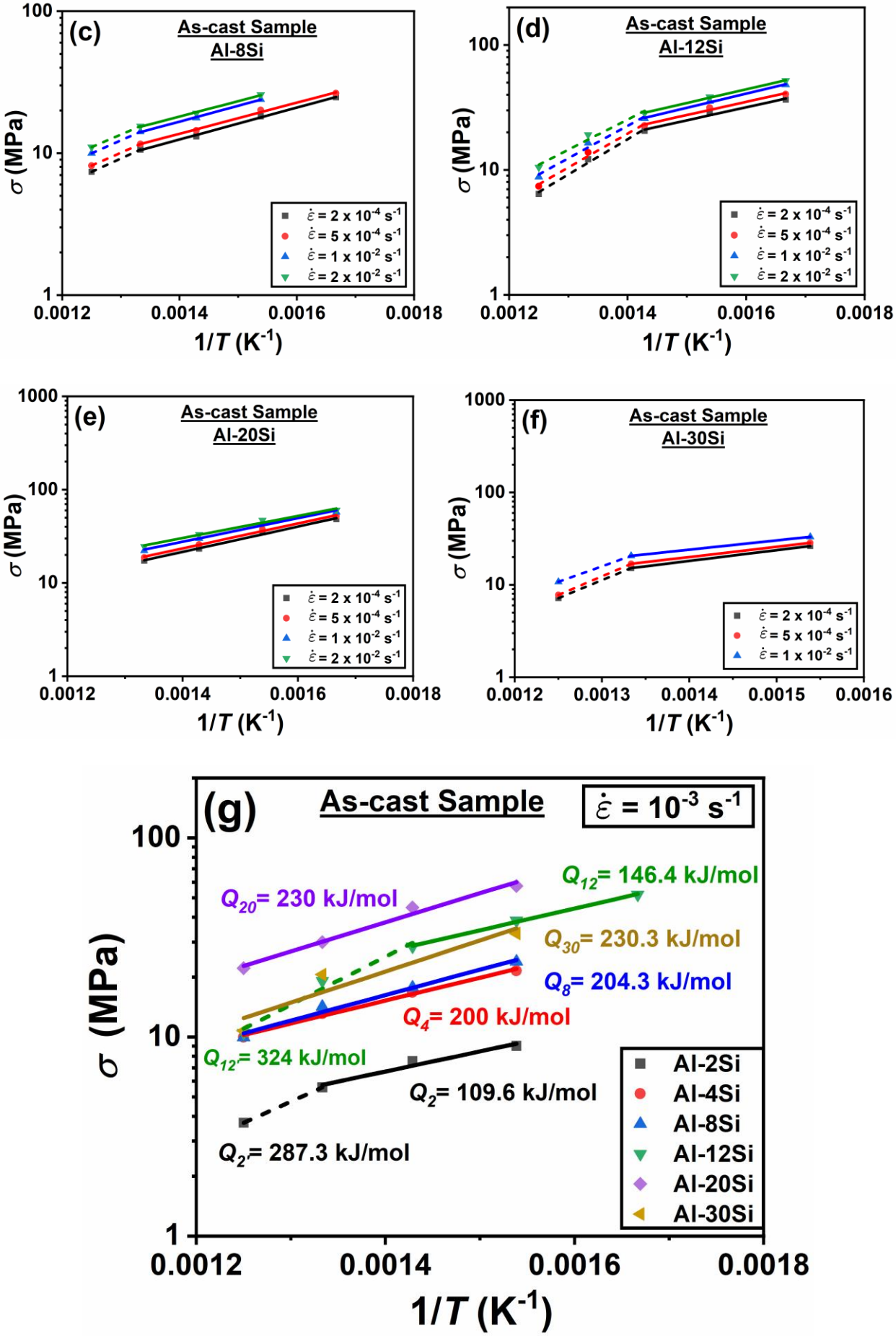
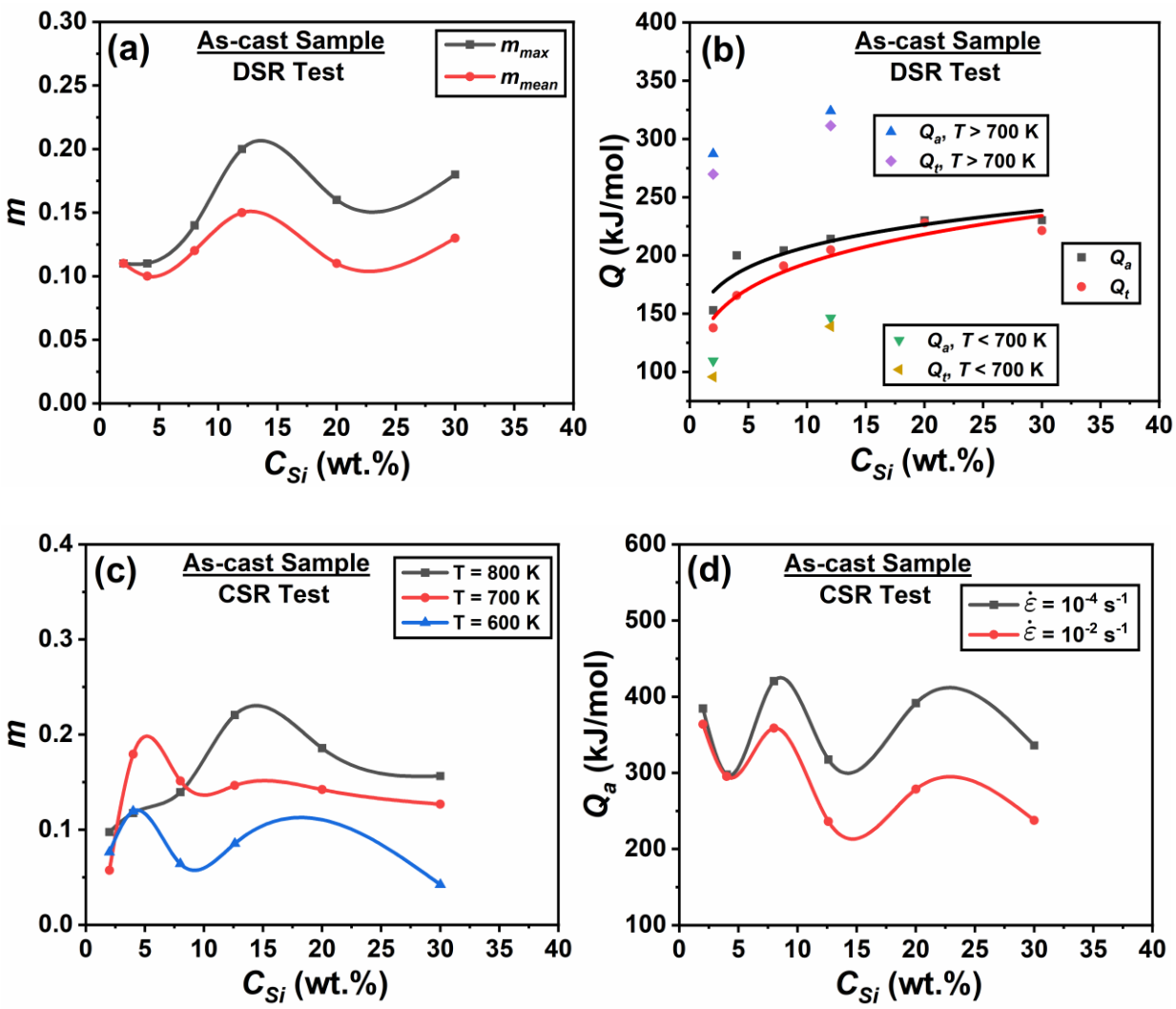


Figure 4.36 : Arrhenius type plot taken at different strain rates for (a) Al-2Si, (b) Al-4Si, (c) Al-8Si, (d) Al-12Si, (e) Al-20 Si, (f) Al-30Si as-cast alloys, and (g) summary of typical Arrhenius plots for all the alloy compositions

The plot of m and Q_a, calculated from DSR tests data for deformation as a function of C_{Si}, as presented in Figure 4.37(a,b), exhibits an increase in the magnitude of m up to eutectic composition and then a decrease for the higher silicon alloy. The value of Q_a increases with increasing C_{Si}, but it is noted to get saturation for hypereutectic alloys C_{Si}=20 to 30. Also, the true activation energy (Q_t) (method described in Chapter 3) was calculated by taking the effect of E as a function of temperature, Eq.(3.14), which showed a slightly lower value compared to Q_a, and followed the same trend as a function of silicon content.

An attempt was made to determine the values of m and Q_a from the stress-strain curves of the CSR tests at limited temperatures and strain rates. In this case, also, m varied from 0.04 for the hypereutectic Al-30Si at the lowest test temperature of 600K to 0.22 for the eutectic Al-12Si alloy at the highest test temperature of 800K. This effect of Si on m is similar to that from the DSR tests, Figure 4.37(c). The values of Q_a obtained from the CSR tests were found to vary in the range ~276.9 to 389.5kJ/mol in an irregular way as a function of C_{Si}, but the overall trend in Q_a, within the scatter, seemed to decrease with increasing silicon content and increase in strain rate, Figure 4.37(d). Figure 4.37(e) shows the plot of Q_t vs. Q_a, which exhibits that both the activation energies are comparable as a function of the alloy compositions.



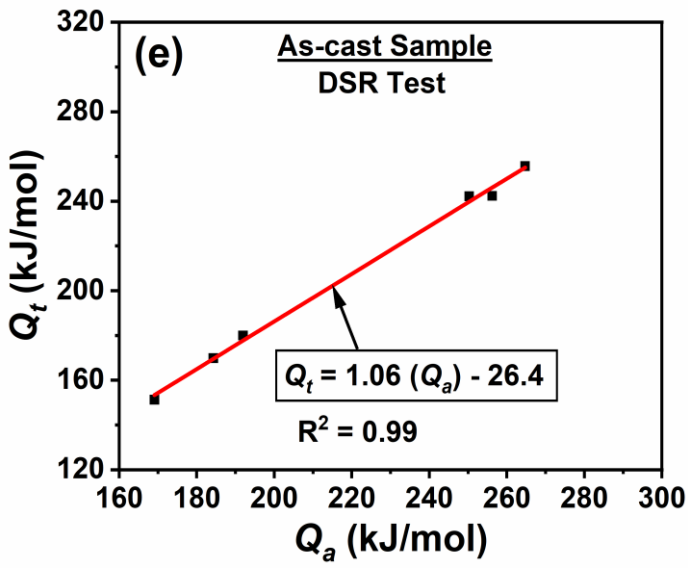


Figure 4.37 : Parameters of constitutive relationship for deformation of as-cast Al-Si alloys, calculated from DSR tests and plotted: (a) *m* as a function of silicon content, and (b) apparent (Q_a) and true activation energies (Q_t) as a function of silicon content; the parameters of constitutive relationship, calculated from CSR tests are plotted in (c) *m* as a function of silicon content for different test temperatures, and (d) *Q* plotted as a function of silicon content. Replotted in Figure (e) is a comparison of true vs. apparent activation energies from Figure (b,d) as a function of increasing Si content

Case (ii): Coupled DSR and CSR tests were performed on tensile samples representative of eutectic (Al-12Si) and hypereutectic (Al-30Si) compositions. The DSR tests were performed at temperatures of 840, 820, and 800K sequentially, as described earlier, over the same range of strain rates. Upon completion of DSR tests at the lowest test temperature of 800K, the tensile test was stopped, and the test temperature was raised to the starting highest temperature of 840K, at which the sample was deformed to failure at the constant initial strain rate of $10^{-4}s^{-1}$. Figure 4.38(a-c) shows the stress-strain curves obtained from DSR tests over the temperature range of 840-800K and from the CSR test at 840K. The stress-strain curve for eutectic composition shows flow hardening initially, but flow softening is noted to dominate over the large range of strain. In the hypereutectic alloy, the stress-strain curve shows rapid flow softening. Total elongations combining the elongation during DSR tests and CSR tests were found to be 57.8% and 15% for eutectic and hypereutectic Al-30Si alloy compositions, respectively. σ-$\dot{\varepsilon}$ plot for Al-12Si and Al-30Si, in the higher temperature range of 840-800K, presented in Figure 4.38(d,e), and Figure 4.38(f) represent the Arrhenius plot for determining true activation energy for deformation of Al-12Si and Al-30Si alloys. The values of *m* were determined to be 0.19-0.28 and 0.17-0.25 for the eutectic Al-12Si and hypereutectic Al-30Si alloys. Similarly, the activation energies were determined to be 196.5±98.4kJ/mol and 149.5±63.6kJ/mol, respectively.

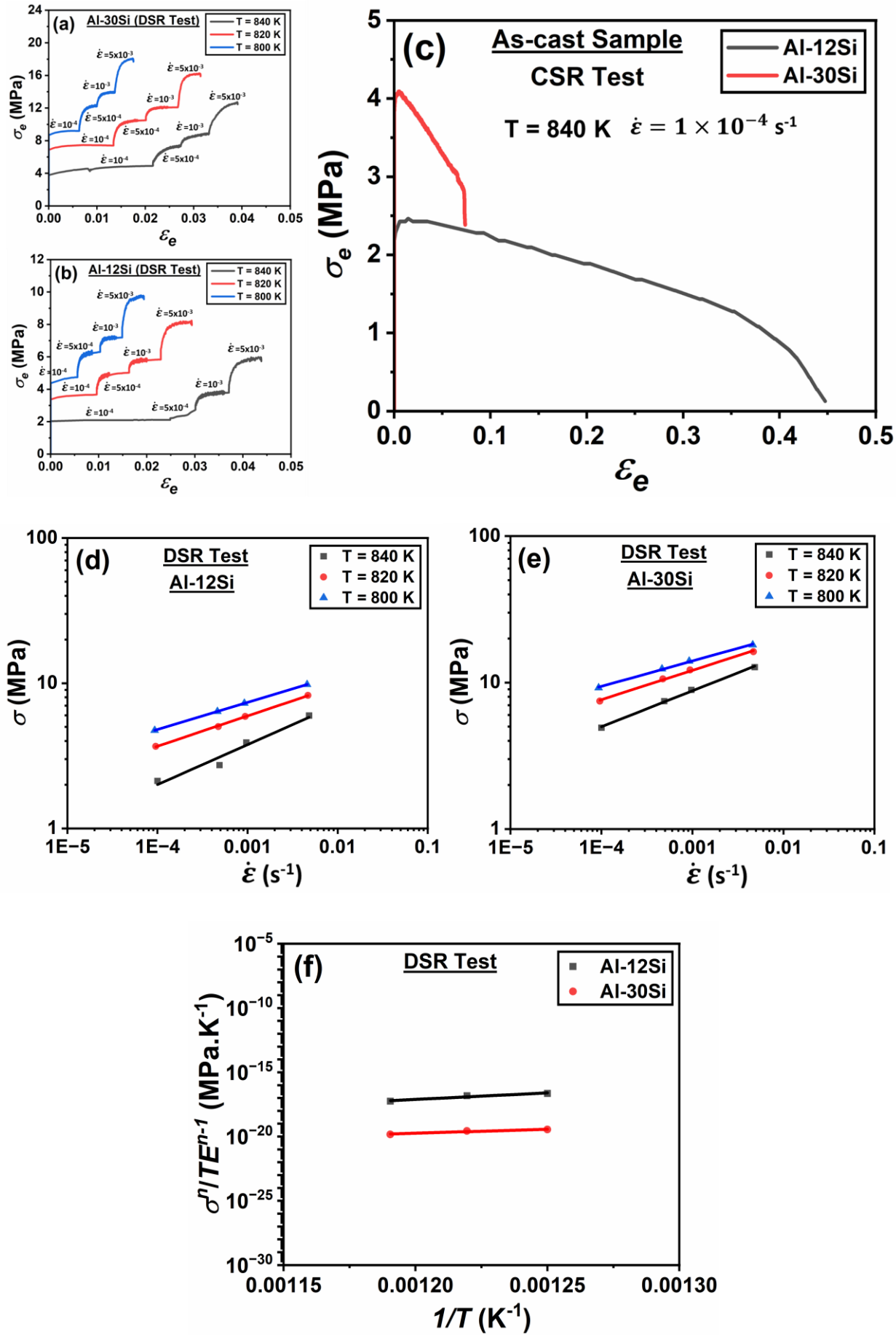


Figure 4.38 : (a-c) Stress-strain curves obtained from the coupled differential strain rate test followed by constant initial strain rate tests for the as-cast Al-12Si eutectic and Al-30Si hypereutectic alloys; differential strain rate test for (a) Al-30Si, (b) Al-12Si alloys, and (c) stress-strain curves from CSR tests after differential

strain rate tests; stress-strain rate plot in the higher temperature range of 800-840K for (d) Al-12Si, and (e) Al-30Si alloys; (f) Arrhenius plot for determining true activation energy for deformation of Al-12Si and Al-30Si alloys

Microstructure Evolution During Deformation

Tensile samples deformed to fracture, whose stress-strain curves are summarized in Figure 4.32(g), were examined for the microstructure evolved from the fracture region to away along the gage length. The microstructures that evolved owing to deformation are summarized in Figure 4.39. There appears to be a pseudo-brittle fracture, along with the presence of large voids. The large primary Si particles present in the beginning are found to remain unchanged in size and shape. However, the Al matrix grains and the eutectic phase reveal significant changes during deformation. The observed comparison between the initial microstructures and those that evolved upon deformation is qualitatively described in Table 4.6.

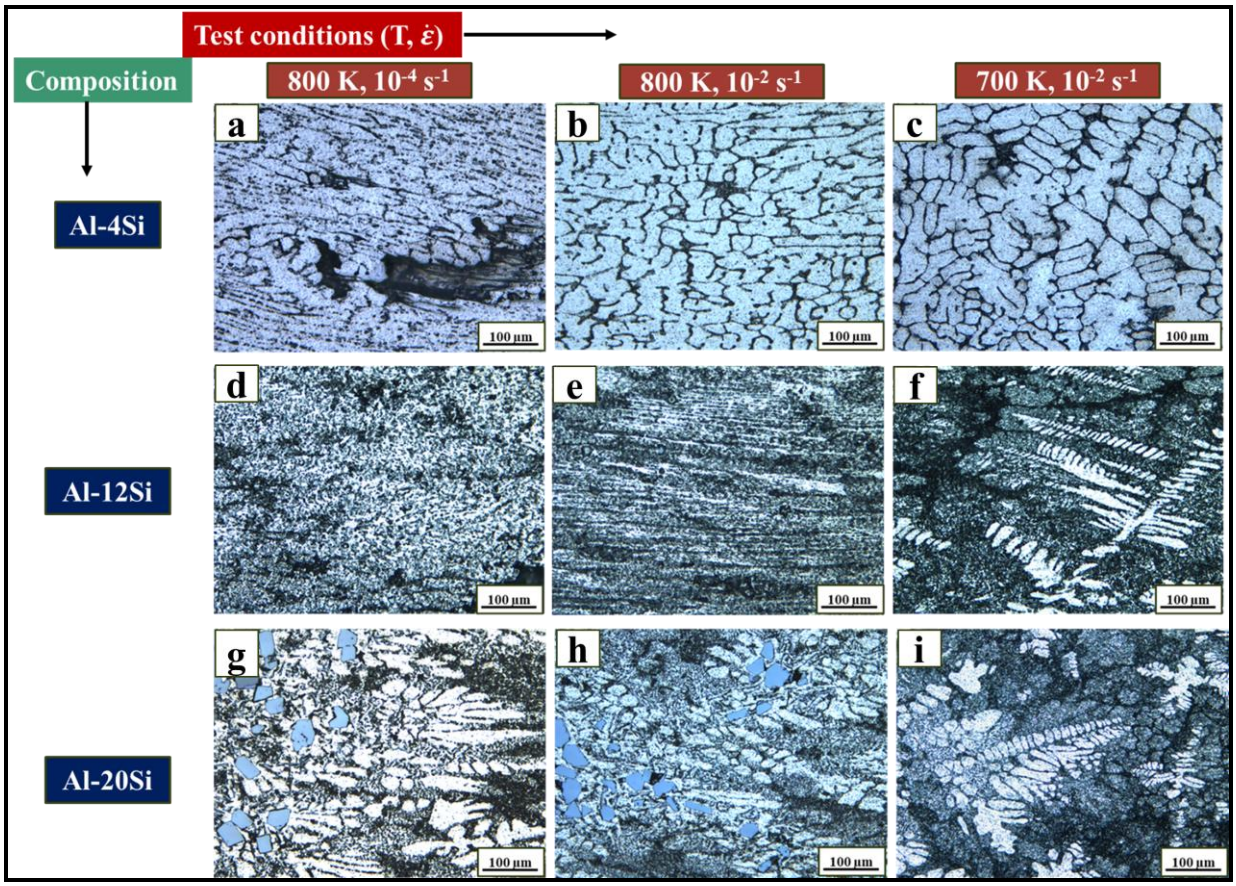


Figure 4.39 : Typical summary of microstructures evolved upon high-temperature deformation corresponding to the test conditions and ε_f values as notable in Figure 4.32(g)

Table 4.6 : A comparative summary of evolved microstructure and change in mechanical properties of post-deformed samples

Alloy Composition	*Initial condition*	*After Deformation*		
		T=800K, $\dot{\varepsilon}=10^{-4}s^{-1}$	*T=800K, $\dot{\varepsilon}=10^{-2}s^{-1}$*	*T=700K, $\dot{\varepsilon}=10^{-2}s^{-1}$*
Al-4Si	No P-Si Fine *EP* Coarse d_α No large voids present *HV*=39HV	No P-Si ↑ *EP* Elongated d_α ↑ ↑ d_{cv} ↑ NA Ductile fracture HV_d=16.6-38.2HV, 33.4HV	No P-Si ↑ *EP* ↑ d_α ↓ d_{cv} ↑ NA Semi-Ductile HV_d=16.6-40.6HV, 33.5HV	No P-Si ↑ *EP* ↑ As-cast d_α ↓ d_{cv} ↓ NA Semi-ductile HV_d=42.8-45.1HV, 43.5HV
Al-12Si	Small P-Si Fine *EP* Randomly-orientated dendritic d_α No voids present *HV*=77HV	↓ d_{Si} Refined *EP* ↓ d_α More cavity (↑ d_{cv}) ↑ NA Ductile fracture HV_d=38-52.2HV	↓ d_{Si} Refined *EP* Elongated d_α Less cavity (↓ d_{cv}) ↑ NA Pseudo-ductile HV_d=36.9-53.2HV, 45.7HV	↓ d_{Si} No change in *EP* No change in d_α No cavity (d_{cv}) ↓ NA Pseudo-ductile HV_d=53.2-67.3HV, 61.9HV
Al-20Si	Large P-Si Fine *EP* Mostly globular d_α No voids present *HV*=91HV	↓ d_{Si} Refined *EP* ↑ Elongated d_α Less cavity (d_{cv}) ↓ NA Pseudo-brittle type HV_d=56-127HV, 76.7HV	No change in d_{Si} ↓ *EP* ↑ Elongated d_α Less cavity (↑ d_{cv}) ↓ NA Pseudo-brittle type HV_d=22-101HV, 60.2 HV	↓ d_{Si} ↓ *EP* As-cast d_α No cavity (d_{cv}) ↓ NA Brittle fracture HV_d=78-54HV, 66HV

Post-Deformation Hardness at Room Temperature

Also, the study aimed to comprehend the influence of high-temperature deformation behaviour on room-temperature properties by examining the hardness of the gage section of the samples deformed to fracture under various test conditions. In Figure 4.40(a), microhardness variations are depicted as a function of the silicon content of both initial and deformed samples across typical test conditions. Notably, the microhardness of deformed samples is registered to be lower than that of the initial samples. Furthermore, the microhardness of the deformed samples exhibits an increasing trend as a function of silicon content, similar to the behaviour

observed in the initial samples. After careful observation, it can be noted that the microhardness generally diminishes as the test temperature rises. In the case of hypoeutectic Al-4Si and eutectic Al-12Si alloys, the maximum hardness is achieved at a lower deformation temperature of 700K and a higher strain rate of $10^{-2}s^{-1}$. Contrarily, for Al-20Si, the peak hardness of approximately 80HV is achieved under the opposite conditions, with the highest deformation temperature of 800K and the lowest strain rate of $10^{-4}s^{-1}$. The nature of variation in hardness reveals the softening effect to varying degrees, as caused by high-temperature deformation and test conditions. In spite of varying Si content and variation in high-temperature test conditions, the Hall-Petch type relationship was found to be obeyed reasonably well for both the undeformed and deformed samples separately and together, as well, Figure 4.40(b).

$$HV = 372.9(d_\alpha)^{-0.5} - 12.6, \qquad R^2 = 0.75 \qquad (4.17)$$

Similarly, it was examined whether the hardness measured at room temperature has any relationship with the elongation of the samples deformed at high temperatures. Interestingly, here also, the decrease in hardness at room temperature, but upon deformation at high temperature, acts as a token of elongation that the sample had undergone at high temperature, Figure 4.40(c). The activation energy values for high-temperature deformation of hypoeutectic (Al-4Si), eutectic (Al-12Si), and hypereutectic (Al-20Si) alloys are plotted as a function of room temperature hardness values of the respective samples in Figure 4.40(d). This plot, with a good level of certainty, exhibits a linear relationship of type.

$$HV_d = 2.3(Q_d) + 210, \qquad R^2 = 0.99 \qquad (4.18)$$

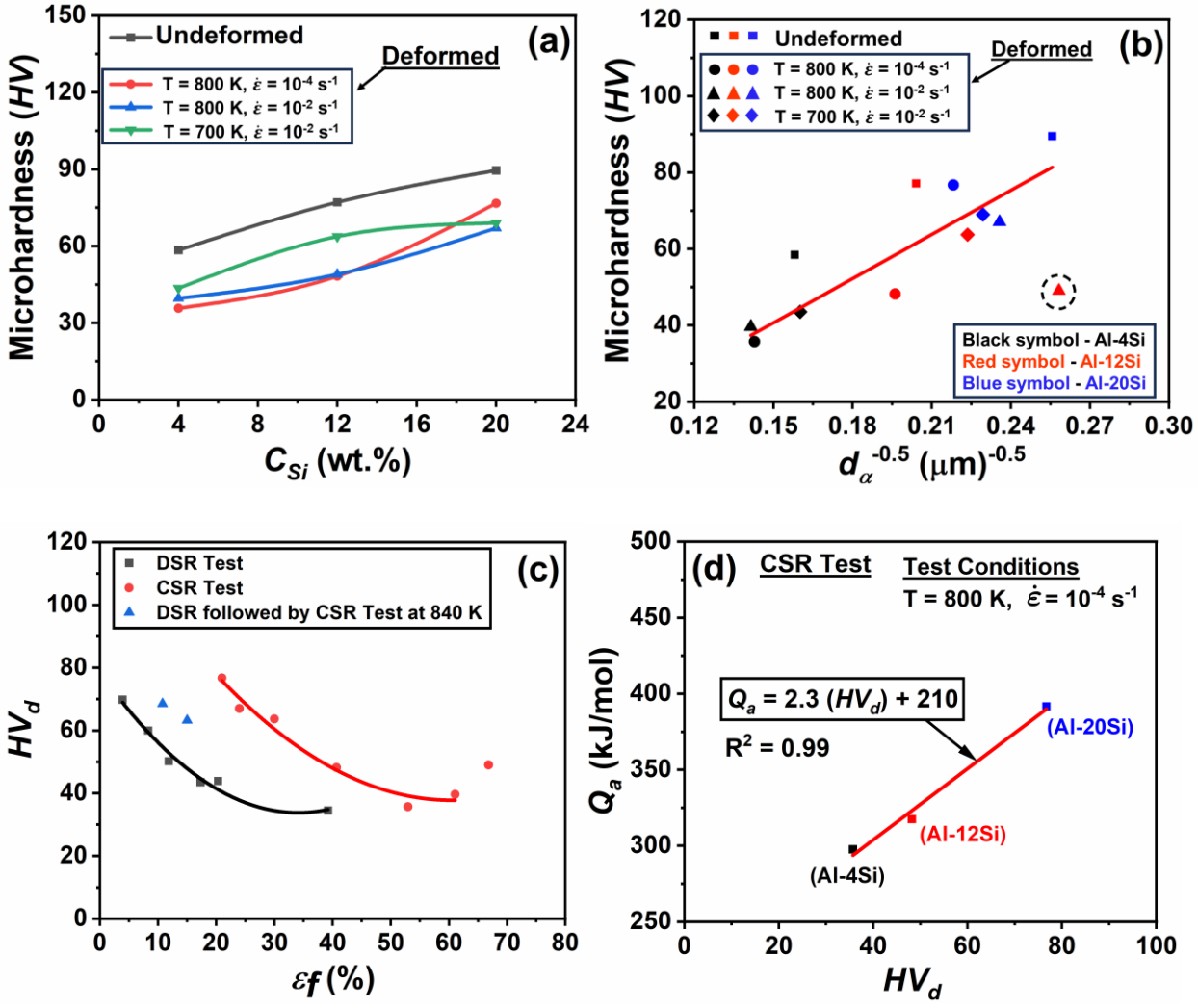


Figure 4.40 : (a) Microhardness measured before deformation and after deformation of the samples at different test conditions plotted as a function of Si content in as-cast Al-Si alloys, (b) Hall-Petch type plot for undeformed and deformed Al-Si alloys, (c) variation in room temperature hardness as a function of high-temperature elongation (ε_f) of samples, (d) a plot of Q_a for deformation and the post deformation room temperature hardness (HV_d) for the given composition and test conditions

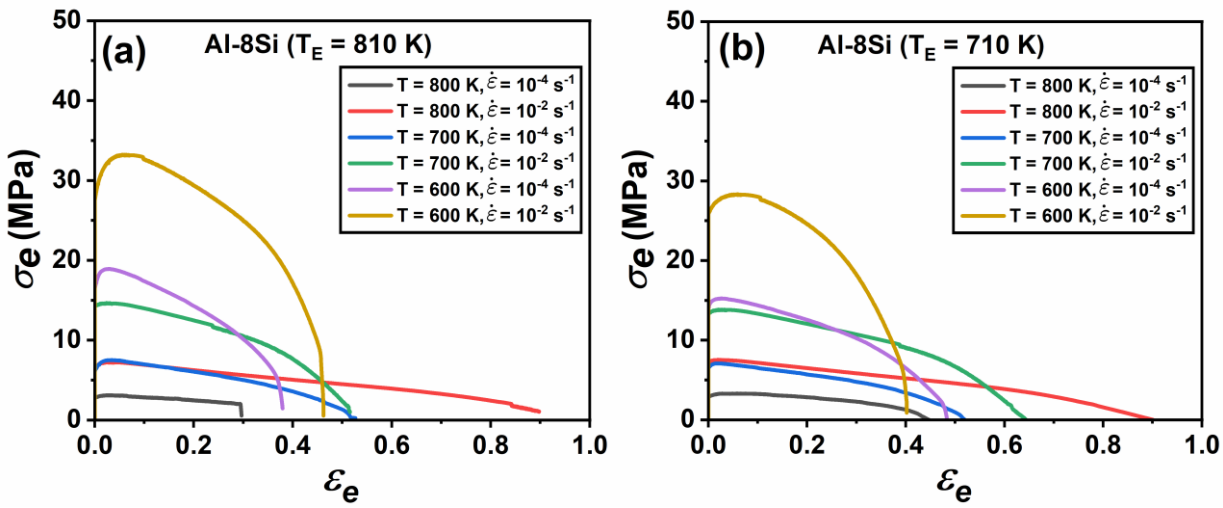
(b) Deformation Behaviour of Extruded Alloys

Stress-Strain Curves from CSR Tests

The stress-strain curves obtained from high-temperature tensile tests on Al-Si alloys, processed using the hot extrusion method, have been analysed under various test conditions, including different temperatures (600–800K) and strain rates (10^{-4}–$10^{-2}s^{-1}$). Figures 4.41(a-d) to 4.44(a-c) present these stress-strain curves for all the Al-Si alloys studied.

Figure 4.41(a-d) focuses on the σ-ε flow behaviour for the hypoeutectic Al-8Si alloy under different extrusion conditions. Figure 4.42(a-d) presents the σ-ε curves for eutectic Al-12Si, Figure 4.43(a-d) and Figure 4.44(a-c) show the σ-ε behaviour of hypereutectic Al-20Si and Al-30Si, respectively. Each σ-ε plot in Figures 4.41-4.44 consists of six distinct curves representing the effects of test temperature and strain rate on the mechanical response of the alloy. The results demonstrate that the flow stress generally increases with increasing strain rate and decreasing temperature for all the conditions investigated. Moreover, the nature of flow stress shows variation as a function of the alloy composition. The maximum flow stress is obtained at the lowest test temperature and higher strain rate for a given composition. On the other hand, regardless of the specific conditions, the elongation (ductility) reaches its maximum (~90%) at the highest test temperature (800K) and higher strain rate ($10^{-2}s^{-1}$) for hypoeutectic Al-8Si alloy. The elongation is noted to decrease with an increase in silicon content and a decrease in test temperature. Overall, the effects of strain rate and test temperature on flow curves are found to be more dominant in the hypoeutectic alloys than in the eutectic and hypereutectic alloys.

Notably, an interesting trend emerges from the data; in most cases (a-d), the peak stress values obtained at higher temperatures and higher strain rates (800K, $10^{-2}s^{-1}$) (red colour curve) are found to be approximately the same as those observed at an intermediate test temperature and lower strain rate (700K, $10^{-4}s^{-1}$) (blue colour curve). Similarly, in some cases, the peak stress values obtained at intermediate temperature and higher strain rate (700K, $10^{-2}s^{-1}$) (green colour curve) and at the lower test temperature and lower strain rate (600K, $10^{-4}s^{-1}$) (purple colour curve) are noted to be approximately the same. This suggests that specific combinations of temperature and strain rate may lead to similar peak stress levels, implying the existence of critical processing conditions that result in optimal mechanical properties for the Al-Si alloys during hot extrusion.



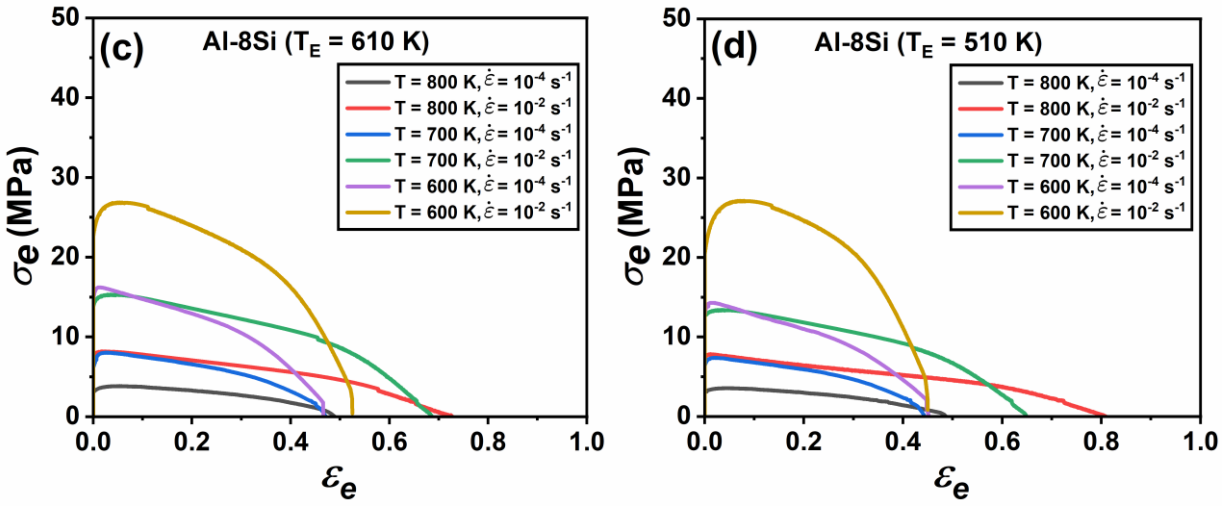


Figure 4.41 : Stress-strain curves obtained from tensile tests performed at different test conditions, viz. temperature (*T*) and strain rate ($\dot{\varepsilon}$) shown by legends in the figures for hypoeutectic (Al-8Si) Al-Si alloy extruded at (*ET*) (a) 810K, (b) 710K, (c) 610K, and (d) 510K

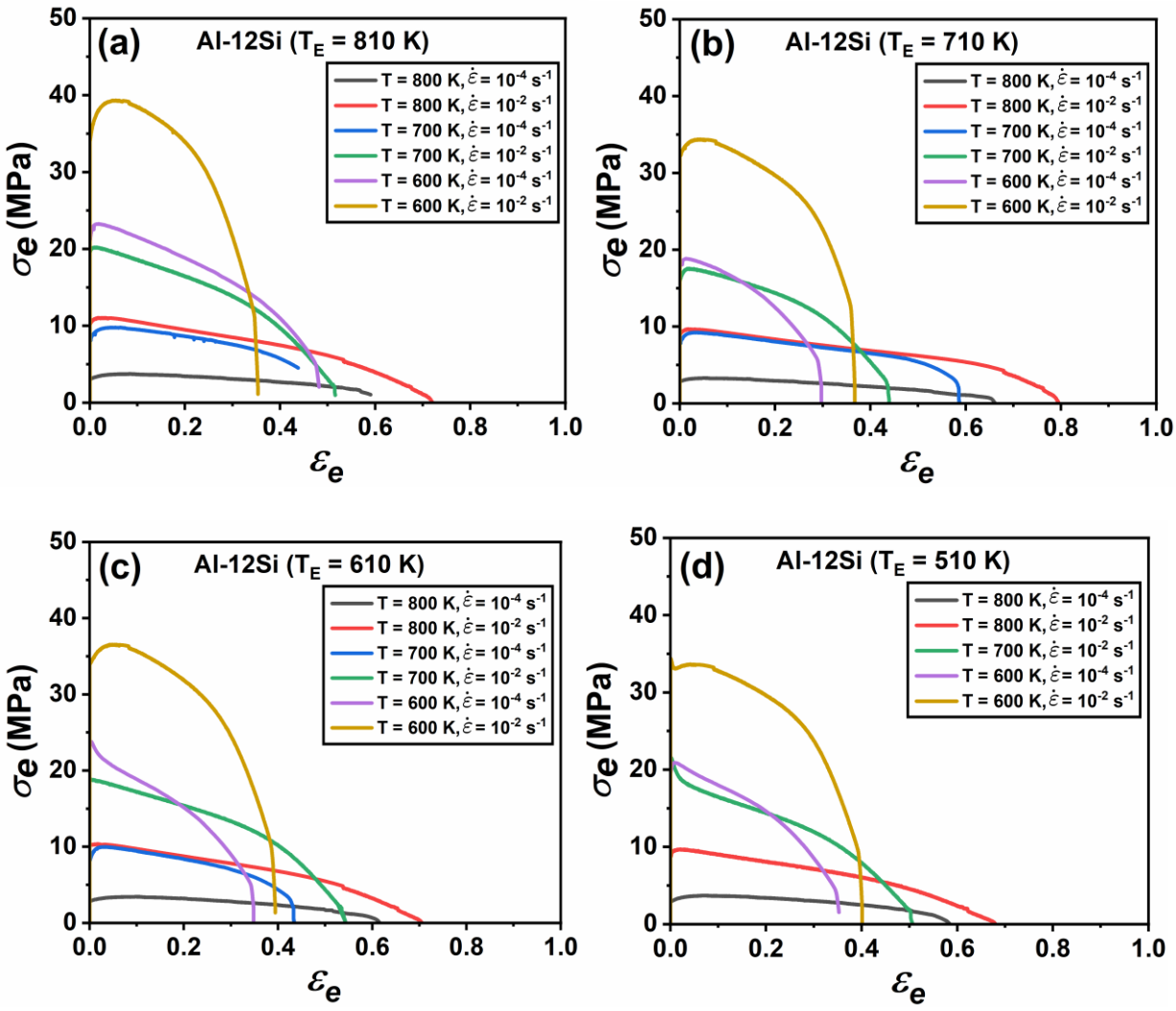


Figure 4.42 : Stress-strain curves obtained from the tensile test under different test conditions (*T*, $\dot{\varepsilon}$) as inset in the figures for eutectic (Al-12Si) Al-Si alloy extruded at (a) 810K, (b) 710K, (c) 610K, and (d) 510K

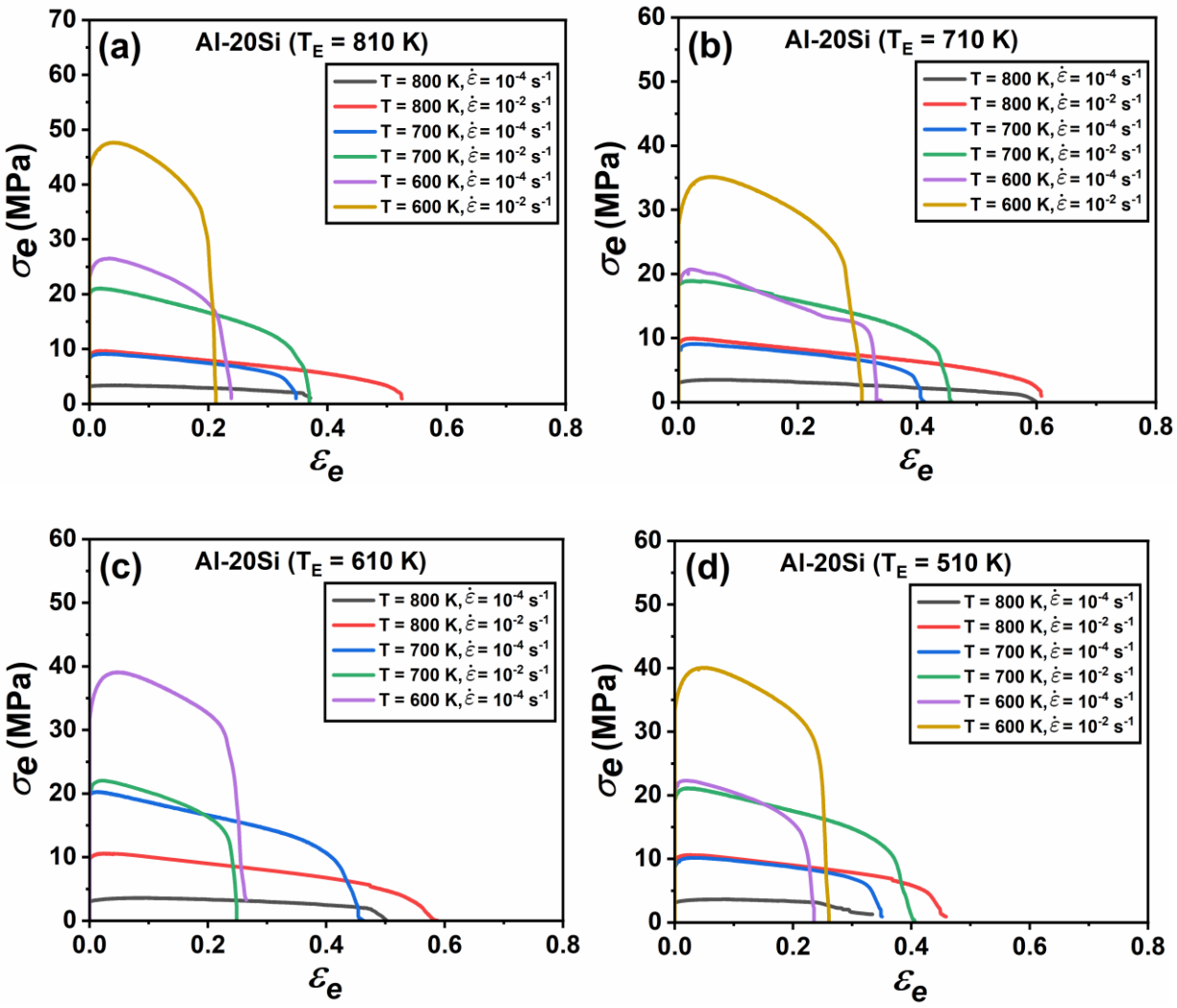
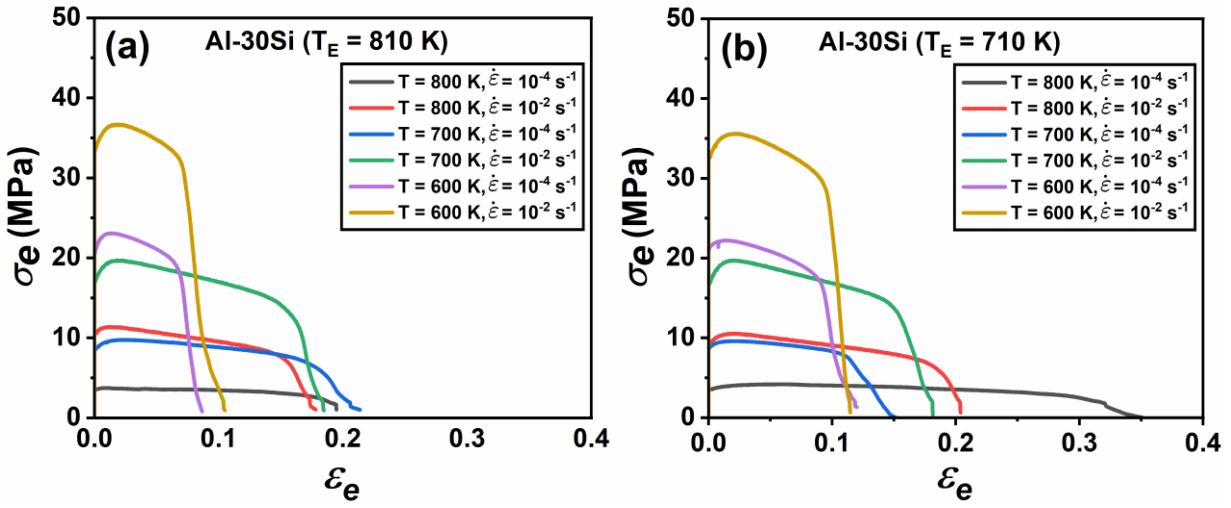


Figure 4.43 : Stress-strain curves obtained from the tensile tests performed at different test conditions (T, $\dot{\varepsilon}$) listed as legends in the figures for hypereutectic (Al-20Si) Al-Si alloy extruded (ET) at (a) 810K, (b) 710K, (c) 610K, and (d) 510K



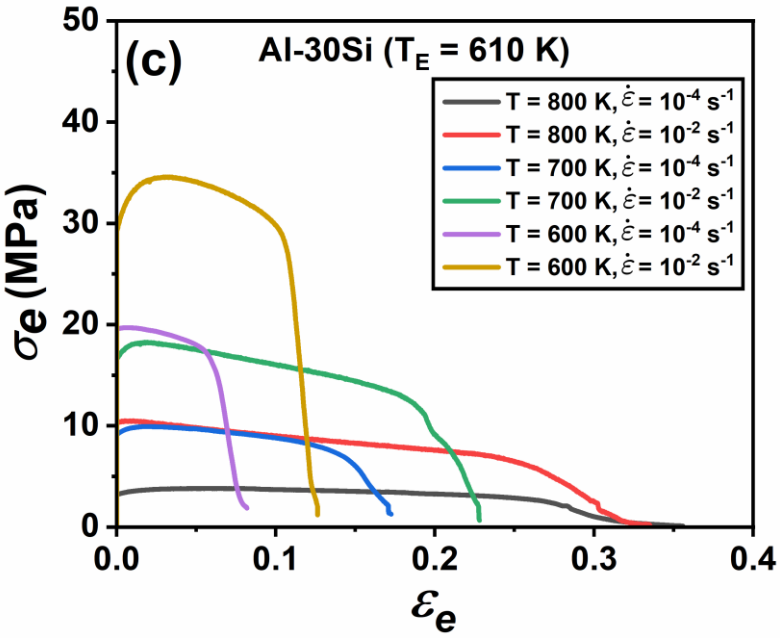


Figure 4.44 : Stress-strain curves obtained from the tensile tests performed at different test conditions (T, $\dot{\varepsilon}$), listed as legends in the figures, for hypereutectic (Al-30Si) Al-Si alloy extruded at (a) 810K, (b) 710K, (c) 610K

Zener-Hollomon parameters of the extrusion process employed for Al-Si alloys were determined by using the strain rate (speed-to-length ratio) and temperature conditions. Interestingly, the log-log plot of grain size as a function of Z reveals a linear fitting (Eq. 4.19) of all the data points, except for the eutectic alloy, independent of the condition. However, in the case of eutectic Al-12Si alloy, d_α varies linearly with Z without considering the encircled grain size and Z values in Figure 4.45.

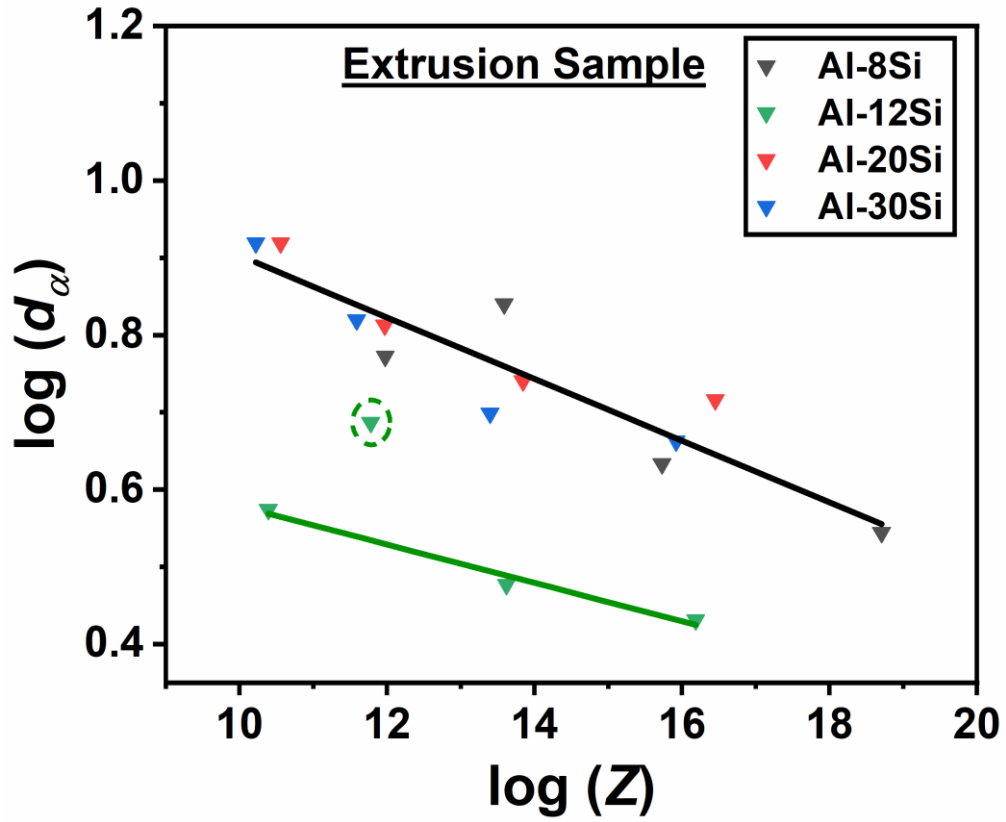


Figure 4.45 : log-log plot of grain size and Zener-Hollomon parameter of extrusion samples of Al-8Si, Al-12Si, Al-20Si, and Al-30Si alloys (the data point which is not included in curve fitting is encircled)

Stress-Strain Rate Behaviour of Extruded Alloy

Observations of the σ-ε curves (Figures 4.41-4.44) from the CSR tensile tests revealed that the extruded samples exhibited sufficient ductility, which can be utilized in the DSR test for testing at various strain rates and test temperature conditions. Stress (σ)-strain rate ($\dot{\varepsilon}$) data were obtained by using two different tensile test techniques: (i) CSR tests, (ii) DSR tests coupled with CSR tests (*SET1:* 800-450K, and *SET 2:* 840-800 K). It may be noted that these tests were planned only for the samples that were extruded at 810K. In case of (ii), firstly, the DSR test went up to the lowest test temperature of 450K for *SET1* and 800K for *SET2*, and then the same sample was followed by the CSR test up to failure at the highest test temperature of 800K for *SET1* and 840K for *SET2* both at the lower strain rate of $10^{-4}s^{-1}$. However, the hypereutectic Al-30Si alloy was not able to sustain such a coupled test due to poor ductility at the lower test temperature, which led to failure during the DSR test (*SET1*) at 550K itself.

Case (i): The apparent activation energy (Q_a) and m values were determined from the limited data of the CSR tests. These parameters were plotted as a function of silicon content (C_{Si}), Figure 4.46. Generally, m varied from 0.1 for hypereutectic Al-30Si at the lowest test temperature of 600K to 0.25 for the eutectic Al-12Si alloy at the highest test temperature of 800K, Figure 4.46(a). In most cases, the activation energy was observed to decrease with an increase in silicon content, Figure 4.46(b), which is very similar to the behaviour of the as-cast alloy. The magnitude of the Q_a varied from 140kJ/mol for the hypereutectic Al-30Si alloy to 242kJ/mol for the eutectic Al-12Si alloy.

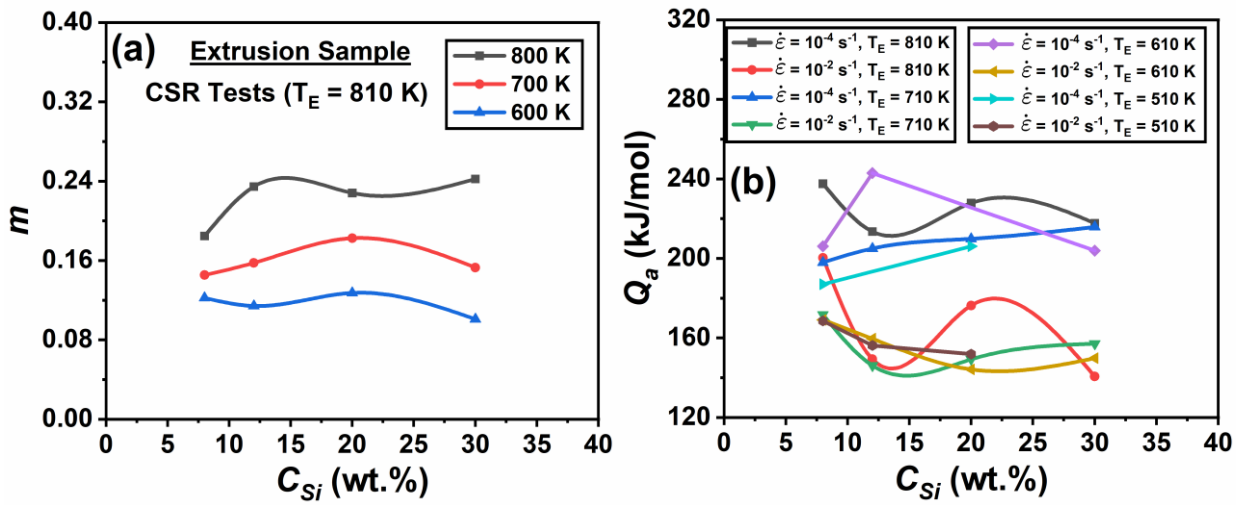


Figure 4.46 : Variation in (a) m, and (b) activation energy (Q_a) as a function of Si content as obtained from CSR test data

Case (ii): The coupled-type (DSR-CSR) tests were conducted in two sets of experiments. In *SET1*, the test temperature was set in the range from 800-450K, and the strain rate range from 10^{-4}-$10^{-2}s^{-1}$, whereas in *SET2* experiments, it was tried to explore the superplastic behaviour of extruded eutectic Al-12Si and hypereutectic Al-30Si alloys at a high temperature of 840K, which is close to their melting points. Coupled DSR tests, followed by CSR tests, were conducted to characterize this behaviour in the temperature range of 840-800K and the strain rate range of 10^{-4}-$10^{-2}s^{-1}$.

Figure 4.47(a-d) shows the σ-$\dot{\varepsilon}$ plots obtained from the DSR tests of *SET1* (800-450K) for all the alloy compositions, whereas Figure 4.48 shows the σ-$\dot{\varepsilon}$ plots obtained from DSR tests of *SET2* (840-800K) for Al-12Si and Al-30Si alloys. The flow stress was observed to increase with the increase in strain rate and decrease in test temperature. The slope of the straight line of the $ln\sigma$-$ln\dot{\varepsilon}$ plot represents the strain rate sensitivity index, denoted by m, which remained constant

with the change in strain rate in the lower test temperature regime. A slight deviation in the slope was observed at the highest test temperature, giving the highest *m* value.

From *SET1* data, overall, the values of *m* ranged from 0.06 to 0.26, with the highest value (*m*=0.26) recorded for the Al-20Si alloy at the highest test temperature of 800K and the lowest value (*m*=0.07) for the Al-30Si alloy at the lowest common test temperature of 550K.

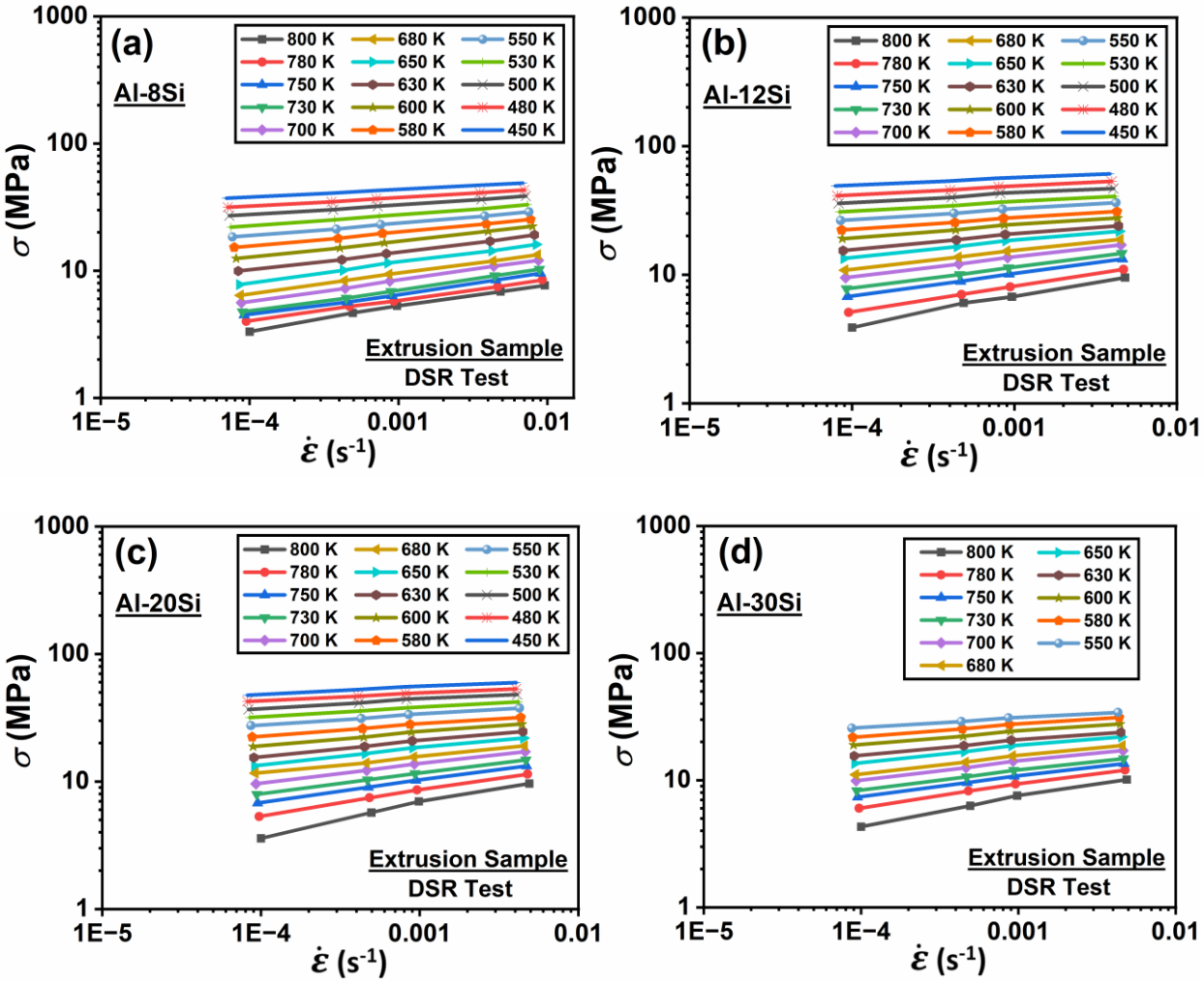


Figure 4.47 : Stress-strain rate plot obtained from DSR type tests (*SET1*) for extruded (a) hypoeutectic Al-8Si, (b) eutectic Al-12Si, (c) hypereutectic Al-20Si, and (d) Al-30Si alloys

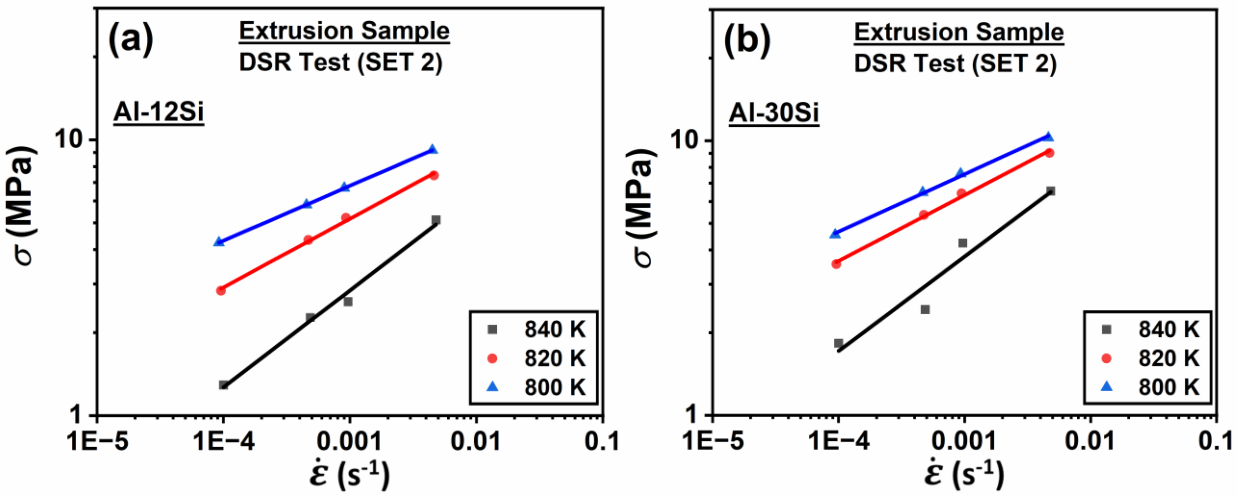


Figure 4.48 : Stress-strain rate plot obtained from DSR type tests (*SET2*) for extruded (a) eutectic Al-12Si and (b) hypereutectic Al-30Si alloys

A typical Arrhenius-type plot was constructed to determine Q_a using the DSR data for all test conditions, as shown in Figure 4.49(a-d). The Q_a was calculated by extracting the flow stress values at constant strain rates but at various temperatures for the Arrhenius plot.

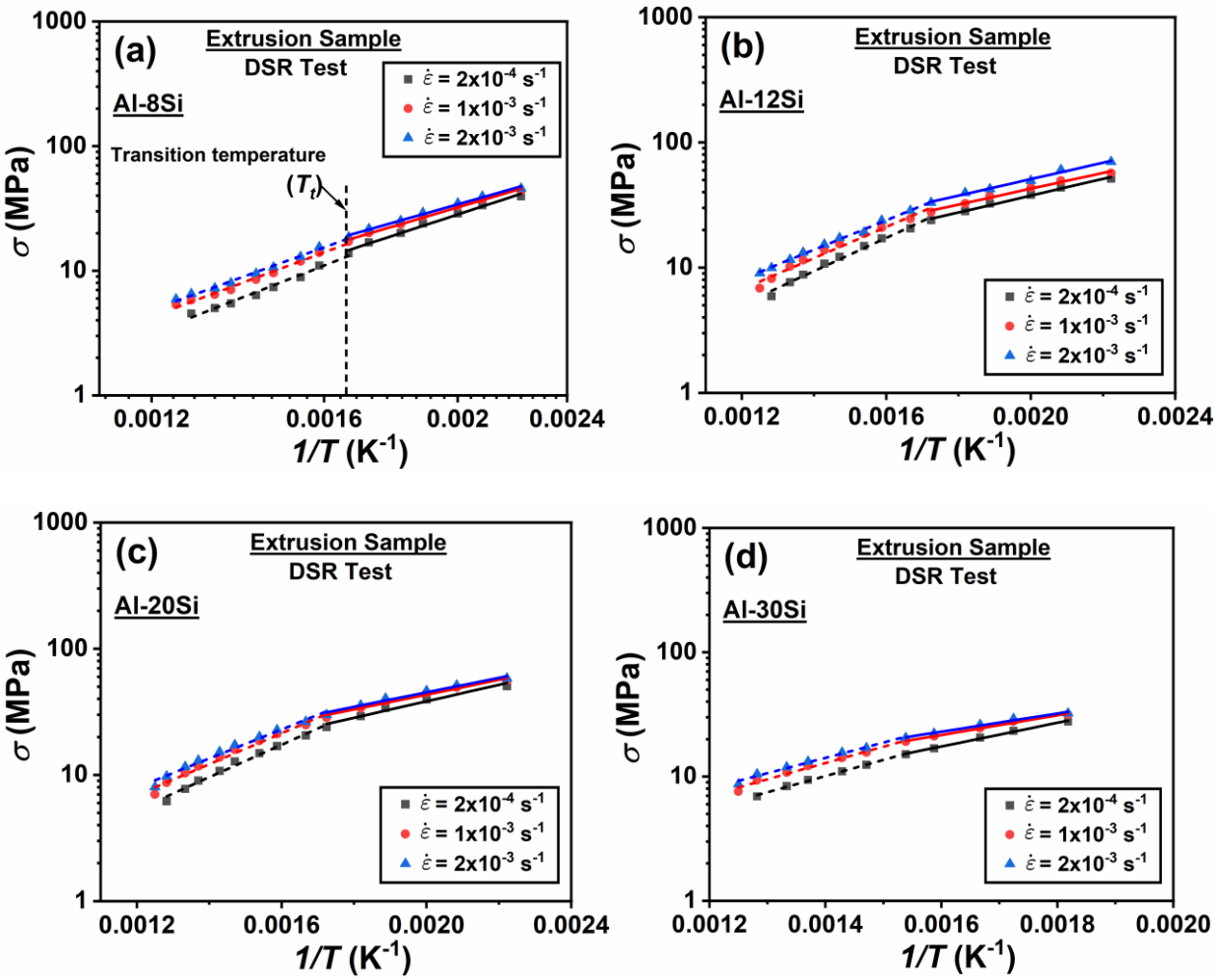


Figure 4.49 : Typical Arrhenius type plots obtained from differential strain rate tests for (a) Al-8Si, (b) Al-12Si, (c) Al-20Si, and (d) Al-30Si alloys extruded at 810K

The magnitude of m was plotted as a function of test temperature, Figure 4.50(a), whereas the maximum and mean values of m were plotted as a function of Si content, Figure 4.50(b). The magnitude of m is noted to increase as a function of increasing test temperature for all the alloy compositions. Also, a sharp increase in the m is found to be noted at a higher temperature range (*SET2*). As a function of composition, the variation in m is not noticeable except in the case of maximum values obtained from the *SET1* experiment. A marginal increase is noted for Al-20Si alloy.

Figure 4.50(c) shows the typical Arrhenius plot of the data obtained from the DSR tests (800-450K), which reveals the two slopes of the plot, depending on the test temperature and alloy composition. The true activation energy (Q_t) obtained is higher (179.2±21.4kJ/mol for Al-30Si) over the higher temperature region (550-800K), but it decreases with decreases in the lower test temperature (550-450K) regime to the value of 79.4±11.8kJ/mol for Al-20Si alloy. The variation in activation energy as a function of Si content is plotted in Figure 4.50(d), which reveals that Q generally increases with the increase in silicon content. From the DSR test data (840-800K), the strain rate sensitivity index (m) and the activation energy (Q) were calculated

and included in Figure 4.50(b,c). The total elongation was obtained from the coupled DSR, followed by CSR tests. For the eutectic Al-12Si alloy, the magnitude of m increased from 0.23 in *SET1* to 0.35 in *SET2*, while for the hypereutectic Al-30Si alloy, it increased from 0.22 in *SET1* to 0.34 in *SET2* at the highest test temperature. Similarly, the value of Q_t showed significant variations, rising from 89.8±12.3kJ/mol to 370±145kJ/mol for the eutectic Al-12Si alloy and from 108.6±11kJ/mol to 308.9±153kJ/mol for the hypereutectic alloy. The true and apparent activation energy shows a mutual relationship (Eq. 4.20), as shown in Figure 4.50(e).

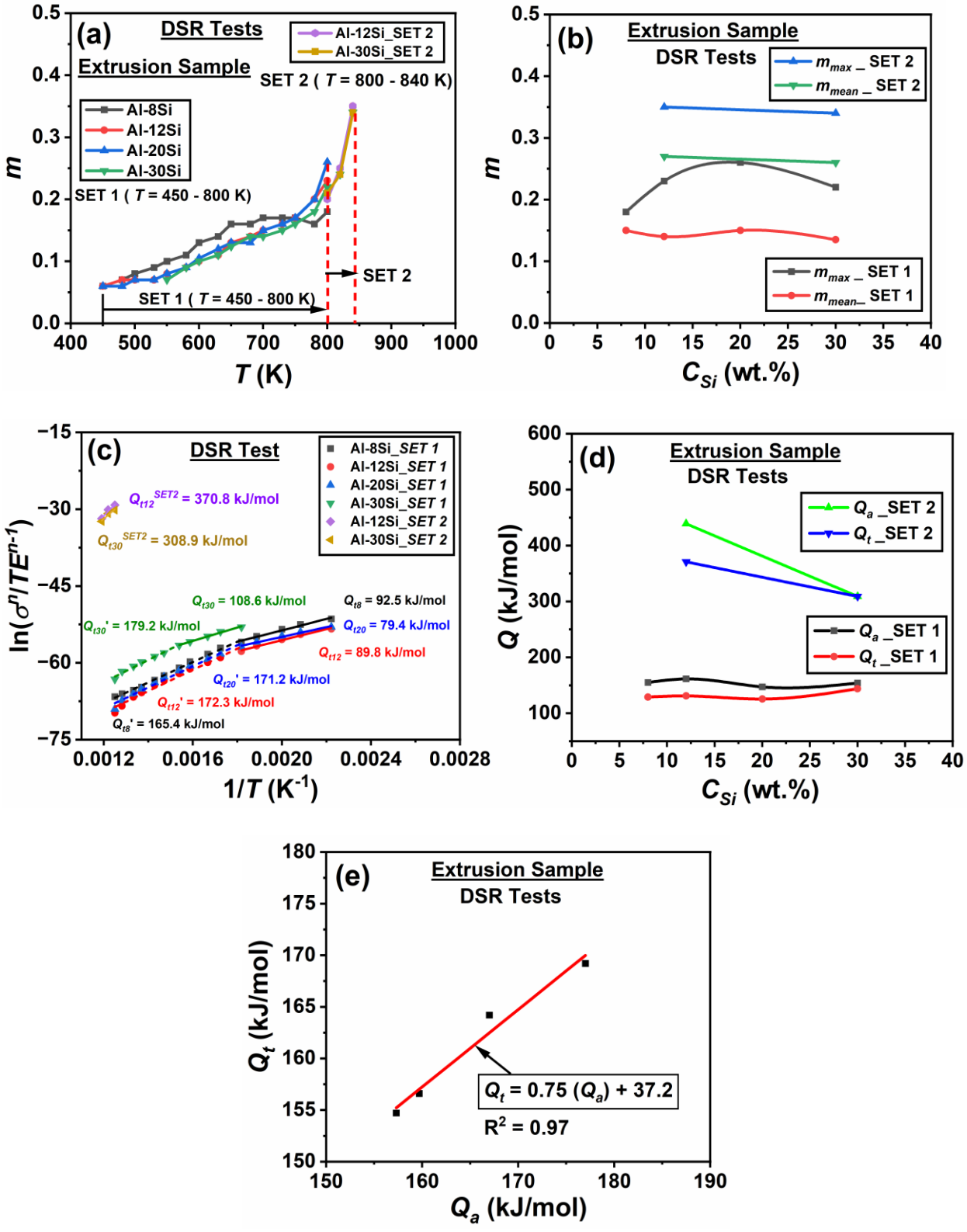


Figure 4.50 : Parameters of constitutive relationship for high-temperature deformation of extruded alloys, calculated from DSR tests: *m* as a function of (a) test temperature, (b) silicon content, (c) typical Arrhenius plot

of DSR tests (*SET1* & 2), (d) apparent (Q_a) and true activation energy (Q_t) as a function of silicon content, and (e) comparison of apparent and true activation energies corresponding to different Si contents

Furthermore, the elongation values of the alloys were compared. It was found that the eutectic Al-12Si alloy demonstrated a remarkable increase in elongation from 58.8% in *SET1* to ~100% in *SET2* (from both differential and constant strain rate coupled tests). The hypereutectic Al-30Si alloy also exhibited enhanced elongation, rising from 16.7% in *SET1* to ~65% in *SET2*. In contrast to these values, the maximum elongations obtained from the CSR tests were 72% and 21.4%, respectively. Figure 4.51 shows the stress-strain plot from the CSR test after the DSR test. Similar to the as-cast alloys, this was obtained from the coupled DSR-CSR tests of Al-12Si and Al-30Si alloys. In both the stress-strain curves, initially the flow hardening is noted to be dominant, and then the flow softening occurs due to localized deformation and microstructural changes to overcome the former mechanism of hardening. Al-12Si alloy showed higher elongation, whereas Al-30Si exhibited higher flow stress at the given test condition.

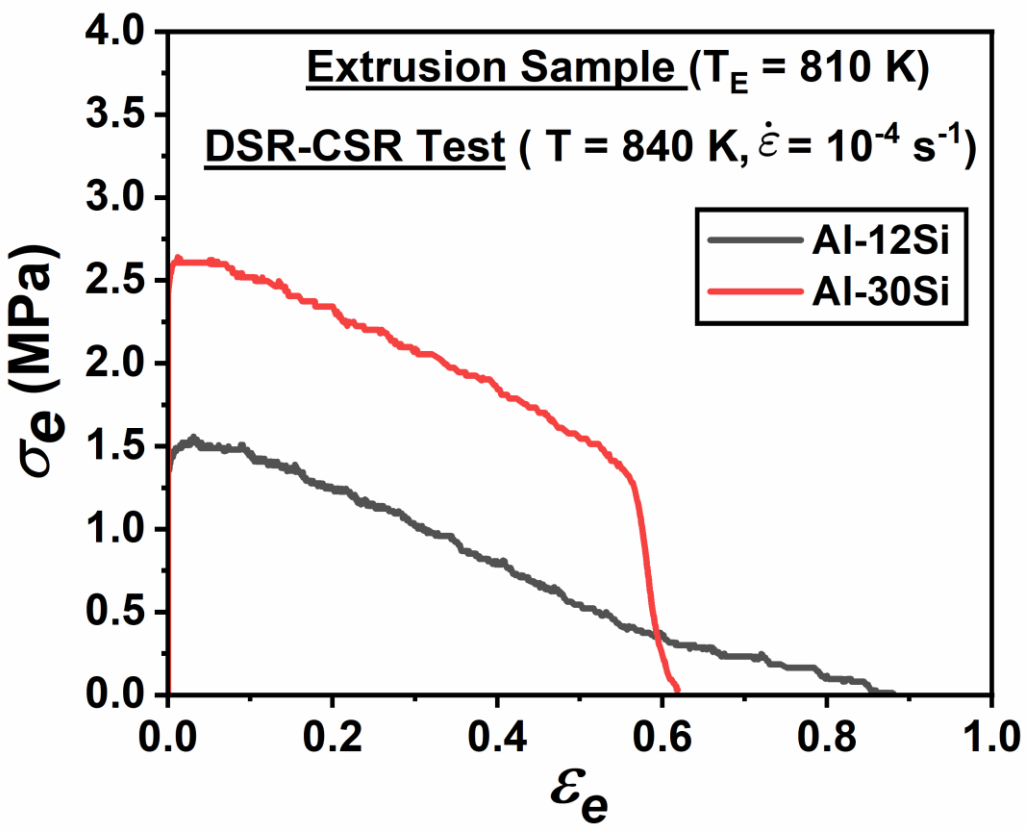


Figure 4.51 : Stress-strain rate curves obtained from the coupled DSR (840-800K) followed by CSR tests conducted at test temperatures of 840K and strain rate of $10^{-4}s^{-1}$ for eutectic Al-12Si alloy and hypereutectic Al-30Si alloy extruded at 810K

Microstructure Examination after High-Temperature Deformation

Typical microstructures of extrusion samples deformed to fracture under CSR tests at 800K and $10^{-2}s^{-1}$ were examined for hypoeutectic Al-8Si, eutectic Al-12Si, and hypereutectic Al-20Si alloys, as shown in Figure 4.52(a-f). The resulting microstructures displayed characteristics of pseudo-brittle fracture, with the presence of large voids. Cracks formed along the interphase boundary between the Al matrix and the Si particles, Figure 4.52(f). In the Al-8Si alloy, no cavities were formed, but instead, necking was observed. The Al-12Si eutectic alloy exhibited small spherical cavities near the fracture tip, with grains and particles aligned and elongated in the direction of loading. Conversely, the Al-20Si alloy showed large, interconnected cavities along the loading direction. There was evidence of grain growth and coarsening of Si particles in the hypoeutectic Al-8Si alloy, while the eutectic Al-12Si and hypereutectic Al-20Si alloys showed minimum change, as illustrated at higher magnification in Figure 4.52(b-d-f).

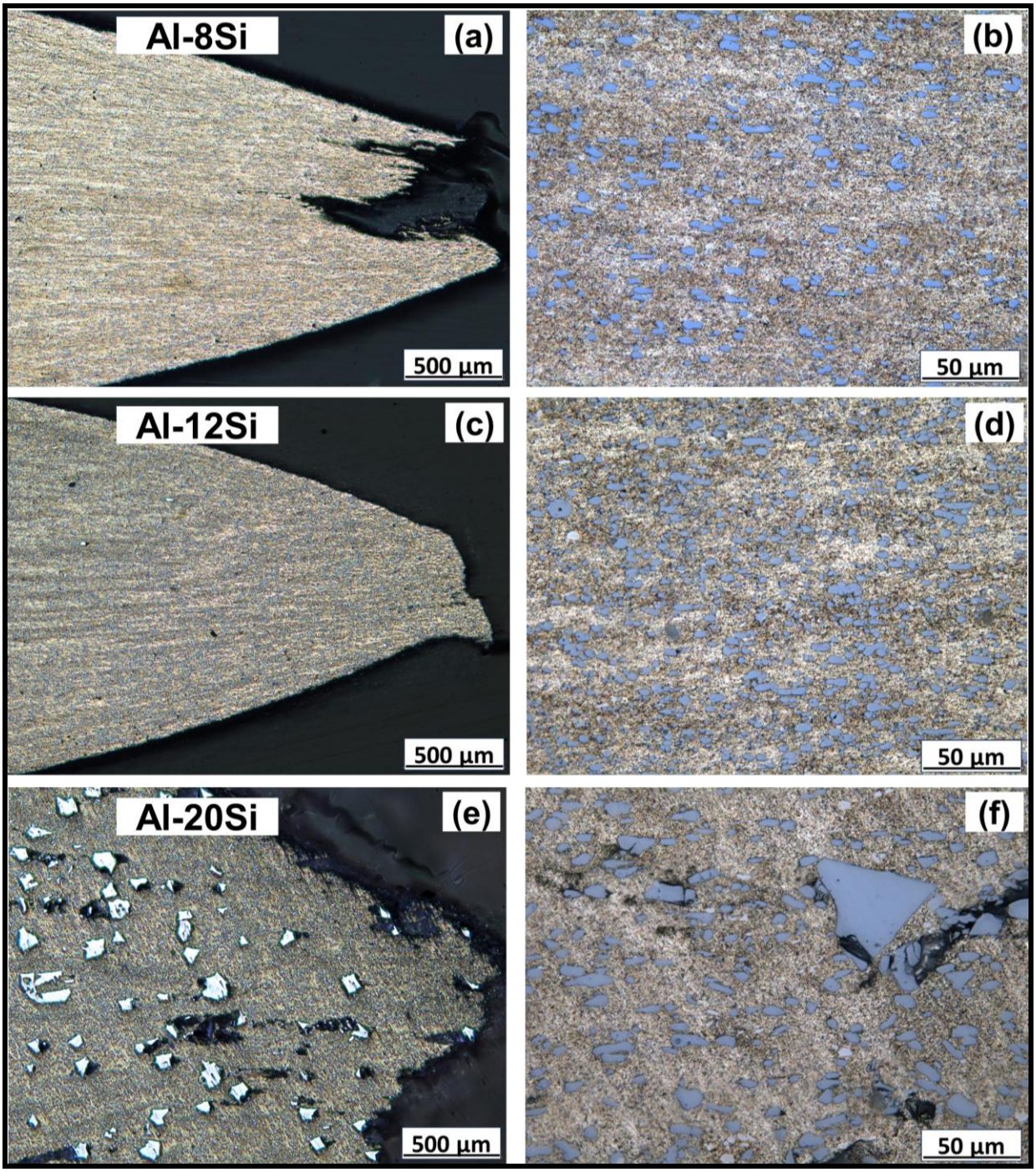


Figure 4.52 : Low magnification micrographs of deformed samples from CSR tests (a-c-e), (b-d-f) corresponding to higher magnification micrographs of the fracture tips

(c) Deformation Behaviour of FSPed Alloys

Stress-Strain Curves from CSR Tests

The σ-ε curves were carefully examined for three-pass friction stir processed (FSP) Al-Si alloys, which were subjected to tensile tests at a constant initial strain rate of $10^{-4}s^{-1}$ and the test temperature of 840K. Shown in Figure 4.53(a) are the σ-ε curves so obtained along with the silhouette of deformed tensile specimens from the CSR tests, Figure 4.53(b), of hypoeutectic Al-8Si, eutectic Al-12Si, hypereutectic Al-20Si, and Al-30Si alloys. Notably, the results showed that both the yield strength and ultimate tensile strength increased as the silicon content increased from eutectic to hypereutectic compositions. Surprisingly, the hypoeutectic Al-8Si alloy exhibited the highest value of strength among the alloys investigated. All the σ-ε curves in

Figure 4.53 (a) initially exhibit flow hardening to peak stresses, followed by prolonged flow softening to varying failure strains. The maximum elongation of ~250% was shown by Al-20Si alloy, whereas elongations of 159%, 141%, and 131% were recorded for Al-30Si, Al-8Si, and Al-12Si alloys, respectively, showcasing their superplastic behaviour. The peak stresses in the σ-ε curves for these alloys are found to vary as 1.4MPa, 1.9MPa, 2.0MPa, and 1.2MPa, respectively. In all the cases, the fractures revealed are of a pseudo-brittle nature.

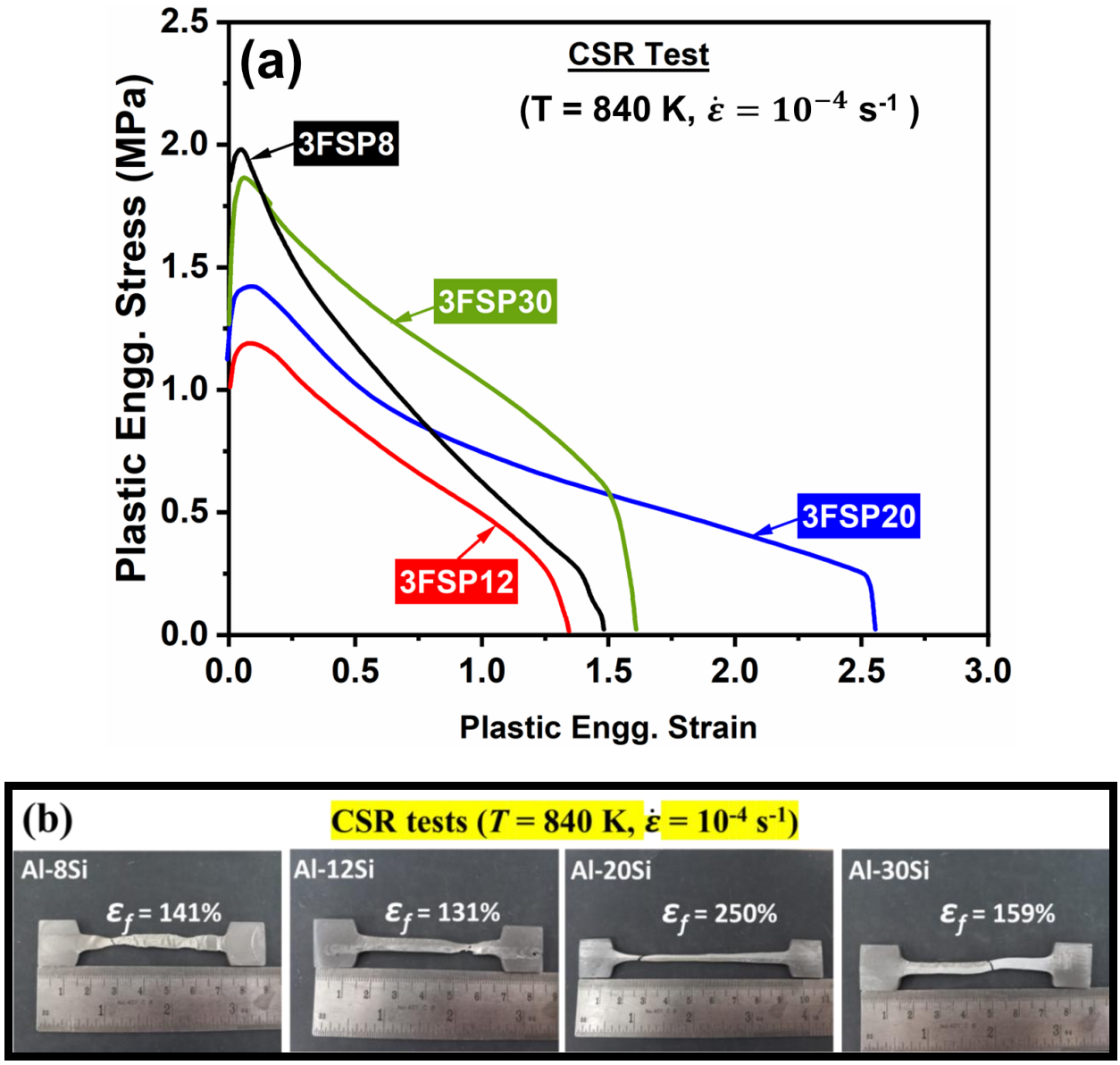


Figure 4.53 : (a) stress-strain curves obtained from CSR tensile tests conducted at a high temperature of 840K and strain rate of $10^{-4}s^{-1}$ for three-pass FSP processed Al-Si alloys having compositions inserted in the legends (Each curve corresponds to specific alloy compositions as denoted in the legends), and (b) total elongation (ε_f) represented in the silhouette of deformed tensile specimens undergone CSR tests

Stress-Strain Rate Behaviour of FSPed Alloy

Stress (σ)-strain rate ($\dot{\varepsilon}$) data were collected over the strain rate range of ~10^{-4}-$10^{-2}s^{-1}$ and at test temperature ranges of (i) 800-530K and (ii) 840-800K, using separate samples for each temperature range, by DSR technique. Presented in Figure 4.54(a-d) are the σ-$\dot{\varepsilon}$ plots for all the alloy compositions and the whole temperature range investigated. The data of parameters of the constitutive relationship are listed in Table 4.7. The following observations can be made from these values and σ-$\dot{\varepsilon}$ plots:

(i) The σ-$\dot{\varepsilon}$ plots at lower test temperatures (T≤650K) show a linear trend at each temperature but a decrease in stress values with the increase in test temperature. The slope of σ-$\dot{\varepsilon}$ plot, called m, is found to be a minimum of 0.07 in Al-30Si at 600K and a maximum of 0.40 in Al-12Si at 840K, Table 4.7. The magnitude of m increases with increasing temperature, Figure 4.57(a), but decreases with increasing Si content, as shown in Figure 4.57(b).

(ii) The σ-$\dot{\varepsilon}$ plots corresponding to the two test temperature ranges of (i) 800-530K and (ii) 840-800K show a variation in stress levels and m value at the common test temperature of 800K. The tests started at 840K of the higher temperature range (840-800K) and continued up to 800K, revealing higher flow stress and lower m than those that started at 800K and continued to the lower test temperatures.

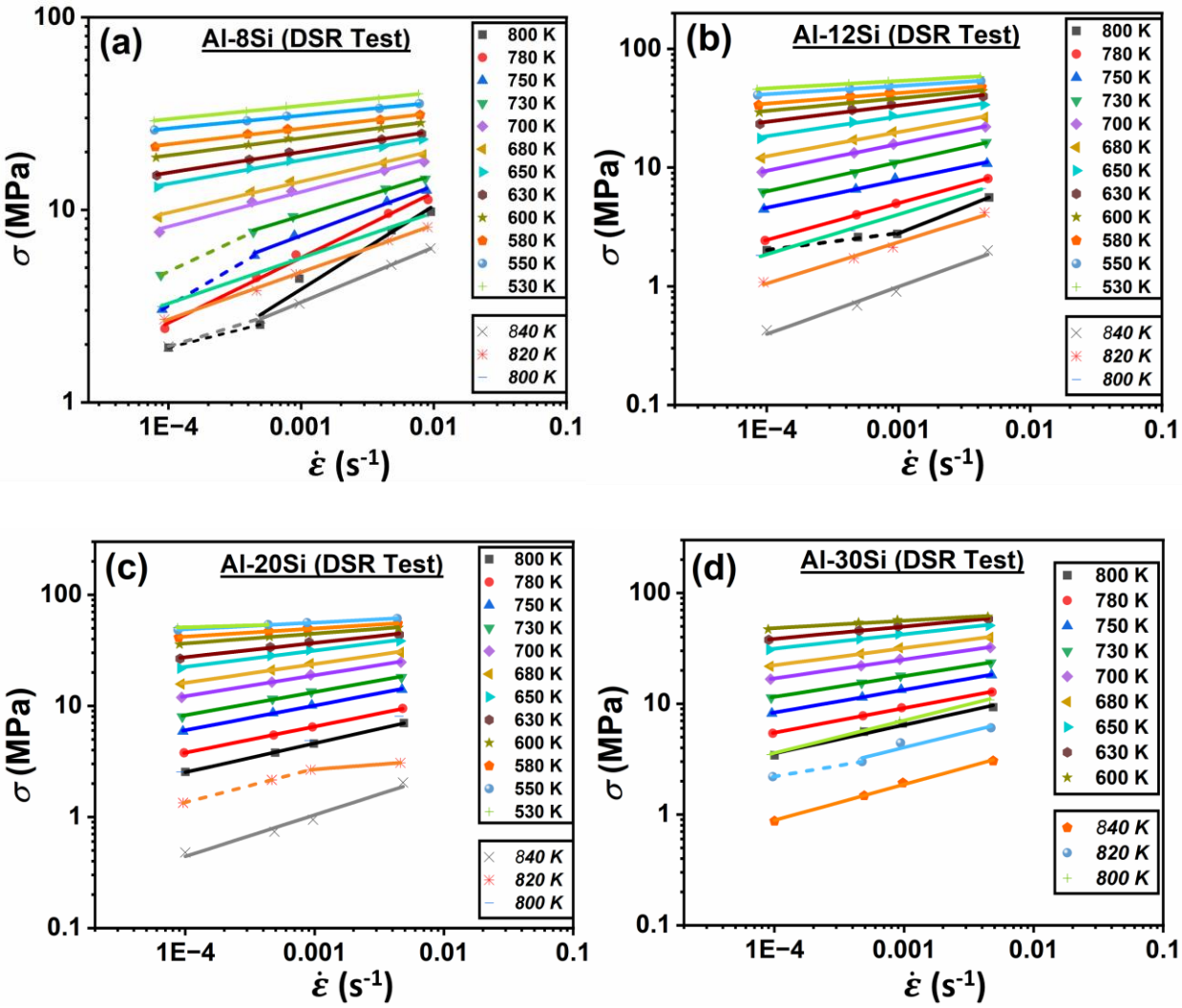


Figure 4.54 : Stress (σ)-strain rate ($\dot{\varepsilon}$) plots, obtained from DSR tests of all the test temperature ranges (840-530K), of (a) Al-8Si, (b) Al-12Si, (c) Al-20Si, and (d) Al-30Si FSP processed Al-Si alloys. Note: In the figure legends, case (ii) temperature range (840-800K) is presented in Italic style to make a difference from case (i), temperature range (800-530K)

To evaluate the activation energy, $ln(\sigma)$ vs. $(1/T)$ Arrhenius plots were made for all the alloys, as shown in Figure 4.55(a-d). From these plots, the apparent activation energy (Q_a) was determined. The apparent and true activation energy for deformation was determined by using Eqs.(3.13) and (3.14). Shown in Figure 4.55(e) is the typical Arrhenius plot for Q_a (800-530K), wherein there appears bi-linear behaviour generally suggesting the higher values of activation energy at higher temperatures and lower Q_a at lower test temperatures with a transition temperature appearing at ~650K. It is also found that Q_a increases with increasing Si content in

the alloy, Figure 4.57(d). The hypereutectic Al-30Si alloy displayed the highest Q_a value, reaching a maximum of 285.5±120kJ/mol. Conversely, the eutectic Al-12Si alloy exhibited the lowest Q_a value, measuring 128.8 ± 52.3 kJ/mol. Similar behaviour was noted in the case of Q_t, but it was generally lower than that of Q_a, Figure 4.57(c,d). The values of Q_a and Q_t for different alloys and temperature ranges are listed in Table 4.7.

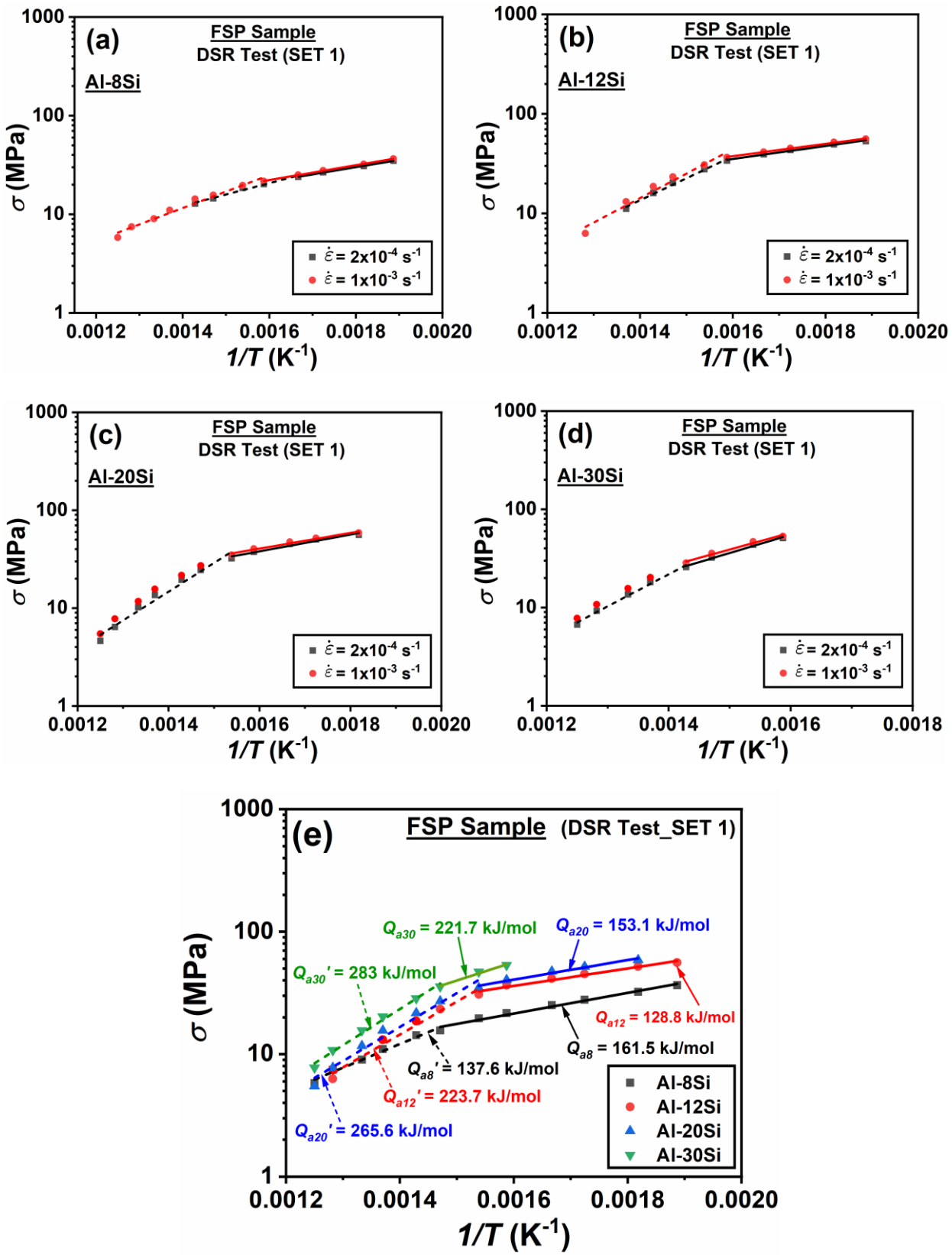


Figure 4.55 : (a-d) Typical Arrhenius-type plot obtained from differential strain rate tests for all the alloy compositions processed by three-pass FSP, (g) comparison of Arrhenius plot (Q) for all the alloy compositions

In view of the fact that the samples Al-8Si deformed from 840K to 800K showed higher flow stress than that deformed from 800K and below, Figure 4.54(a), the Arrhenius plot was considered separately in the case of (ii) 840-800K, Figure 4.56. However, even in this case, the magnitudes of Q_a and Q_t are found to be comparable.

A coupled DSR test followed by a CSR test on the same sample was performed further to investigate the superplastic behaviour of the Al-Si alloys. Only the samples of hypoeutectic (Al-8Si) and eutectic (Al-12Si) alloys were able to withstand these tests, as the other hypereutectic Al-Si alloys (Al-20Si, Al-30Si) experienced fracture during the DSR tests (800-530K), whereas for DSR (840-800K), all the Al-Si alloy compositions tested successfully for coupled DSR-CSR tests. This test was started at a higher test temperature and gradually decreased to a lower temperature, using the same strain rates as in the previous tests. The values of m varied between the minimum of 0.26 for the hypoeutectic Al-8Si alloy and the maximum of 0.4 for the eutectic Al-12Si alloy at 840K. The determined activation energy for deformation revealed a maximum value of 571.4±77.6kJ/mol for the hypereutectic Al-30Si alloy, while the hypoeutectic Al-8Si alloy exhibited the lowest value of 278.7±79.4 kJ/mol, Figure 4.56, Table 4.7. In Figure 4.57(b,d), the variation of the constitutive parameters, m, and the activation energy, Q, with respect to C_{Si} is depicted. The value of m initially increases with increasing Si content up to the eutectic Al-12Si alloy, but subsequently decreases with an increase in C_{Si}. On the other hand, Q shows an increasing trend with C_{Si} until reaching its peak value for the Al-30Si alloy. However, for the Al-30Si alloy, Q seems to be saturated. Notably, these values demonstrate an increase compared to that obtained in the previous tests conducted at lower test temperatures. The maximum elongation was observed in the eutectic Al-12Si alloy, reaching a remarkable value of over 341%, while the hypoeutectic Al-8Si alloy exhibited a minimum elongation of 77.3%. The elongation values were found to vary depending on the C_{Si} content, initially increasing for the eutectic alloy and subsequently decreasing with higher C_{Si} levels. Figure 4.57(f) illustrates the relationship between total elongation and m (Eq. 4.21), revealing that the maximum elongation was achieved at the optimal m value corresponding to the eutectic composition. At these test conditions, the eutectic Al-12Si alloy demonstrates its superplastic nature through the combination of m≥0.3 and total elongation ≥300%. This indicates that the alloy exhibits exceptional ductility and the ability to undergo extensive deformation without premature fracturing.

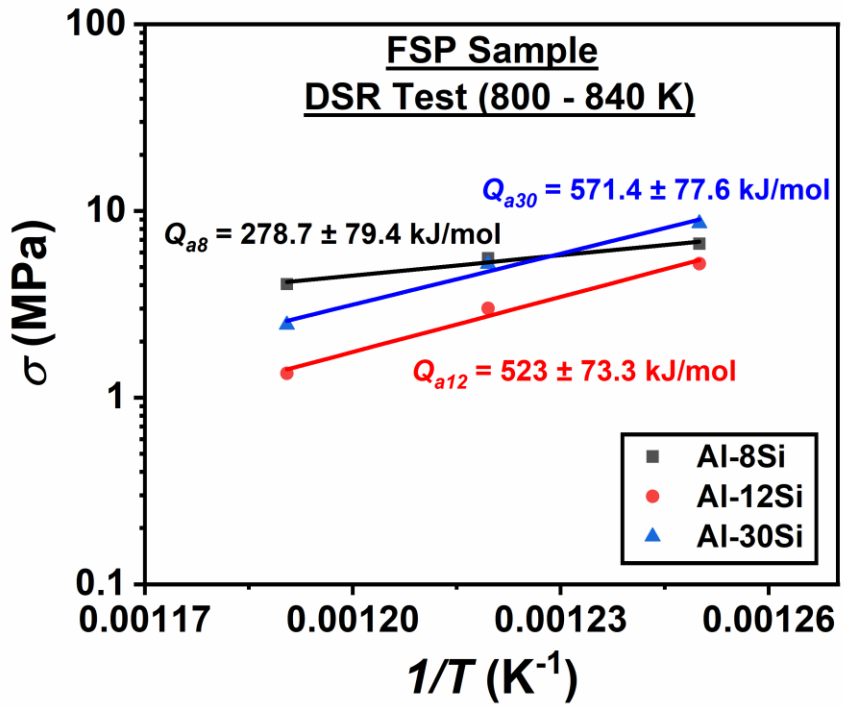
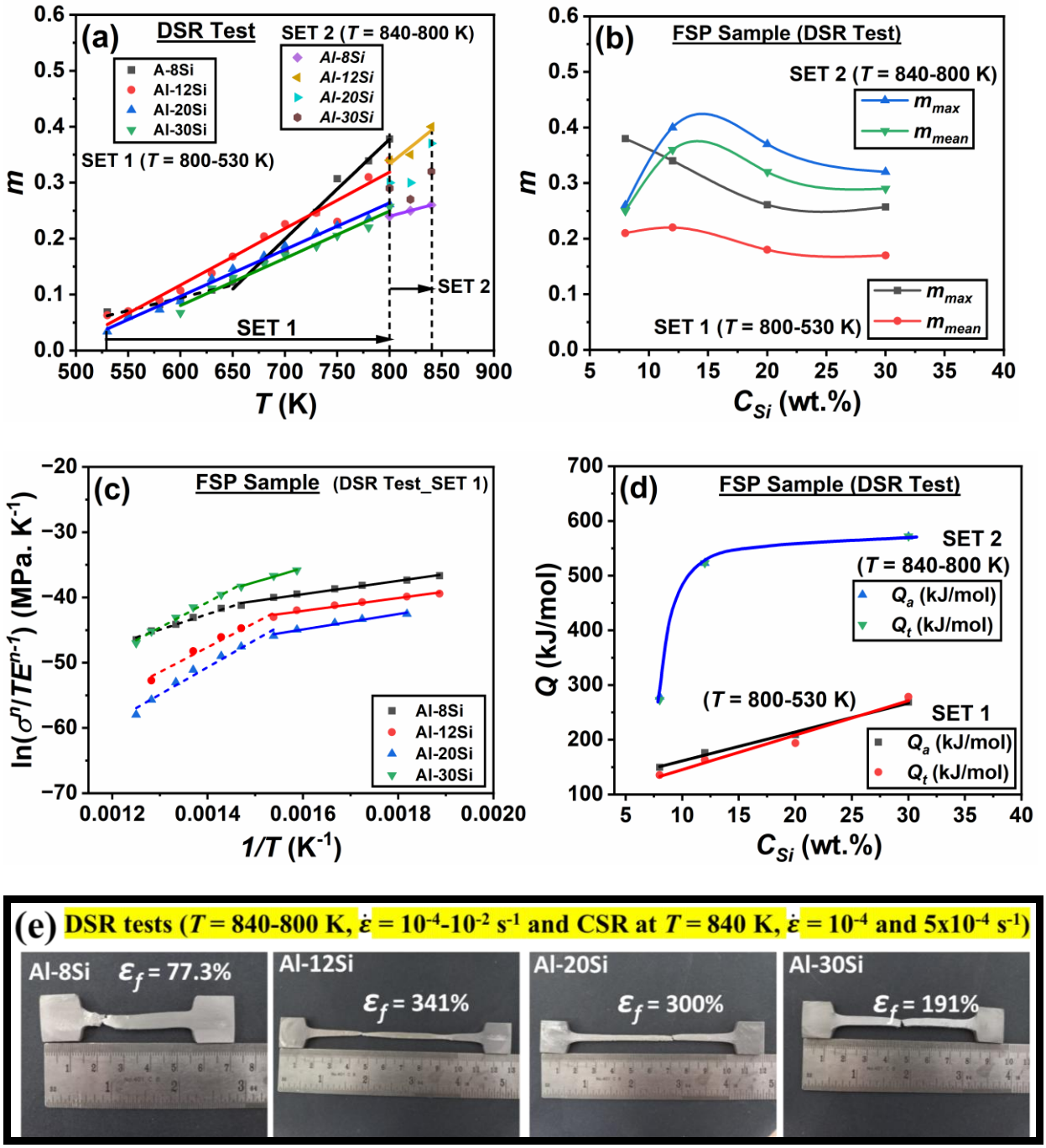


Figure 4.56 : Typical Arrhenius-type plot obtained from DSR tests (840-800K) for all the alloy compositions processed by three-pass FSP



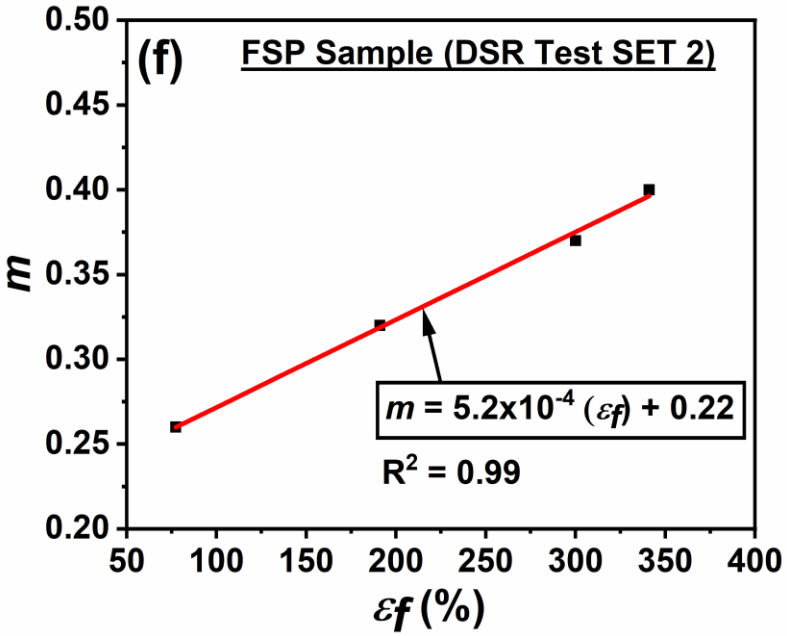


Figure 4.57 : Plot of strain rate sensitivity index (m) data obtained from all temperature ranges as a function of (a) test temperature, (b) Si content, (c) typical Arrhenius plot of data obtained from all temperature ranges, (d) variation in activation energy (Q_a and Q_t) as a function of Si content for all the temperature range involved, (e) silhouette of deformed tensile specimens undergone couple DSR-CSR tests of Al-8Si, Al-12Si, Al-20Si and Al-30Si alloys, and (f) dependence of total elongation (ε_f) on m in DSR-CSR coupled tests at temperature range of 840-800K

Table 4.7 : Activation energy (Q_a, Q_t) and strain rate sensitivity index (m) values for deformation of FSP processed Al-Si alloys over different ranges of temperatures

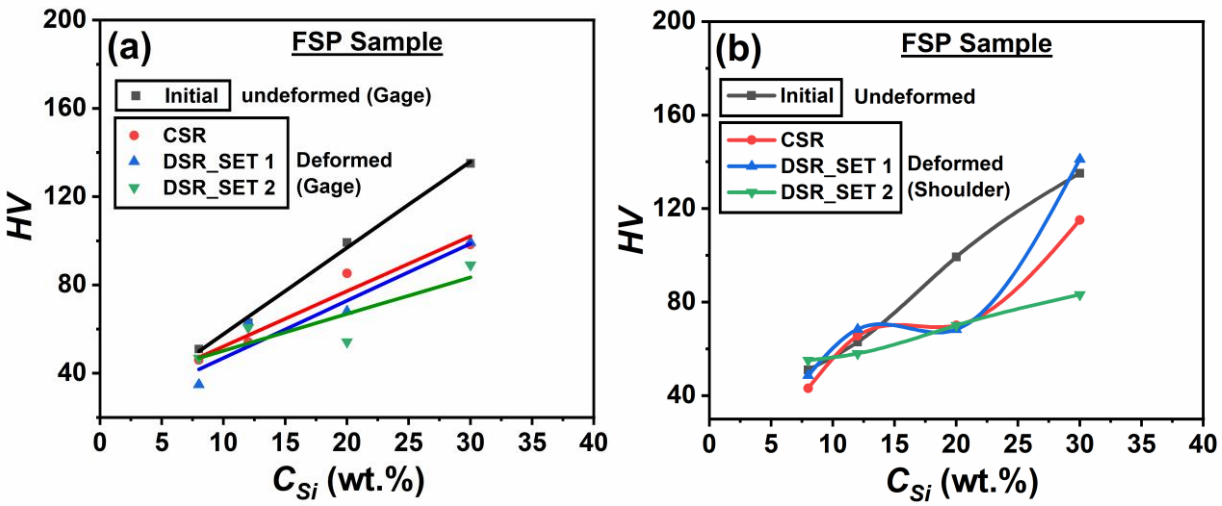
Material	Constitutive Parameter (T=80 -530K, $\dot{\varepsilon}$=10^{-4}–$10^{-2}s^{-1}$)					
	Q (kJ/mol) ($T_{trans} \approx 650K$)				m	
	$Q_{al}^{FSP}(T \geq T_{trans})$	$Q_{all}^{FSP}(T \leq T_{trans})$	$Q_{al}^{FSP}(T \geq T_{trans})$	$Q_{al}^{FSP}(T \leq T_{trans})$	m_{max}	m_{mean}
Al-8Si	137.6±33	161.5±19.5	135.1±26.8	135.7±9.6	0.38	0.21
Al-12Si	223.7±77.6	128.8±52.3	221.5±58	104.7±14.4	0.34	0.22
Al-20Si	265.6±68.1	153.1±68	262.1±53	125.8±18.7	0.26	0.18
Al-30Si	285.5±120	252±178	310.4±32.3	246.2±31.8	0.26	0.17
Constitutive Parameter (T=840-800K, $\dot{\varepsilon}$=10^{-4}–$10^{-2}s^{-1}$)						
	Q_a		Q_t		m_{max}	m_{mean}
Al-8Si	278.7±79.4		272.9±97.8		0.26	0.25
Al-12Si	523±73.3		523±127		0.4	0.36
Al-20Si	-		-		0.37	0.32
Al-30Si	571.4±77.6		572±148		0.32	0.29

Furthermore, the microhardness values of the deformed samples after CSR and DSR tests were measured to analyse the effects of deformation conditions and the concurrently evolved microstructure on the room temperature property of Al-Si alloys. The variation in hardness of the gage section and shoulder section as a function of alloy composition is depicted in Figure 4.58(a,b). It is noted that the microhardness of the deformed samples is lower than that of the initial or undeformed samples of the gage section, whereas, in some cases, the hardness of the shoulder section is registered as higher than that of the initial sample. Moreover, the variation in microhardness of the deformed (gage section) and heat-treated (shoulder) samples is noted to increase with silicon content, similar to the behaviour observed in undeformed samples. The microhardness values are found to be maximum for hypereutectic Al-30Si and lowest for hypoeutectic Al-4Si alloy. In general, the microhardness of the DSR (840-800K) conditions is obtained to be lower than that of the other deformation conditions. This reveals the softening nature of the high-temperature deformation of the Al-Si alloy.

Further, it was tried to analyse the effect of softening during high-temperature deformation on room-temperature hardness. However, the plot between the two does not show any relationship. As plotted earlier in other samples (as-cast), the activation energy for deformation is plotted as a function of room temperature hardness of the different deformation conditions, irrespective of the alloy composition, Figure 4.58(c). A linear curve fitting was applied to make uniformity with the previous results, Figure 4.40(d). A linear relationship is followed by the fitted data of type with a good level of certainty.

$$HV_d = a_{FS}(Q_d) + b_{FS}, \tag{4.22}$$

where a_{FS} and b_{FS} are the magnitude of the slope and intercept for the linear fit. The magnitude of a_{FS} varies in the range of 0.9 - 6.3, and b_{FS} varies from 29.7 to 44.9.



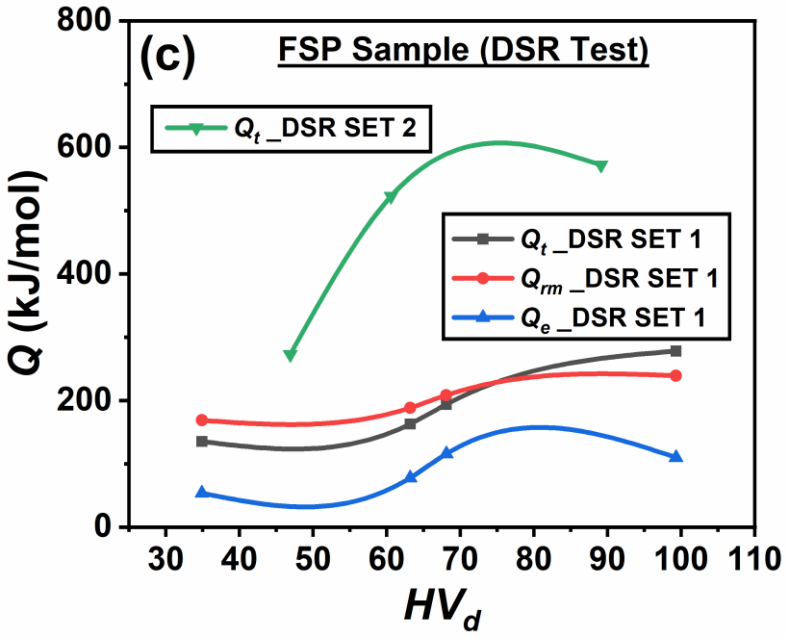


Figure 4.58 : Microhardness of the deformed and undeformed sample as a function of Si content of (a) gage section, (b) shoulder section, and (c) a plot of *Q* for deformation and the post-deformation room temperature hardness (HV_d) for the given composition and test conditions for FSPed Al-Si alloys

Microstructure Evolution During High-Temperature Deformation

Microstructures after deformation were examined for the samples that underwent (i) CSR tests and (ii) differential strain rate-differential temperature tests coupled with CSR tests at the final stage of deformation.

Case (i): Presented in Fig. 4.59(a-l) are the micrographs and size distribution curves after failure at CSR. There appears to be cavitation, shown at lower magnification, from the fracture tips to ~5mm along the gage length. Examination of cavities in the samples of different compositions reveals that maximum cavitation occurs in the hypereutectic Al-30Si alloy, and the cavities of different sizes are spherical in nature. Al-8Si alloy is found to exhibit the smallest size cavities with minimum volume fractions. Al-12Si eutectic shows large-size interconnected (coalesced) cavities elongated in the direction of loading. There appear to be small sizes but interlinked cavities in the loading direction in the Al-20Si alloy. The occurrence of grain growth and coarsening of Si particles, as illustrated at higher magnification in the vicinity of fracture tips, are also shown. The growth in d_α is noted to be ~290-440% and it was obtained to ~105-274% for Si particle size. The distribution curves for d_α and d_p are included in Figure 4.59(i-l). It is noted that the d_α is greater than the d_p in all the alloys, but the size difference between the two phases becomes less with increasing Si content in the alloy.

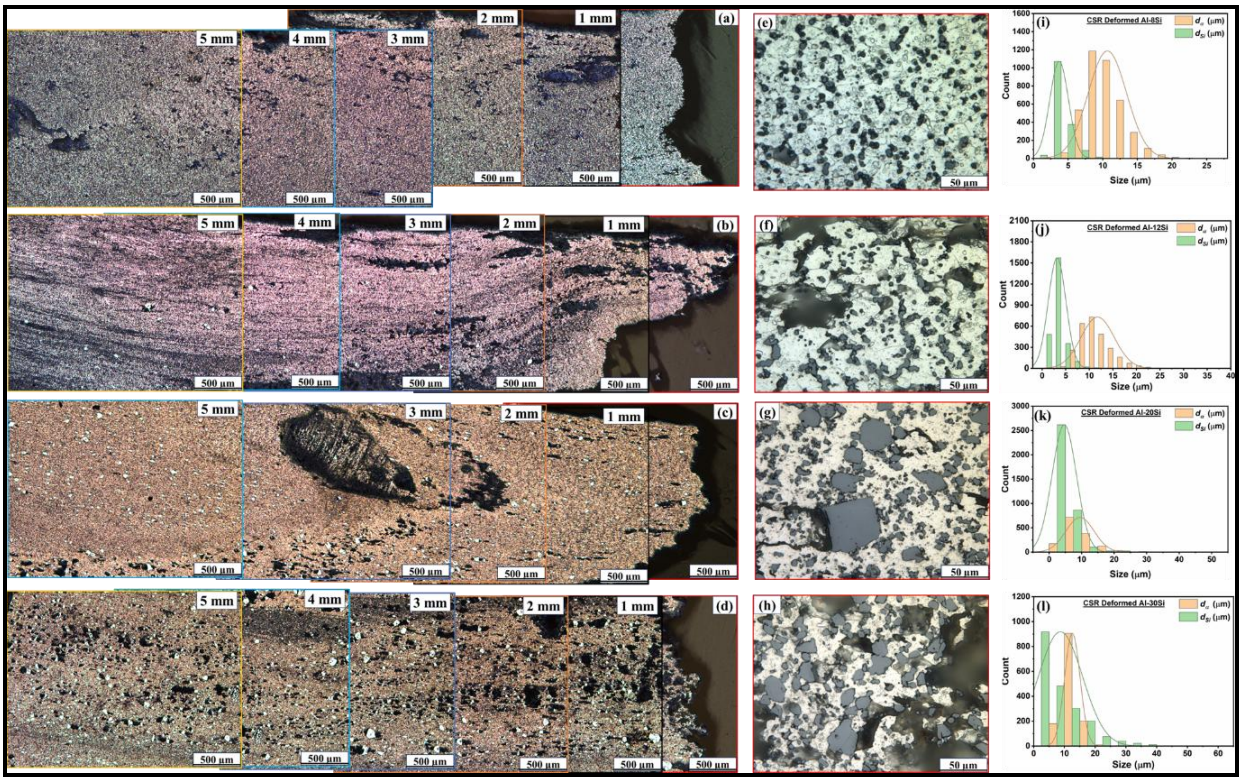


Figure 4.59 : Low magnification micrographs of deformed samples of CSR tests (a-d), (e-h) corresponding higher magnification micrographs of the tips, and (i-l) grain (d_α) and particle size (d_p) distribution of the deformed samples at CSR tests of Al-8Si, Al-12Si, Al-20Si, and Al-30Si alloys

Case (ii): The samples subjected to DSR-differential temperature tests over the temperature range of 800-530K were examined to characterize the evolved microstructures upon failure. Figure 4.60(a-l) represents the microstructures and distributions of d_α and d_p. While the cavities are seen clearly in the hypoeutectic (Al-8Si) and eutectic (Al-12Si) alloys, there appear to be a few cavities in the hypereutectic (Al-20Si) or almost no cavities in the Al-30Si hypereutectic alloys. The cavity formation is seen to be the maximum in the Al-8Si alloy, and mostly, they are in spherical shape, with the large cavities being interconnected in the transverse direction, perpendicular to the loading direction. The mean grain sizes (d_α) upon failure are found to be 13.7, 4.7, 3.4, and 1.6µm in Al-8Si, Al-12Si, Al-20Si, and Al-30Si, respectively. Similarly, the mean particle sizes (d_p) in these alloys were found to be 3.5, 2, 4.95, and 3.5µm, respectively. The d_α and d_p distribution curves exhibit the d_α to be larger than the d_p in the hypoeutectic Al-8Si and eutectic Al-12Si alloys, whereas d_α and d_p both tend to be comparable in the Al-30Si hypereutectic alloy. The growth in d_α is noted to be ~50-407%, and it was obtained to ~40-140% for Si particle size.

Figure 4.61(a-l) shows the micrographs, grain, and particle size distributions upon deformation to failure by coupled DSR-differential temperature tests (840-800K) followed by the CSR deformation test. Here, maximum cavities are present in the samples of Al-12Si alloys, followed by Al-20Si and Al-30Si, with the minimum in the Al-8Si alloy. While the cavities in the Al-12Si are elongated and interlinked to several mm along the gage length, the cavities in the Al-20Si alloy are large, but they are interlinked in the transverse (normal) to the loading direction. The particle size d_p and matrix grain size d_α distributions are presented for all the alloy compositions in Figure 4.61(i-l). The variation in d_α is noted to be 12-17µm, whereas d_p varies in the range of 4-8µm. The growth of α-Al matrix (d_α) and Si particle (d_p) sizes was determined to be 430-530% and 160-280%, respectively.

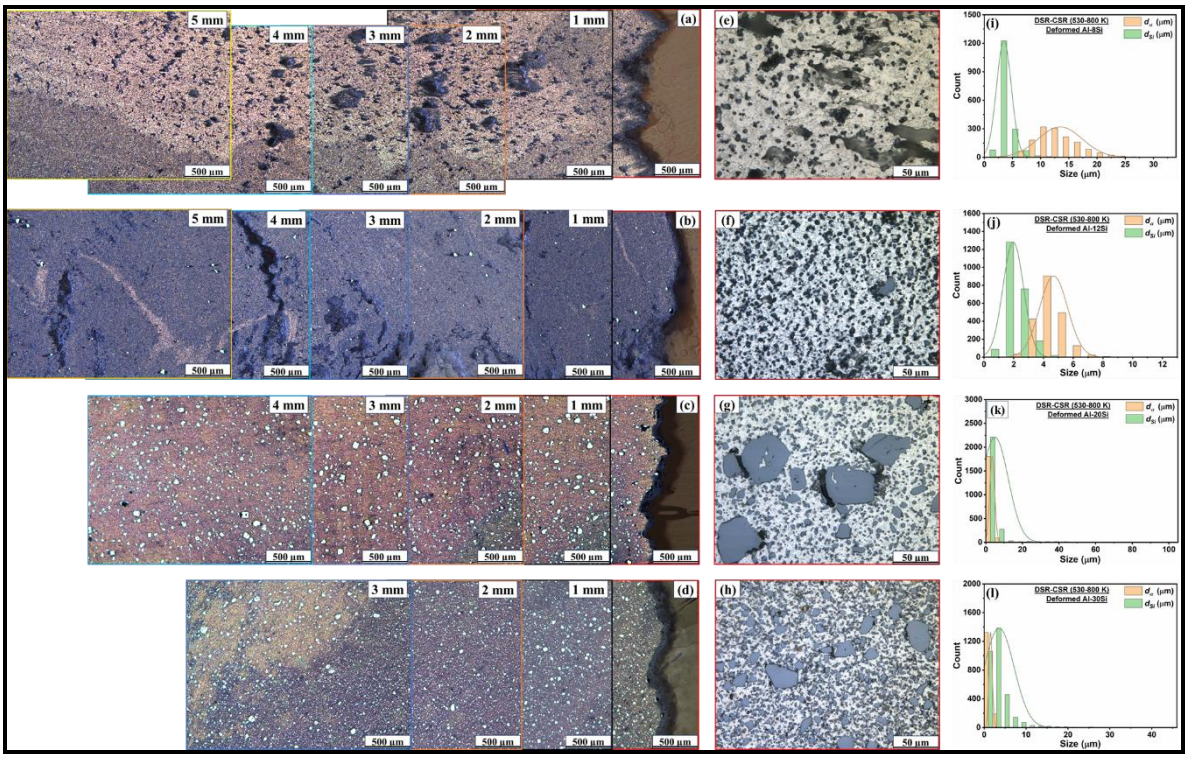


Figure 4.60 : Low magnification micrographs of deformed samples of DSR tests over the temperature range of 800-530K (a-d), (e-h) corresponding higher magnification micrographs of the tips, and (i-l) grain (d_α) and particle size (d_p) distribution of the deformed samples at DSR tests of Al-8Si, Al-12Si, Al-20Si, and Al-30Si alloys

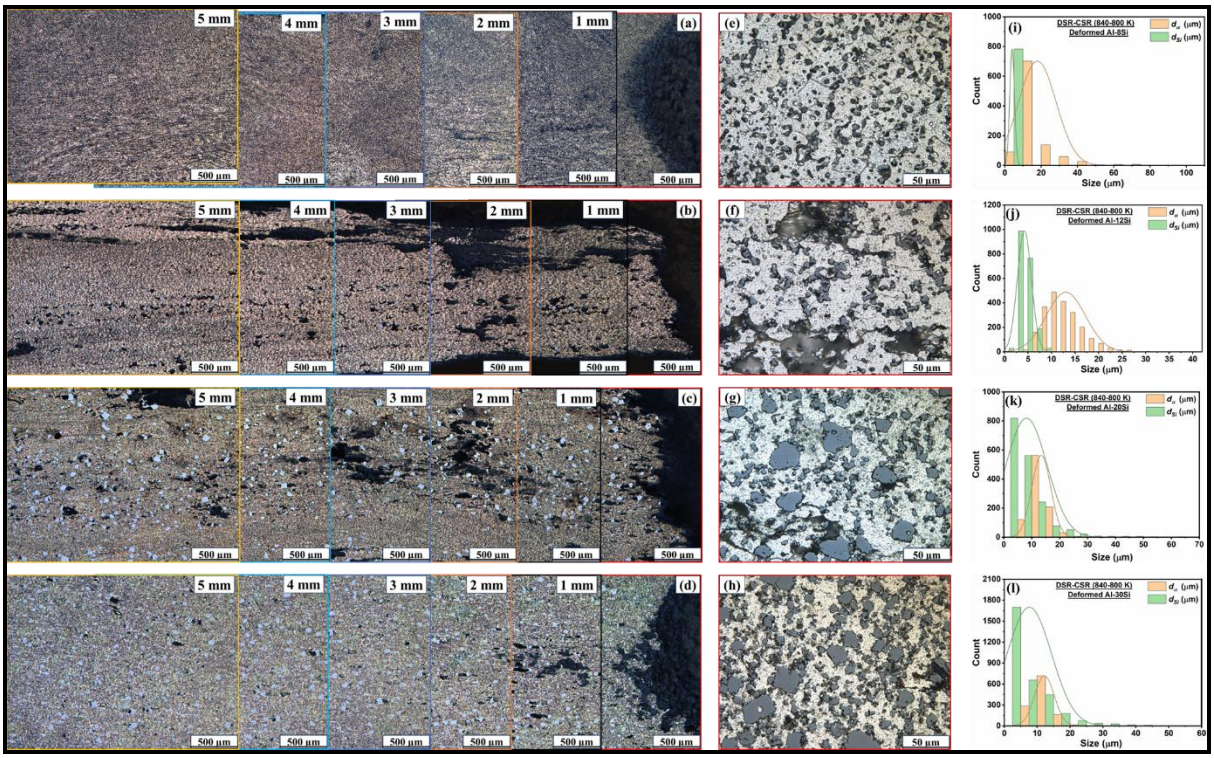


Figure 4.61 : Low magnification micrographs of deformed samples of DSR tests over the temperature range of 840-800K (a-d), (e-h) corresponding higher magnification micrographs of the tips, and (i-l) grain (d_α) and particle size (d_p) distribution of the deformed samples at DSR tests of Al-8Si, Al-12Si, Al-20Si, and Al-30Si alloys

Presented in Figure 4.62(a,b) is the ratio d_α/d_p plotted as a function of volume fraction of Si particles, f_p for initial FSPed samples, Figure 4.62(a) and upon deformation at CSR, as well as after DSR-differential temperature test coupled with the CSR tests, case (i), and case (ii), Figure

4.62(b). Interestingly, in most of the cases, the microstructural changes of the two phases appear to be interdependent, and the ratio of matrix and particle sizes (d_α/d_p) decreases with increasing volume fraction of second-phase silicon particles, f_p, according to the following relationship.

$$\frac{d_\alpha}{d_p} = m_{FS}(f_p) + C_{FS}, \tag{4.23}$$

m_{FS} is the slope, and C_{FS} is the intercept, the values of which are listed in the table for different conditions.

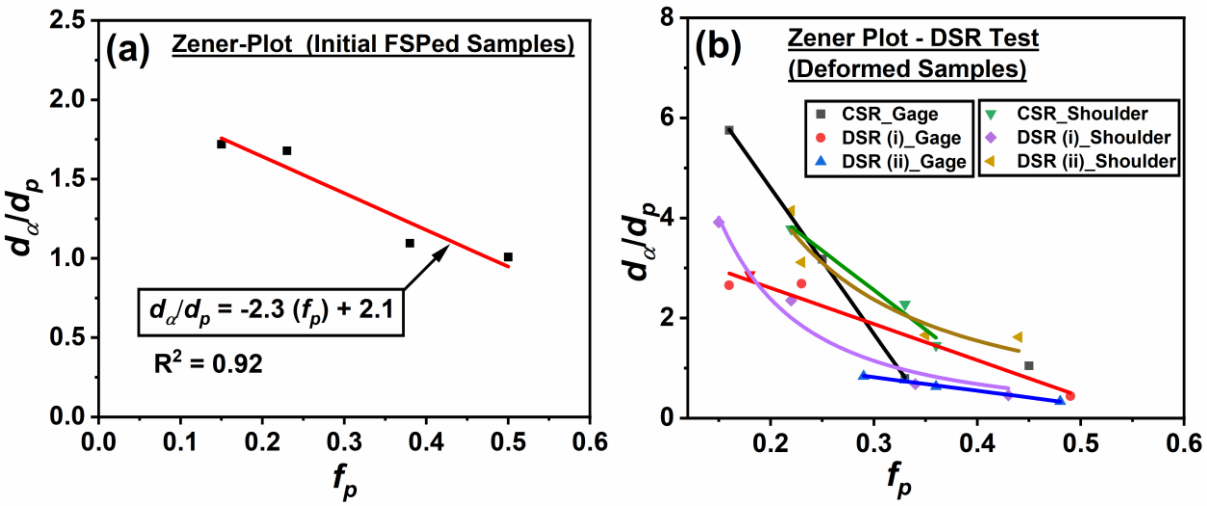


Figure 4.62 : Ratio d_α/d_p plotted as a function of volume fraction of Si particles, f_p for initial FSPed samples (a), and upon deformation at CSR as well as after DSR-differential temperature test coupled with the CSR tests of all the Al-Si alloys (b)

Table 4.8 : m_{FS} and C_{FS} values for the different test conditions and alloy compositions

Parameter	*Undeformed Sample*	*Deformed Sample*					
		Gage			*Shoulder*		
		CSR	*DSR(i)*	*DSR(ii)*	*CSR*	*DSR(i)*	*DSR(ii)*
m_{FS}	-2.3	-15.8	-12.4	-10.5	-16.6	-7.2	-2.7
C_{FS}	2.1	7.3	5.4	5.9	7.6	4	1.6

…